

THESIS FOR THE DEGREE OF DOCTOR OF PHILOSOPHY

Growth of ZnO/GaN distributed Bragg
reflectors by plasma-assisted molecular beam
epitaxy

David Adolph



Photonics Laboratory
Department of Microtechnology and Nanoscience (MC2)
CHALMERS UNIVERSITY OF TECHNOLOGY
Göteborg, Sweden, 2016

Growth of ZnO/GaN distributed Bragg reflectors by plasma-assisted molecular beam epitaxy

David Adolph

Göteborg, May 2016

©David Adolph, 2016

ISBN 978-91-7597-393-7

Doktorsavhandling vid Chalmers Tekniska Högskola

Ny serie 4074

ISSN 0346-718X

Technical Report MC2-336

ISSN 1652-0769

Photonics Laboratory

Department of Microtechnology and Nanoscience (MC2)

Chalmers University of Technology, SE-412 96 Göteborg, Sweden

Phone: +46 (0) 31 772 1000

Front cover illustration: A crackfree uniform 20-period ZnO/GaN distributed Bragg reflector. Left: A naked eye view of the cleaved reflector. Center: Cross-sectional high angle annular dark-field scanning transmission electron microscope micrograph across the cleaved edge of the reflector. Right: Schematic wurtzite unit cell for ZnO and GaN.

Printed by Chalmers reproservice, Chalmers University of Technology
Göteborg, Sweden, May, 2016

Growth of ZnO/GaN distributed Bragg reflectors by plasma-assisted molecular beam epitaxy

David Adolph

Photonics Laboratory

Department of Microtechnology and Nanoscience (MC2)

Chalmers University of Technology, SE-412 96 Göteborg, Sweden

Abstract

This thesis describes epitaxial growth of ZnO/GaN distributed Bragg reflectors by hybrid plasma-assisted molecular beam epitaxy on GaN(0001). The unique hybrid approach employed the same growth chamber for continuous growth of both ZnO and GaN without exposing the layers to the ambient conditions. The Bragg reflectors consisted up to 20 periods as verified with cross-sectional transmission electron microscopy. The maximum achieved reflectance was 77% with a 32 nm wide stopband centered at 500 nm. A profound study of the ZnO and the ZnO/GaN growth processes was carried out including growth along both ZnO(0001) and ZnO(000 $\bar{1}$) directions. The impact of growth temperature, O₂ flow-rate and the Zn-flux on the ZnO growth rate, structural quality and surface and interface morphology, was investigated in detail. The layers were studied with a wide range of materials characterization techniques such as x-ray diffraction, scanning electron microscopy, atomic force microscopy, secondary-ion mass spectroscopy and transmission electron microscopy. Low-temperature growth as well as two-step low/high-temperature deposition was carried out where the latter method improved the Bragg mirror reflectance. Samples grown along the ZnO(0001) direction yielded a better surface morphology as revealed by scanning electron microscopy and atomic force microscopy. It was observed that the growth rate of ZnO decreased when the O₂ flow rate was increased. This is unexpected with respect to the common knowledge in the molecular beam epitaxy research community. A detailed study of this effect involving optical emission spectroscopy of the O-plasma, revealed that the cause was an overall decrease of the amount of the active O provided by the plasma source. Reciprocal space maps showed that ZnO(000 $\bar{1}$)/GaN reflectors are relaxed whereas the ZnO(0001)/GaN DBRs are strained. The ability to n-type dope ZnO and GaN makes the ZnO(0001)/GaN DBRs interesting for various optoelectronic cavity structures such as blue vertical surface emitting lasers and novel cavity-polariton devices. This is the first time ZnO/GaN DBRs have been demonstrated.

Keywords: ZnO, GaN, Oxides, Nitrides, distributed Bragg reflector (DBR), molecular beam epitaxy (MBE)

List of Papers

This thesis is based on the following appended papers:

- [I] **David Adolph** and Tommy Ive, "Nucleation and epitaxial growth of ZnO on GaN(0001)," *Appl. Surf. Sci.*, **307** (2014) 438–443
- [II] **David Adolph**, Tobias Tingberg, Thorvald Andersson and Tommy Ive, "Plasma-assisted molecular beam epitaxy of ZnO on *in-situ* grown GaN/4H-SiC buffer layers," *Front. Mater. Sci.* 2015, **9**(2): 185–191
- [III] **David Adolph**, Tobias Tingberg and Tommy Ive, "Growth of ZnO(0001) on GaN(0001)/4H-SiC buffer layers by plasma-assisted hybrid molecular beam epitaxy," *J. Cryst. Growth*, **426** (2015) 129–134
- [IV] **David Adolph** and Tommy Ive, "Impact of O₂ flow rate on the growth rate of ZnO(0001) and ZnO(000 $\bar{1}$) on GaN by plasma-assisted molecular beam epitaxy," *Phys. Stat. Solidi B*, Online 16 March 2016, DOI: 10.1002/pssb.201552764. Issue and page number not assigned yet.
- [V] **David Adolph**, Reza R. Zamani, Kimberly A. Dick and Tommy Ive, "Hybrid ZnO/GaN distributed Bragg reflectors grown by plasma-assisted molecular beam epitaxy," Submitted to *Appl. Phys. Lett. Mater.*, 15 April 2016

Acknowledgement

I am grateful to my supervisor Associate Professor Tommy Ive for your endless support. I appreciate our team-work and your commitment during the entire project. I value our discussions and the problems we have been able to solve along the way. I wish you all the best in your future career. I thank my examiner Professor Anders Larsson for your support and confidence related to this research project. Without the world-wide-famous pioneer within the field of Molecular Beam Epitaxy, Professor Thorvald Andersson, there would be no MBE-360 at Chalmers. I am grateful for our fruitful discussions and your encouragement.

I thank Jeanette Träff and Helena Russberg for administrative support and Kaija Matikainen for assistance with the lab supplies. Carl-Magnus Kihlman, you deserve special acknowledgement for the occasion when you went to Chalmers and helped me on a technical matter despite the fact that you are retired. Thank you to Fredrik Johansson and Carl-Magnus who designed and constructed the supports to the cryo-pump and to the O- and N-plasma sources. I thank Jan-Åke Wiman for showing me how to spot-weld. With this skill I could repair our substrate heater. I thank Mats Myremark for the drawings and the construction of spare Ta-coils to our substrate heater.

I appreciate the technical support during the first year refurbishment of the MBE-360. This includes specially the MC2-staff Henrik Frederiksen, Lars-Åke Sidenberg, Christer Andersson and Johan Persson. Kjell Blank at Löwener Vacuumservice AB is also acknowledged. I thank Jörgen Schaeffer at Eurovac Sweden for repairing our RHEED-equipment, John Lockley (Veeco) for support related to the plasma sources and Kristian Flodström (Rowaco AB) for the help to find suitable MFCs with controller. I thank the tool-responsible who maintain the characterization equipment I have used, Anders Kvist (SEM Ultra-55), Alexey Kalaboukhov (XRD) and Piotr Jedrasik (AFM).

I thank Göran Alestig who helped me to improve my ellipsometric measurements. Dr. Per Malmberg is acknowledged for TOF-SIMS on our initial samples. I thank Tobias Tingberg who performed room-temperature Hall measurements and Reza Baghdadi

who carried out low-temperature IV-measurements. I thank Professor Kimberly Dick Thelander and Dr. Reza R. Zamani for taking the decision to collaborate with us and perform TEM-measurements on the DBRs. Your TEM cross-sections show the results in a manner everyone can understand. This is an important contribution. I thank Professor Åsa Haglund for your support and wish you and Ehsan Hashemi good luck with the transmission line measurements on the DBRs.

I thank my fellow PhD-students and colleagues at the Photonics lab and MC2 for creating a focused and friendly work environment. It has been a great time and I wish you all good luck.

I am indebted to my family for a praiseworthy upbringing and I thank you all for this. I am also grateful for the support and feedback from my friends, you know who you are.

I highly value my former teachers in Strömsnäsbruk, Ljungby, Halmstad and Lund. Your patience, high demands and inspiring attitude affect the outcome for research projects years later after your efforts.

Finally, and with most importance I want to thank my beloved wife Eleonor who has let me spend a considerable amount of time on ZnO, GaN and MBE during 5 years. You have allowed me to fulfil dreams. I thank you so much for your love, work and support. I am a really lucky man to have met such a good wife as you! Samuel, Elin and John - I encourage each one of you to find your own way through life, never give up and work persistent to fulfil your inner dreams. There is much interesting to investigate. Also concentrate on your own efforts and be glad when your brother, sister and friend succeed. When they stumble and fall, then it is also the appropriate time to be a good sister, brother and friend. In other words, grow on your own and let other people grow as well. Why not then grow semiconductor widebandgap wurzite or cubic crystals? The p-doping for ZnO is still an issue to be solved.

This work was supported by the Swedish Research Council (Grant DNR 2009-4903). It was also partly supported by a grant from the Department of Microtechnology and Nanoscience (MC2) at Chalmers University of Technology.

David Adolph

*Göteborg
May 2016*

List of Acronyms

- AFM** atomic force microscopy [20, 31, 33, 37, 47, 48, 50, 51]
BEP beam equivalent pressure [18, 69]
CAR continuous azimuthal rotation [16, 18]
CG-mode Columnar growth mode [13]
DBR distributed Bragg reflector [i, 1, 2, 4, 5, 7, 9, 12, 25, 53]
FM-mode Frank-van der Merwe growth mode [13, 15]
FWHM full width at half maximum [36, 37]
HAADF-STEM high-angle annular dark-field scanning transmission electron microscope [63]
LD laser diode [1]
LED light emitting diode [1]
MBE molecular beam epitaxy [i, 1, 2, 11, 13, 20, 37, 49]
MOCVD metal-organic chemical vapor deposition [2, 8, 42]
PBN pyrolytic boron nitride [16]
PLD pulsed laser deposition [2]
PV peak to valley [48, 49, 51]
RHEED reflection high energy electron diffraction [11, 18, 33, 34, 42]
RMS root mean square [37, 48, 49, 51]
SEM scanning electron microscopy [12, 14, 19–21, 25, 36]
SF-mode Step-flow growth mode [13, 15]
SK-mode Stranski-Krastanov growth mode [13]
SPM scanning probe microscopy [10]
SThM scanning thermal measurement [10]
TEM transmission electron microscopy [25]

TOF-SIMS time of flight secondary ion mass spectroscopy [25, 38]
TSK terrace step kink model [13, 37]
UHV ultra high vacuum [19]
VCSEL vertical cavity surface emitting laser [2, 3, 69]
VW-mode Volmer-Weber growth mode [13]
XRD X-ray diffraction [10]

Table of Contents

Abstract	i
List of Papers	iii
Acknowledgement	v
List of Acronyms	vii
1 Introduction	1
1.1 Motivation - ZnO/GaN	1
1.1.1 ZnO/GaN DBRs	2
1.2 Organization of thesis	3
2 Physical properties of GaN and ZnO	5
2.1 Crystal structure	5
2.2 Optical properties	7
2.2.1 ZnO/GaN - DBR principle	9
2.2.2 DBR - design strategy	9
2.3 Thermal properties	10
3 Epitaxy	11
3.1 Introduction	11
3.1.1 Heteroepitaxy	12
3.1.2 Growth modes	12
3.1.3 Epitaxy - atomistic description	13
3.2 MBE technology - Nitrides and Oxides	16
3.2.1 Ultra high vacuum	16
3.2.2 Substrate heater, sample mounting and transfer	16
3.2.3 Solid effusion cells	16

3.2.4	Nitrogen and Oxygen plasma sources	17
3.2.5	Reflection High Energy Electron Diffraction	18
3.2.6	The BEP-gauge	18
4	Characterization Techniques	19
4.1	Scanning electron microscopy	19
4.2	Atomic force microscopy	20
4.3	X-ray diffraction	21
4.4	Time of flight secondary ion mass spectroscopy	25
4.5	Transmission Electron Microscopy	25
4.6	Spectral Reflectance Measurements	26
4.7	Electrical characterization	27
4.8	Optical emission spectroscopy	28
5	Growth of ZnO and GaN	31
5.1	Substrates	31
5.1.1	Substrate preparation	32
5.1.2	RHEED - ZnO on GaN	33
5.2	GaN on 4H-SiC(0001)	33
5.3	ZnO-nucleation and initial growth	36
5.3.1	ZnO nucleation on 4H-SiC(0001)	37
5.3.2	ZnO nucleation on GaN/Al ₂ O ₃ -templates	38
5.3.3	ZnO nucleation on GaN/4H-SiC	40
5.3.4	Zn(0001) and ZnO(0001) growth	41
5.4	Growth of smooth ZnO layers on GaN(0001)/4H-SiC	41
5.4.1	ZnO - growth temperature dependence	42
5.4.2	ZnO - Zn source temperature dependence	43
5.4.3	ZnO - O ₂ flow-rate dependence	44
5.4.4	ZnO - smooth layers	47
6	ZnO/GaN distributed Bragg reflectors	53
6.1	Growth procedure - ZnO/GaN DBRs	53
6.2	List of selected sample properties - ZnO/GaN DBRs	55
6.3	Properties of ZnO/GaN DBRs - Color	56
6.4	ZnO/GaN DBR surface morphology	59
6.5	ZnO/GaN DBR Reflectance	61
6.6	Microanalysis of ZnO/GaN DBRs	63
6.7	Structural analysis of ZnO/GaN DBRs	64
7	Summary and Outlook	69
7.1	Summary and discussion	69
7.2	Outlook	71

8 Summary of Papers	73
References	77
Papers I–V	89

Chapter 1

Introduction

This chapter gives an introduction to ZnO and GaN and the benefits of combining them to a into a hybrid ZnO/GaN DBR grown by a hybrid nitride/oxide MBE system. A description of the organization of this thesis is given at the end of this chapter.

1.1 Motivation - ZnO/GaN

Semiconductors with a bandgap above 3 eV such as ZnO and GaN, are generally referred to as wide bandgap materials. The group-III materials B, Al, Ga and In alloyed with the group-V element N, are referred to as III-nitrides. The direct bandgap of GaN is 3.39 eV at 300 K [1]. The growth of GaN is today well-established [2]. Nitride-based white-light-emitting light emitting diode (LED)s are very energy-efficient light emitters that are replacing incandescent light bulbs thus reducing the energy consumption needed for lightning. White LEDs have also been combined with solar cells and rechargeable batteries into compact, reusable and portable systems that are now introduced in third world countries which lack a developed power grid. Lamps based on burning fossil-fuels such as oil and kerosene are widely used in these countries. These fossil-fueled lamps emit toxic fumes and are energy inefficient. The introduction of clean and reusable white LED systems therefore offer significant improvement of the quality of life in third world locations where the power grid is inaccessible. Nitride-based edge-emitting laser diode (LD)s operating at a wavelength of 405 nm (blue-violet light) are used in Blu-ray DVD players [3]. ZnO is formed by Zn from group II and O from group VI. The direct bandgap of ZnO is 3.37 eV at 300 K [4] which is close to the GaN bandgap. All efforts to obtain reliable p-doping in ZnO

have so far been unsuccessful [5]. ZnO and GaN exhibit a wurtzite structure with similar in- and out-of-plane lattice constants a and c . For bulk ZnO, $a_{\text{ZnO}} = 0.325$ and $c_{\text{ZnO}} = 0.521$ nm, respectively compared to $a_{\text{GaN}} = 0.319$ and $c_{\text{GaN}} = 0.518$ nm for GaN. The ZnO/GaN lattice mismatch $(a_{\text{ZnO}} - a_{\text{GaN}})/a_{\text{GaN}}$ is 1.9% which is a comparably small value and therefore reduces the risk of forming cracks.

MBE can be used to fabricate wide-bandgap heterostructures with interfaces that are abrupt on the atomic scale [6, 7]. This is achieved by controlling the supply of ultra-pure source material with mechanical shutters.

Both ZnO and GaN can be fabricated with other techniques such as pulsed laser deposition (PLD) [8] and metal-organic chemical vapor deposition (MOCVD) [9]. Hybrid ZnO/GaN LED structures [10–13] and ZnO transparent contacts [14] have been demonstrated. These hybrid structures were always grown using two different deposition systems. The InGaN/GaN layers were first grown in an epitaxy system dedicated for nitrides. Hereafter, the sample was removed and re-mounted in another system for the overgrowth of ZnO. This procedure was also used recently for the ZnO(0001) overgrowth on GaN(000 $\bar{1}$) nanowires [15]. Often, MOCVD was used for the growth of InGaN/GaN QWs while a range of techniques such MOCVD, PLD and MBE as were used for the deposition of ZnO. This procedure introduced Ga_xO_y sub-oxides uncontrollably on the nitride surface. These sub-oxides affect both the structural quality of the overgrown ZnO layer and also the homogeneity of the ZnO/GaN interface [16–21]. Non-radiative recombination centers can also be introduced into the structure by these suboxides [11]. The formation and thus the adverse effects of the sub-oxides can be avoided or minimized if the InGaN or GaN is not exposed to air before the ZnO growth. This can be achieved with a hybrid nitride/oxide MBE-system where the same MBE growth chamber is used for both ZnO and GaN growth.

In this work the epitaxial growth of GaN and ZnO was done using the same growth chamber which is a unique approach that to our knowledge, has only been reported once before in Ref. [22]. The system design and assembly was part of this project. The hybrid configuration facilitates immediate and subsequent growth of the two materials without the exposing any of them to the air ambient. Thus, the formation of sub-oxides that are detrimental for subsequent epitaxial growth of ZnO, can be avoided. This hybrid system was used to grow ZnO/GaN DBR:s for the first time.

1.1.1 ZnO/GaN DBRs

GaN-based blue-emitting vertical cavity surface emitting laser (VCSEL)s have been reported by several research groups [23–28]. Both nitride based epitaxial and dielectric DBRs have been used for the formation of the VCSEL optical cavity. However, no commercial blue-emitting VCSEL exist yet.

The first approach using nitride DBRs utilizes a relatively small difference between the refractive index of $\text{Al}_x\text{Ga}_{1-x}\text{N}$ or AlInN and GaN which means that a larger number of periods N is needed to achieve a high reflectance DBR [24, 25, 29–31]. For

instance, $N > 20$ for AlN/GaN DBRs and $N > 40$ for AlInN/GaN Bragg mirrors. The cavity with the active region is grown on top of the bottom DBR. The top DBR consisting of dielectric materials, is then bonded onto the cavity. Strain-engineering is needed for the $\text{Al}_x\text{Ga}_{1-x}\text{N}/\text{GaN}$ DBRs to avoid crack-formation caused by the large lattice mismatch between high-Al containing $\text{Al}_x\text{Ga}_{1-x}\text{N}$ and GaN. The largest refractive index contrast for nitride-based DBRs is achieved for the AlN/GaN combination but these DBRs also exhibit the largest challenges with crack formation.

The second approach use dielectric DBRs for both the bottom and the top DBRs. The advantage is that only a few periods are needed to obtain a high reflectance [23, 26–28, 32–35]. The drawback with this approach is the high precision processing steps needed to make a cavity with a well defined-thickness.

None of the described DBR approaches yield electrically conducting structures which therefore require additional processing steps to enable electrical injection.

In this thesis a third approach using hybrid ZnO/GaN DBRs is described. This method allows epitaxially growing a complete VCSEL structure in-situ which significantly reduces the number of costly processing steps required to fabricate the discrete VCSEL device. The lattice-mismatch between ZnO and GaN is 1.9% which is comparatively small and therefore minimizes the risk of forming cracks. The refractive index difference between ZnO and GaN is ≈ 0.4 at a wavelength λ of 450 nm. This difference is relatively large and therefore a smaller number of periods ($N < 20$) are needed to achieve a high-reflectance DBR. Finally, n-doping of both ZnO [36] and GaN is straightforward meaning that an electrically conducting ZnO/GaN DBR can be achieved.

A hybrid ZnO/GaN DBR could thus enable the fabrication a blue-emitting VCSEL that employs current injection through the DBR similar to GaAs-based VCSELs.

One of the general advantages of VCSELs as compared to edge-emitting laser diodes is that they can be fabricated on the wafer-scale and also tested directly on the wafer without having to dice the wafer. This lowers the fabrication costs of VCSELs compared to edge-emitting laser diodes that first must be processed into discrete devices before they can be tested.

1.2 Organization of thesis

The next chapter 2 introduces a selection of materials properties for ZnO and GaN. Hereafter, chapter 3 gives a short introduction to epitaxy. The concepts of different growth modes and the atomistic picture of epitaxy are presented. A technical section showing the configuration of the hybride nitride and oxide MBE growth chamber is also included. The following chapter 4 shows the characterization techniques used to investigate the grown structures. A description of the optical emission spectroscopy setup used to assess the efficiency of the O-plasma source is also given. In chapter 5 the growth methods and results of ZnO and GaN on 4H-SiC(0001) and GaN/Al₂O₃(0001)

templates are described. The effect of substrate pre-treatment, nucleation and subsequent growth is presented. A description on how to grow smooth ZnO layers of both ZnO(0001) and ZnO(000 $\bar{1}$) on GaN(0001) is given. This chapter present a new found ZnO growth rate dependence on the O₂ flow rate and how this is related to the emission spectra from the O-plasma source. The following chapter 6 describes the growth results of ZnO/GaN DBRs fabricated along the ZnO(000 $\bar{1}$) and ZnO(0001) directions. Hereafter, chapter 7 provides a summary and discussion with an outlook for ZnO/GaN DBRs. The last chapter 8 presents a summary of the appended papers.

Chapter 2

Physical properties of GaN and ZnO

This chapter provides a brief summary of selected physical properties of the wide-bandgap semiconductors GaN and ZnO and how these can be utilized in a DBR.

2.1 Crystal structure

A crystal consists of periodically arranged atoms. The arrangement can be described mathematically by a lattice with an attached basis that is associated with each lattice point. Crystals exhibit long-range order compared with amorphous materials which exhibit no order of atoms. The structure of a crystal influence its electrical, optical and thermal properties. Table 2.1 summarizes a selection of properties of ZnO and GaN.

Figure 2.1 shows a schematic of the wurtzite crystal structure which is the thermodynamically stable crystal phase for both GaN and ZnO. Each cation (Ga and N) and anion (Zn and O) atom is indicated in the figure. The primitive cell is a hexagonal structure with four basis atoms [46]. The unit vectors are $\mathbf{a}_1 = (\frac{1}{2}, \frac{\sqrt{3}}{2}, 0)\mathbf{a}$, $\mathbf{a}_2 = (\frac{1}{2}, -\frac{\sqrt{3}}{2}, 0)\mathbf{a}$ and $\mathbf{c} = (0, 0, \frac{c}{a})\mathbf{a}$. The crystallographic $[0001]$ and $[000\bar{1}]$ directions are indicated in Fig. 2.1 and are of special importance for the work presented in this thesis since both ZnO(0001) and ZnO(000 $\bar{1}$) have been grown on GaN(0001) substrates. GaN(0001) have also been fabricated on 4H-SiC(0001)-substrates and also on both ZnO(0001) and ZnO(000 $\bar{1}$) layers. ZnO(0001) and Zn(000 $\bar{1}$) are also referred to as Zn- and O-polar ZnO [47]. The corresponding names for GaN(0001) and GaN(000 $\bar{1}$) are Ga- and N-polar GaN [41].

2. PHYSICAL PROPERTIES OF GAN AND ZNO

Table 2.1: Selected properties for GaN and ZnO

Property	Unit	GaN	ZnO
Lattice constant a (300 K)	Å	3.189 [37]	3.249 [38]
Lattice constant c (300 K)	Å	5.185 [37]	5.205 [38]
Band gap E_g (300 K)	eV	3.39 [1]	3.37 [4]
Ordinary ref. index n_0 (450 nm)	-	2.45 [39]	2.106 [40]
Th. exp. coeff. α^{a_0} (100-600)K	K^{-1}	$1.2\text{-}5 \times 10^{-6}$ [41]	4.75×10^{-6} [5]
Th. exp. coeff. α^{c_0} (100-600)K	K^{-1}	$1.1\text{-}4.4 \times 10^{-6}$ [41]	2.9×10^{-6} [5]
Th. conductivity κ	W/cm-K	1.86-2.05 [42]	1.10-1.16 [43]
Melting point T^M	K	2791 [41]	1703 [5]
Decomposition temperature T_E	$^{\circ}C$	850 [44]	550–600
Spontaneous polarization P_{sp}	C/m ²	-0.034 [37]	0.057 [45]

The positions of the atoms, in units of \mathbf{a}_1 , \mathbf{a}_2 and \mathbf{c} are $(0,0,0)$ and $(\frac{2}{3}, \frac{1}{3}, \frac{1}{2})$ for the positive cation atoms, and $(0,0,u)$ and $(\frac{2}{3}, \frac{1}{3}, u + \frac{1}{2})$ for the negative anion-atoms, where u is the dimensionless internal parameter. For the ideal wurtzite structure $c/a = \sqrt{\frac{8}{3}}$ and $u = \frac{3}{8}$ [48]. Table 2.1 gives the in-plane lattice constants a and out of plane lattice constants c for GaN and ZnO at room temperature.

One way of looking at a crystal structure is by identifying the stacking sequence of atoms and classifying each stacking case as a specific polytype [49]. Let a capital letter (A,B,C) denote a cation-anion pair in the vertical direction (one bilayer) in figure 2.1(a). Different capital letters mean different positions of a bilayer in the horizontal plane. The stacking sequence for wurtzite (GaN and ZnO) is AB repeated in the c -direction.

One substrate used in this work is the 4H-SiC(0001)-substrate where H denotes hexagonal and the number 4 refers to the specific polytype [49]. The stacking sequence for 4H-SiC(0001) is ABCB repeated in the c -direction. The lattice constants for 4H-SiC(0001) are $a=0,3073$ nm, $c=1,0053$ nm [50].

Two known polytypes of III-nitrides and II-oxides are 2H-GaN or ZnO and 3C-GaN or ZnO [51, 52]

Figures 2.2(a)–(f) show various cross-sections of the wurtzite structure. Figure 2.2(a) shows the crystal with c -, a - and m -planes. The c -plane viewed from above with the $[0001]$ c -axis directed out from the image is shown in Fig. 2.2(b) The opposite plane is referred to as $[000\bar{1}]$. Figure 2.2(c) shows the wurtzite crystal with the normal of the a -planes directed to the right and the c -direction directed up. Figure 2.2(d) shows a side view of a ZnO(0001) or Zn-polar crystal and Fig. 2.2(e) shows a ZnO(000 $\bar{1}$) (O polar) crystal. The effect of compression of a crystal is shown in Fig. 2.2(f). Compression occurs when a crystal with a larger in-plane lattice constant is grown onto a crystal with a smaller in-plane lattice constant such as ZnO grown on

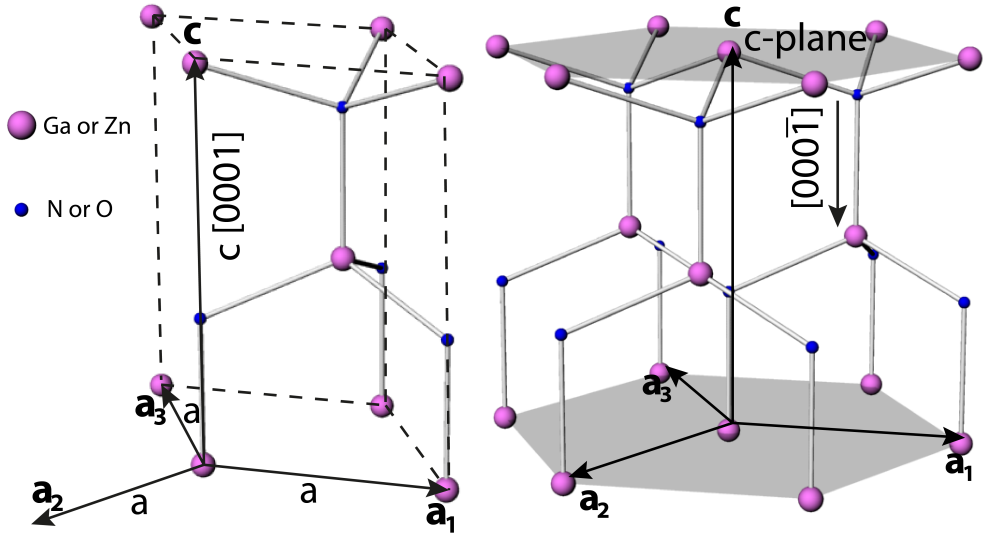


Figure 2.1: Schematic of the wurtzite structure. Hexagonal primitive unit cell with four basis atoms (dashed lines in the left image) [46]. Each atom is bonded to four nearest neighbors. The crystallographic $[0001]$ and $[000\bar{1}]$ directions are indicated. The normal of the c -plane is directed from the cation (Ga or Zn) to the anion (N or O). The in plane lattice constant is denoted as a and the out of plane lattice constant is denoted as c .

GaN. Compressive strain will decrease the in-plane lattice constant a and increase the lattice constant c . The opposite occurs when a material is grown on a substrate with a larger in-plane lattice constant, for instance GaN on ZnO. Strain-free layers are said to be relaxed.

2.2 Optical properties

The refractive indices are of utmost importance for the design of a DBR since they ultimately determine the number of DBR periods needed. The refractive indices can be determined with ellipsometry or the prism-coupling method. A consequence of the anisotropic wurtzite crystal is that it has two refractive indices, the n_o -ordinary (for polarization parallel to the c -axis) and the n_e -extraordinary refractive indices (for polarization perpendicular to the c -axis). Table 2.1 lists the values for the ordinary refractive indices, given for GaN and ZnO at 450 nm. The refractive index for ZnO can

2. PHYSICAL PROPERTIES OF GAN AND ZNO

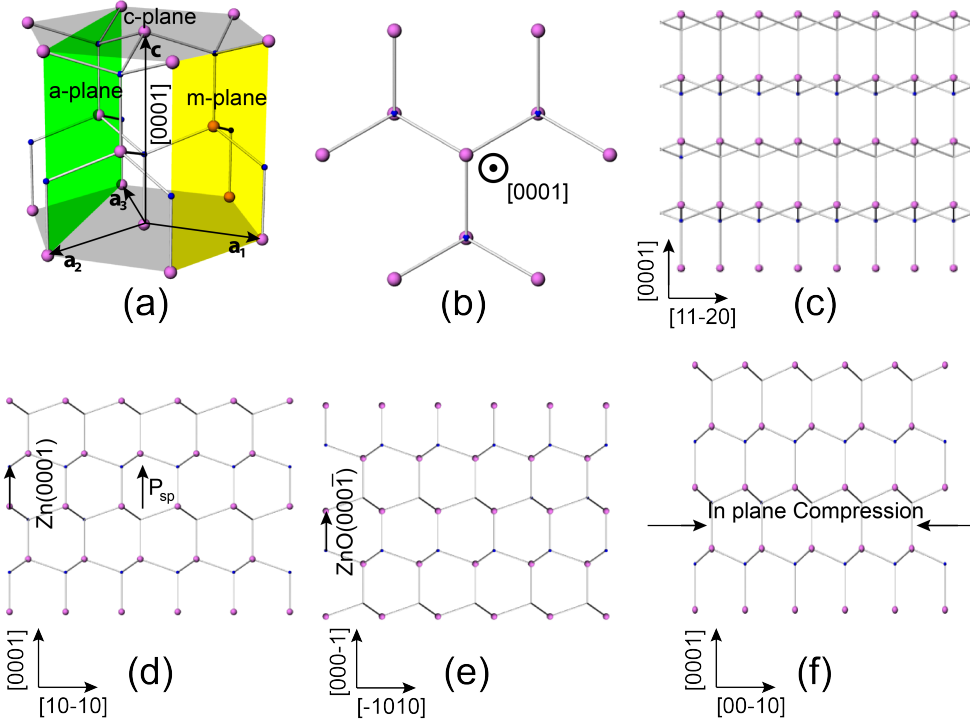


Figure 2.2: Schematic for the wurtzite crystal. Hexagonal unit cell with a, m and c-planes (a). Top view of c-plane surface (b). Side-view of crystal (c). Side view of Zn(0001) (d). Side view of ZnO(0001) (e). In-plane compressive strain decrease the in-plane lattice constant a and increase the out-of-plane c -lattice constant (e).

be modeled below the fundamental absorption edge by using the first order Sellmeier equation:

$$n(\lambda) = \sqrt{A + \frac{B\lambda^2}{\lambda^2 - C^2}} \quad (2.1)$$

where A , B and C are fitting parameters and λ is the wavelength. Fits against experimental data are $A=2.84$ (2.85), $B=0.84$ (0.87) and $C=0.319$ (0.310) μm for $\vec{E} \perp \vec{c}$ and $(\vec{E} \parallel \vec{c})$ [53]. The corresponding first order fitting parameters for GaN are $A=3.60$, $B=1.75$ and $C=0.256$ μm for $(\vec{E} \parallel \vec{c})$ [54]. The refractive index of a material is also affected by the temperature as shown for GaN [39]. Refractive indices determined with the prism-coupling method for MOCVD grown GaN between 442–1064 nm are given

in [55]. The refractive indices for ZnO can be found in refs. [53, 56–58]. Refractive indices at $T=4.2$ K near the absorption edge are found in ref.[58].

2.2.1 ZnO/GaN - DBR principle

Figure 2.3(a) shows a schematic of a GaN/ZnO/substrate quarter-wave $\lambda/4$ reflector structure. If the thickness d of each layer fulfills $d = \lambda/(4n)$ where n is the refractive index of the layer material, the reflected light will add up in phase which will result in the light being reflected efficiently. The reflectivity is enhanced when more $\lambda/4$ pairs are stacked on top of each other. The large refractive index difference between ZnO and GaN (≈ 0.4) is advantageous since it means that only a small number of pairs is needed to reach a high reflectivity [Fig. 2.3(b)].

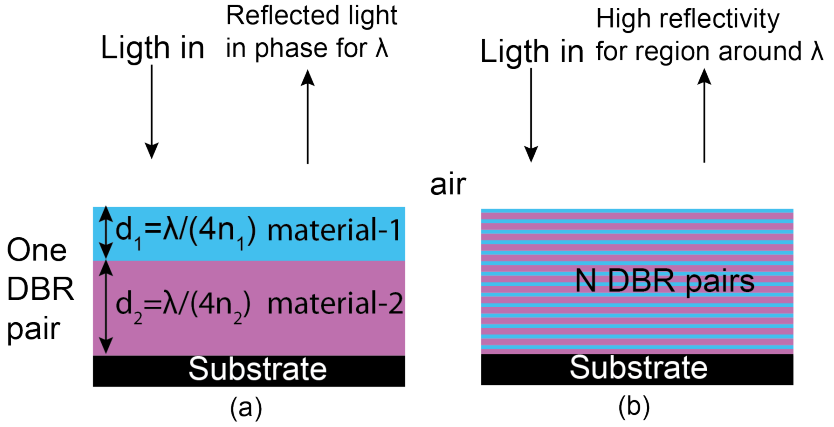


Figure 2.3: Schematic of a DBR. One $\lambda/4$ pair of two materials (a). A stack of $\lambda/4$ pairs (b).

2.2.2 DBR - design strategy

A DBR is mainly characterized by its reflectance in, as given by equation 2.2 which is based on the transfer matrix formulation [2] for incident, reflected and transmitted electromagnetic waves for a center wavelength λ .

$$R(N) = \left(\frac{1 - \frac{n_2^2}{n_s n_0} \left(\frac{n_1}{n_2} \right)^{2N}}{1 + \frac{n_2^2}{n_s n_0} \left(\frac{n_1}{n_2} \right)^{2N}} \right)^2 \quad (2.2)$$

Here, N is the number of pairs of materials 1 and 2, n_1 , n_2 , n_s , n_0 are the refractive indices for materials 1 and 2, the substrate and the region above material 1 in Fig. 2.3. The region with high reflectivity is the stop band of the incident electromagnetic wave. The wave will not be transmitted through the material in the stop band. Instead the light is reflected. Important consideration when designing a DBR is given in the following list.

High refractive index difference: A large refractive index difference n_1 - n_2 means that a smaller number of $\lambda/4$ periods is needed to achieve a specific reflectance. The refractive index difference between ZnO and GaN is (≈ 0.4) at 450 nm.

Well defined layer thickness: The thickness of a period must fulfill the $\lambda/4$ criterion.

Abrupt interfaces: Smooth interfaces are needed to avoid scattering effects.

2.3 Thermal properties

The thermal properties of a semiconductor are of importance for the epitaxial growth since thermal mismatch between the thermal expansion coefficients can lead to strain and crack formation.

Table 2.1 lists the thermal expansion coefficients for GaN and ZnO. The data for the GaN was given for the temperatures 100-600 K in [41]. The thermal expansion coefficients for ZnO are given at room temperature in table 2.1. However, the expansion was measured with powder X-ray diffraction (XRD) for temperatures between 200-1400° and fitted to the following analytical functions for the lattice constant a and c for ZnO [5].

$$a = 3.2468 + 0.623 \times 10^{-5}T + 12.94 \times 10^{-9}T^2 \quad (2.3)$$

$$c = 5.2042 + 0.252 \times 10^{-5}T + 11.13 \times 10^{-9}T^2 \quad (2.4)$$

The thermal conductivity for GaN and ZnO can be measured with the scanning probe microscopy (SPM)-method scanning thermal measurement (SThM). The higher value of 1.16 W/cmK corresponds to the Zn-polar and the lower value of 1.1 W/cmK to the O-polar bulk values. Higher values up to 1.47 W/cmK for the thermal bulk conductivity have also been reported for N-plasma treated melt grown crystals [5] and is closer to the reported values for GaN.

Chapter 3

Epitaxy

This chapter gives a basic introduction to epitaxy. A description of the hybrid nitride and oxide MBE-system used to fabricate the samples in this work, is also provided.

3.1 Introduction

The word epitaxy comes from the greek words *epi* meaning above and *taxis* meaning in ordered manner and was introduced by Royer 1928 [59]. By definition epitaxy involves the process of depositing or growing a crystalline layer on a crystalline substrate. Epitaxy is necessary to fabricate various semiconductor structures for applications such as laser diodes and light-emitting diodes.

Similar to other epitaxial methods, the MBE process involves the nucleation of nuclei or islands of a crystalline material on the substrate surface followed by the coalescence of these islands into a single crystal layer.

The processes in MBE are usually far away from thermodynamic equilibrium and are therefore better described by kinetic models that involve mass transport and adsorption, desorption, diffusion, incorporation, decomposition and growth rates.

Atomistic models describe the interaction between single atoms and gives for instance the bond strength and bond length between the atoms Wurtzite crystal [Fig. 2.1, chapter 2]. The quantum mechanical aspects on this length-scale (nm) has to be taken into account for the description of the chemical bonding between impinging atoms and substrate atoms via their respective atomic or molecular orbitals [60].

A unique and unparalleled advantage of MBE is that it is possible to identify different growth modes *in real-time* by the observation of different reflection high

energy electron diffraction (RHEED) patterns with the help of a RHEED system that is an integral component in most MBE systems.

Homoepitaxy refers to the case when the deposited or grown material is the same as the substrate material. This case does therefore not induce lattice strain in the film-substrate interface since the lattice constants are the same. Consequently, homoepitaxy yields high-quality thin films such as ZnO films grown on ZnO substrates. [9]

3.1.1 Heteroepitaxy

Heteroepitaxy refers to the case when the grown material is different from the substrate material. Heteroepitaxy can be further divided into either lattice matched or lattice mismatched growth.

Heteroepitaxy can combine semiconductor materials with different electrical or optical properties that enable new compound materials with novel properties. For instance, by precisely combining thin layers of GaN and InGaN compounds into QWs LEDs and laserdiodes emitting in the UV-violet-blue and green spectral range, can be fabricated.

For optical applications, a crack free conductive AlN/GaN DBR exhibiting a reflectance $R \geq 99\%$ and with a stopband of 40-50 nm centered around 450 nm has been demonstrated [61]. This MBE-grown DBR consisted of 20 pairs of lattice-mismatched AlN/GaN-layers grown on a 6H-SiC(0001)-substrate. The structure is suitable for optoelectronic applications in the blue-green spectral range.

A crack-free 40-pair lattice matched $\text{In}_{0,17}\text{Al}_{0,83}\text{N}/\text{GaN}$ DBR has been grown on a 2-inch *c*-plane sapphire substrate by MOCVD. The thickness of each $\text{In}_{0,17}\text{Al}_{0,83}\text{N}/\text{GaN}$ -pair was 47/50 nm. The R of this DBR was 99.4% with a bandwidth of 30 nm centered at 450 nm [62]. A higher number of pairs was needed in the lattice matched DBR since the refractive index contrast between the layers was lower compared with the lattice-mismatched AlN/GaN DBR [61].

The lattice mismatch in heteroepitaxy is measured by the misfit parameter f_m defined as

$$f_m = \frac{a_l - a_{sub}}{a_{sub}} \quad (3.1)$$

where a_l and a_{sub} are the lattice constants of the epitaxial layer and the substrate, respectively [63]. The lattice mismatch initially results in the accumulation of either compressive or tensile strain. Above a certain critical thickness, the strain becomes so large that the strained layer relaxes through the formation of dislocations and cracks. Dislocations reduce the periodicity of the crystal structure. A lower crystal periodicity translates to a lower structural quality.

3.1.2 Growth modes

Figure 3.1 shows three different types of structures grown in this work. The images are obtained with scanning electron microscopy (SEM) (see chapter 4.1).

The main growth modes in epitaxy are classified as follows [59]:

Frank-van der Merwe growth mode (FM-mode): Layer by layer growth. One layer is grown before the growth of the next layer starts.

Step-flow growth mode (SF-mode): Adatom diffusion along steps or step-flow. The layer advances along the step.

Stranski-Krastanov growth mode (SK-mode): 2D-layer growth followed by formation of 3D-island [Fig. 3.1(a)].

Volmer-Weber growth mode (VW-mode): 3D-island growth [Fig. 3.1(c)].

Columnar growth mode (CG-mode): 3D-island growth followed by coalescence. The islands merge and form a film [Fig. 3.1(b)].

3.1.3 Epitaxy - atomistic description

Mass-transport, adsorption, diffusion and incorporation are the key mechanisms in the kinetic atomistic description of epitaxy which is important in MBE [64–67].

Figure 3.2 shows a schematic description on the atomistic view of epitaxy and is referred to as Kossel’s model of crystallization [59]. This model is also called the terrace step kink model (TSK) model [68].

The schematic shows a cubic lattice and describes the basic processes involved in homoepitaxy. Each atom is viewed as a building block with six faces where each face has one possibility to interact and bond to another surface. The substrate at temperature T is viewed as many building blocks put together into a single crystal and each position is considered as a site. The substrate has a lower, a middle and an upper terrace each separated with a vertical step height which is one building block high. The length L is defined as the terrace or step length. The number of bonds indicated at each site are (1) on a terrace, (2) at a step, (3) at a kink, (4) at a step vacancy and (5) at a terrace vacancy.

An impinging flux of atoms arrive at the substrate where they adhere to the surface [Fig. 3.2 (lower terrace)]. The physisorbed state represent the weakest bond formed between the adatom and the substrate. Desorption is the process when a physisorbed adatom leaves the surface. The physisorbed adatom is free to move or diffuse on the surface between different sites over flat surfaces, over steps or over islands [69]. Chemisorption is the process when the adatom binds to the surface and is thus incorporated into the growing layer. A higher growth temperature increases the desorption from the substrate. A higher source temperature will increase the flux of impinging atoms onto the surface.

Diffusion can also occur along steps and bind at a more preferable kink site [Fig. 3.2 (middle terrace)]. Nucleus 1, 2 and 3 are 2D-islands and represent nucleation. Nucleus 1 shows a small nucleus dissociating. A nucleus can also diffuse on the substrate and become incorporated into a larger nucleus. The process where nuclei merge is called

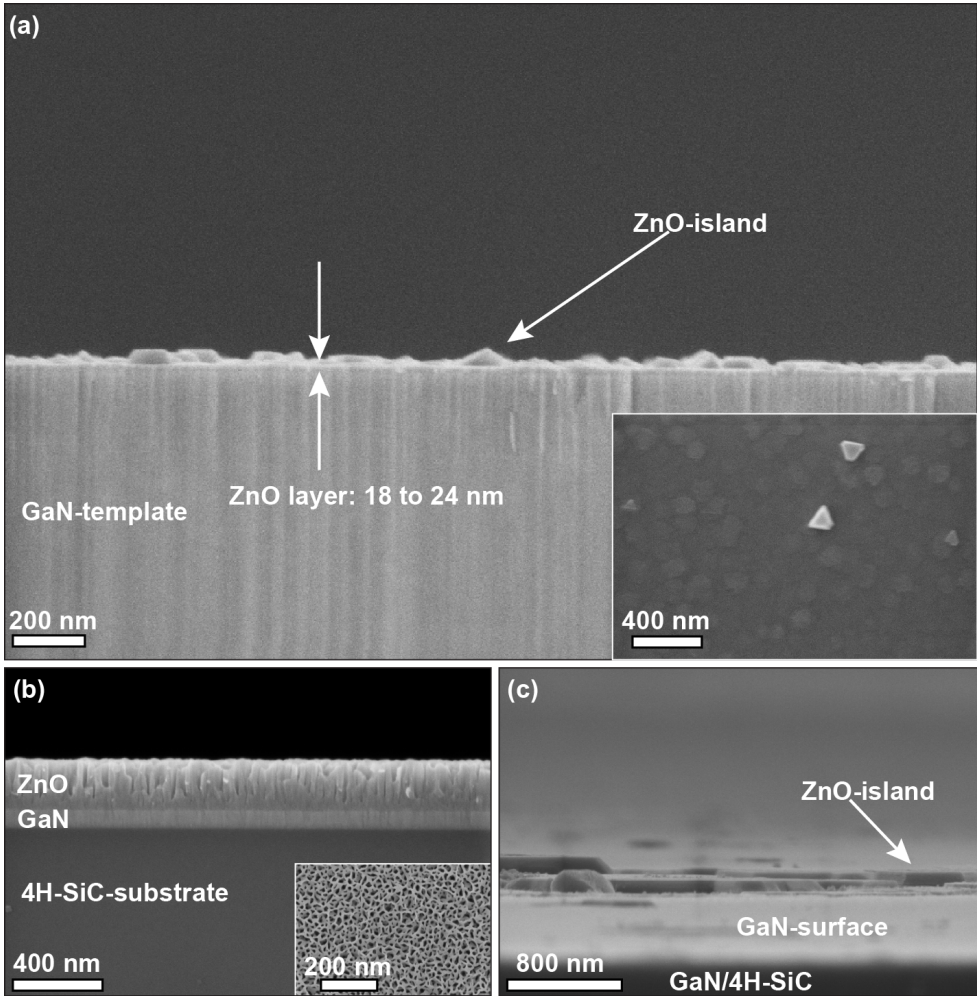


Figure 3.1: SEM micrographs of different ZnO-growths on different GaN(0001)-surfaces. (a) Cross-section SEM image of a sample with a thin ZnO layer and islands. The insert shows an SEM image of the surface of this sample (m1041). (b) A cross-section SEM image of a columnar ZnO layer grown on in-situ grown GaN/4H-SiC. The insert shows the SEM image of the sample (m1113). (c) SEM micrograph of a sample with ZnO islands on GaN/4H-SiC (m1128)

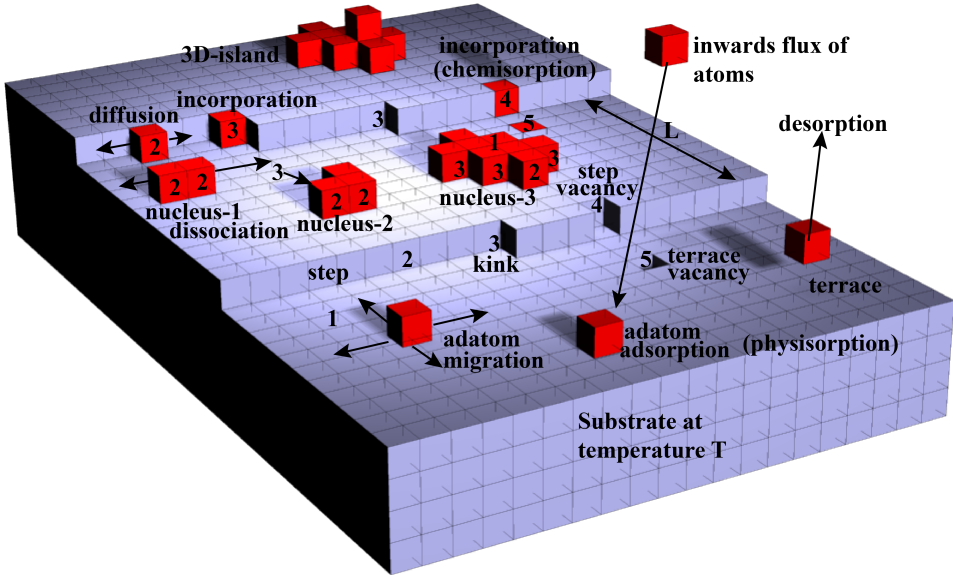


Figure 3.2: Schematic description of the atomistic view of homoepitaxial growth. Atoms impinge on the substrate, where they adhere. The step-length of the terraces is L . Diffusion of adatoms will occur as long as they are not bound strongly to the substrate. The bond strengths for a specific site is increasing with increasing number 1-5. An adatom is incorporated into the substrate when it stops to migrate and becomes chemisorbed. Desorption of an adatom can occur before incorporation. 2D-nucleation is shown for different sizes of nuclei where the smallest nucleus both can migrate on the surface as well as dissociate. A 3D-nucleus is formed at the highest terrace. The rates for all reactions on the surface are greatly affected by the substrate temperature T .

coalescence [70]. A larger 2D-island have a higher number of possible binding sites and therefore grow faster compared with a smaller nucleus.

The diffusion length of an adatom is defined as the average length the adatom moves on the surface before desorption or incorporation occurs. If the diffusion length is smaller than the terrace or step length, the growth mode will yield 2D-islands on the terraces (FM-mode). SF-mode mode will occur when the diffusion length is larger than the terrace or step length [71].

A 3D-island is formed if the vertical growth rate is larger than the rate of growth in the lateral direction [Fig. 3.2(upper terrace)].

3.2 MBE technology - Nitrides and Oxides

Figure 3.3 shows a schematic of the refurbished MBE360-system used to grow ZnO and GaN using the same growth chamber. There are also two additional chambers used for sample transfer between ambient and the growth chamber. The growth of GaN and ZnO in one single chamber is extremely rare and to our knowledge only been reported previously by M.A.L Johnson et al. [22].

3.2.1 Ultra high vacuum

The base pressure (standby condition) of the growth chamber is maintained with an ion pump and a cryo-pump. The base pressure is measured with an ion-gauge to 5×10^{-10} Torr. During growth, the ion-pump is turned off since the growth pressure is above the ion-pump capacity. The cryo-pump is regulating the pressure during the growth and is assisted by cryo-panels filled with liquid nitrogen. The pressure range during the growths was 3.0×10^{-6} – 5.0×10^{-5} Torr depending on the O_2 flow rate Φ_{O_2} or the N_2 flow rate Φ_{N_2} .

3.2.2 Substrate heater, sample mounting and transfer

The samples were In-mounted (soldered) on a 50 mm diameter Si(100)-wafer attached to a ring-shaped Mo-holder. The Mo-holder is loaded into the load-lock and transferred via the buffer-chamber into the growth chamber onto the continuous azimuthal rotation (CAR)-unit. The CAR-unit is a manipulator stage with the possibility to move in the x-, y- and z-directions as well as z-rotation. The uniformity of the grown layer is improved by the continuous azimuthal rotation of the substrate holder around its surface normal (y-axis in figure 3.3). All samples were continuously rotated at 6 rpm during the growth experiments. The substrate heater is a Ta-circuit inside a pyrolytic boron nitride (PBN) fixture. The temperature of the heater is measured with a W/Rh thermocouple located on the back of the Mo-holder and behind the substrate back-surface. Thus, the actual temperature on the substrate surface differs from the one measured.

3.2.3 Solid effusion cells

A solid source effusion cell loaded with 7N Ga is used to provide elemental Ga. Elemental Zn is provided by a solid source effusion cell filled with 6N Zn. Both elements are contained in crucibles made of PBN. The Ga-source is usually operated between 1000-1120 °C for growth of GaN. A PBN aperture-plate with an aperture diameter of 7 mm was positioned over the orifice of the Zn-crucible to minimize oxidation of the source material [72]. The aperture plate also provides additional control of the Zn-flux. The Zn source is operated between 290-440 ° during growth of ZnO. The temperature

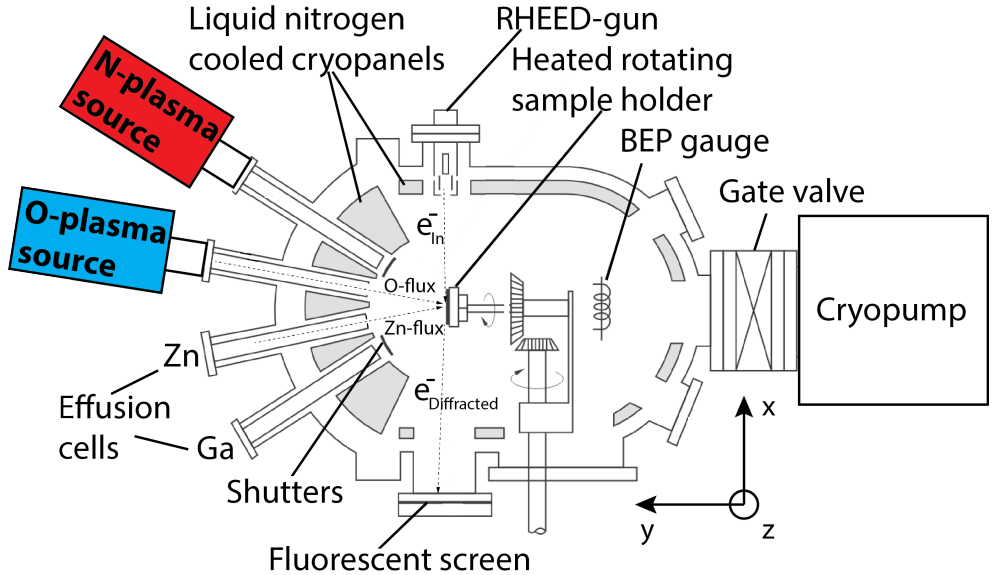


Figure 3.3: Schematic of a hybrid MBE-system for growth of GaN and ZnO using the same growth chamber. The shutters in front of the Zn- and O-sources regulate the flux of Zn- and O-atoms towards the heated substrate which is mounted on a rotating sample holder. Real-time in-situ observation of the growth is possible by monitoring the RHEED-pattern on the fluorescent screen. The GaN-growth is performed analogously.

is measured with a W/Rh thermocouple in contact with the crucible. Shutters are located in front of all sources. Shuttering enables or disables the flux of elements from a specific source.

3.2.4 Nitrogen and Oxygen plasma sources

A N-plasma source (Veeco) supplied with 7N N₂ is used for producing active N. An O-plasma source (Veeco) supplied with 6N O₂ for producing active O. Each plasma source is equipped with a conduction tube protruding into the growth chamber. This is a non-standard solution that was necessary to allow mechanical mounting of the plasma-sources on the growth chamber since the available flange size on the MBE-360 is 2.75" while the flange size for the plasma sources is 4.5". The conduction tubes lower the growth rate by a factor 2–4. The flow-rate of O₂ and N₂ are each controlled with a 5 standard cubic centimeter (sccm) mass flow controller. The plasma for each source can be maintained between 0.2–5.0 sccm. Both plasma sources can be operated

in either low-brightness or high-brightness mode. All grown samples have been grown in high-brightness mode. The difference between the modes can be observed through a viewport located on the end of each plasma source.

3.2.5 Reflection High Energy Electron Diffraction

The RHEED-system is an in-situ characterization tool used to monitor the growth process in real-time. It has two major parts, a 10 kV RHEED-gun and a fluorescent RHEED-screen mounted diametrically opposite to the gun. The electrons from the gun can be adjusted at a glancing angle $< 3^\circ$ with respect to the mounted substrate located in the xz-plane. The electrons will be scattered or reflected by the surface and also diffracted in the case of an ordered surface such as an epitaxial layer. The diffraction pattern can be observed on the RHEED-screen. This pattern depends on the electron acceleration voltage, the lateral and vertical coherence length of the electrons and the condition of the surface [73, 74]. With reference to the three terraces described in figure 3.2 the following will be observed with the RHEED-system:

Figure 3.2(Lower terrace): Streaks.

Figure 3.2(Middle terrace): Streaks but with a lower intensity due to population of the surface with 2D-islands.

Figure 3.2(Upper terrace): Spots if completely covered with 3D-islands and a combination of spots and streaks if the surface is partially covered with 3D-islands.

Observation of rings and ring segments indicates a polycrystalline surface. A polycrystal consists of small crystalline domains that are randomly ordered with respect to each other and to the substrate surface. This therefore no longer represents epitaxy.

3.2.6 The BEP-gauge

The beam equivalent pressure (BEP)-gauge is mounted on the CAR-unit on the opposite side of the substrate heater. When rotated toward the sources the gauge can detect a flux of Ga or Zn atoms. The BEP-gauge gives a qualitative measure of the atoms/s emitted from the source. The flux of atoms is conveniently plotted as a function of the source temperature and this is useful for the calibration of the flux. It also indicates when a solid source is empty and needs to be refilled.

Chapter 4

Characterization Techniques

This chapter introduces the characterization methods used for the structural, morphological, electrical and optical characterization of the epitaxial layers described in this thesis. It also describes the optical emission spectroscopy setup used to assess the oxygen plasma composition.

4.1 Scanning electron microscopy

With SEM it is possible displaying sample images with a lateral resolution of 3–6 nm. In SEM, electrons that are emitted from a field emission filament located in ultra high vacuum (UHV) are accelerated with a high voltage (2–20 kV) and directed through a system of electron lenses and apertures before striking the sample surface. The interaction between the incident electrons and the sample surface will result in the emission of secondary, Auger and backscattered electrons. The secondary electrons emitted from the sample, are collected by a detector. The detector signals are processed electronically and ultimately form an image [75].

In this work a LEO Ultra FEG 55 SEM was used to characterize the samples. This SEM was operated with a 5 kV acceleration voltage and with a 7.5 μm aperture. Plane-view images of the sample surfaces provided information of the surface morphology as shown in figure 4.1(a) for a ZnO/GaN-structure grown on 4H-SiC(0001).

The samples were cleaved manually with a diamond scribe to expose a cross-section of the sample edge for thickness measurements [Fig. 4.1(b)]. The cleaved sample was mounted on the sample holder so that the cross-section faced the detector. A secondary electron (SE) detector was used for an initial coarse adjustment before

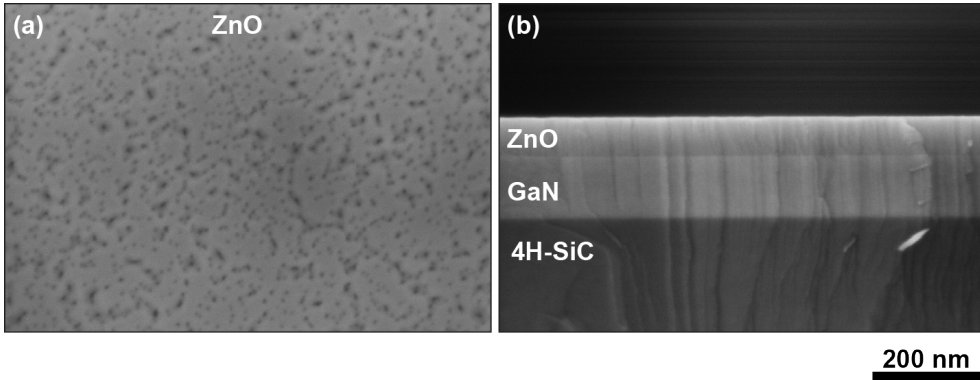


Figure 4.1: SEM micrographs for MBE-grown ZnO on in situ grown GaN/4H-SiC (sample m1095). A plane-view image of the surface (a) and a cross-section micrograph of the cleaved sample edge (b).

enabling the high-resolution InLens detector. An improved image quality was achieved with a lower line scan speed and by averaging the detector signal up to 256 times. From the cross-sectional images, the thicknesses of the layers could be determined with an accuracy of ± 5 nm. The growth rate was then calculated by dividing the measured thickness with the growth time.

4.2 Atomic force microscopy

The surface morphology (topography) of a samples were investigated with atomic force microscopy (AFM) [76], [77]. In AFM, a sharp tip located on the edge of a cantilever scans the sample surface. The tip-surface atomic force interaction causes the cantilever to deflect and the degree of deflection is recorded by a laser-photodetector system. The photodetector signal is used by a closed-loop piezoelectric setup to which the cantilever is attached. The piezoelectric setup moves the cantilever in a direction that is parallel to the surface normal of the sample (height or z-coordinate). The closed-loop configuration will try to maintain a constant tip-sample interaction. A topographical map of the surface can therefore be obtained since every z-value is associated with a surface x- and y-coordinate. In this work, the AFM micrographs were recorded using a Bruker Dimension 3100 system in tapping mode and under ambient conditions.

Figure 4.2 (a) shows a SEM image of the probe tip. A schematic of the tip and the cantilever assembly is shown in Fig. 4.2 (b). An AFM micrograph of a GaN(0001)/Al₂O₃-template is shown in Fig. 4.2 (c). The GaN surface exhibited curved

terraces that were 0.23 nm high and 80 nm wide as indicated in the figure. The the peak-to-valley distance (z -value) was 0.9 nm over a $2 \times 2 \mu\text{m}$ scan area. The probe

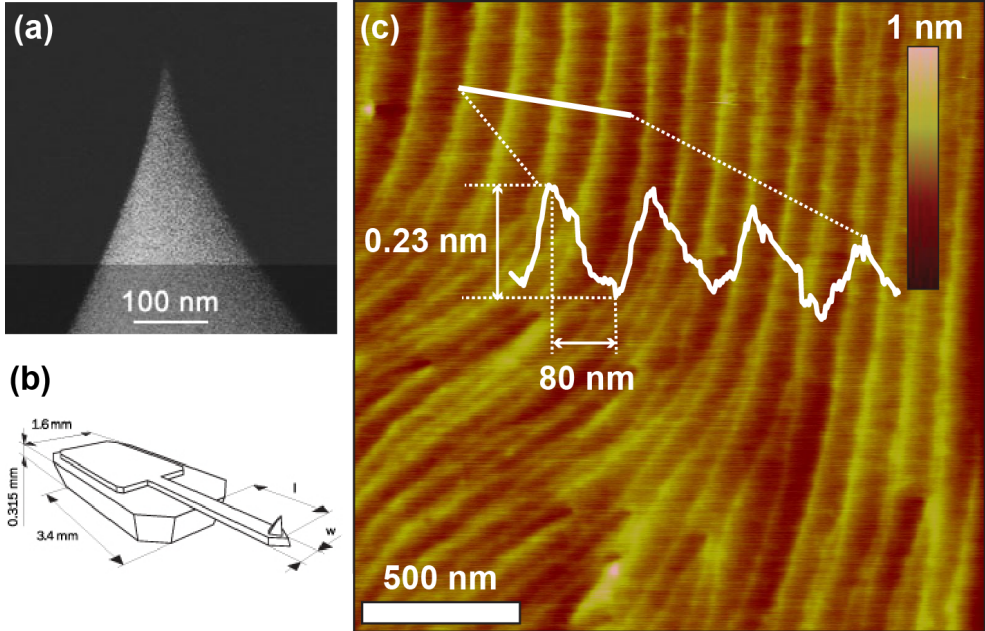


Figure 4.2: SEM image of an AFM probe tip (a) and the schematic for the tip-cantilever assembly (b). AFM micrograph of GaN(0001)/Al₂O₃-template surface (c). The white line indicates the height and length of the terraces.

tips used (HQ:NSC15/Al BS) had an uncoated tip diameter of 8 nm. The full tip cone angle was 40° and the total tip height was 12–18 μm . The cantilever force constant was 40 N/m and the resonance frequency was ≈ 325 kHz [78]. A z -range of 1–3 μm was used. Images were captured over 2–5 μm areas with scan speeds of 1–2 Hz. For all measurements the image artifacts [79] were minimized by observation of the real-time lines of the trace and re-trace which should be identical.

4.3 X-ray diffraction

The structural properties of a material can be investigated analyzing the diffracted x-ray pattern of an epitaxial layer that is irradiated by x-rays from an x-ray source.

4. CHARACTERIZATION TECHNIQUES

The fundamental relation between the incident x-ray beam and the crystal structure of the epitaxial film is expressed by Bragg's law

$$n\lambda = 2d \sin \theta \quad (4.1)$$

where $n=1,2,3..$ is an integer representing the diffraction order, λ is the wavelength of the incident X-ray beam ($\lambda = 0.154056$ nm), d is the distance between the crystal planes and θ is the angle between the crystal planes and the incident beam as well as for the diffracted beam.

Figure 4.3(a) illustrates fundamental geometry behind Bragg's law. The sample surface normal \hat{s} is here parallel with the lattice plane normal \hat{n} . It is common to denote the incident angle with ω instead of θ as indicated in Fig. 4.3(a).

The distance between the crystal planes for a hexagonal crystal structure is given by

$$d(h, k, l) = 1/\sqrt{(h^2 + k^2 + l^2) \frac{4}{3a^2} + \frac{l^2}{c^2}} \quad (4.2)$$

where h,k,l are the Miller indices and a and c are the lattice constants of the hexagonal unit cell [80].

In figure 4.3(a) the angular change of direction between the incident and diffracted X-rays is 2θ with respect to ω . If n,λ and 2θ are known, it is possible to determine the plane distance d which can be used to identify a specific crystalline material. This x-ray scan configuration is called symmetric or on-axis.

Figure 4.3(b) shows two asymmetric reflection geometries that make it possible to determine the positions of diffraction peaks from crystal planes that are not parallel to the sample surface $\hat{n} \nparallel \hat{s}$. The incident and diffracted x-ray beams and the \hat{n} and \hat{s} are still located in the same plane. Here, the angle of incidence with respect to the sample surface is either lower $\omega - \Delta$ or higher $\omega + \Delta$ as compared with the symmetric Bragg reflection condition. The diffracted beam is changed correspondingly with $2\theta + \Delta$ and $2\theta - \Delta$ as indicated in Fig. 4.3(b). In order to fulfill the Bragg conditions for these planes, the detector and sample must be rotated to specific angles assuming that the incident beam geometry is fixed which is the case for many common diffractometer systems. This will limit the number of planes or Bragg reflections that are accessible by the diffractometer. Asymmetric scan geometries are also called an off-axis scans since $\hat{n} \nparallel \hat{s}$.

In skew geometry scans, the sample is rotated both in the plane for the incident and diffracted beams [Fig. 4.3(b)] as well as out of this plane as indicated in Fig. 4.3(c).

By performing a scan where only ω is changed and the detector is wide-open, the sample is "rocked" through the Bragg condition for a reflection (hkl). This type of scan is thus called a rocking-curve. If a very wide scan-range is needed, the detector angle is changed with 2θ where still $\omega = \theta$.

A deviation from the ideal crystal configuration as observed for real crystalline materials such as ZnO and GaN which have the wurtzite crystal structure, will affect the diffracted x-ray pattern. This can be used to assess the crystal quality of the film.

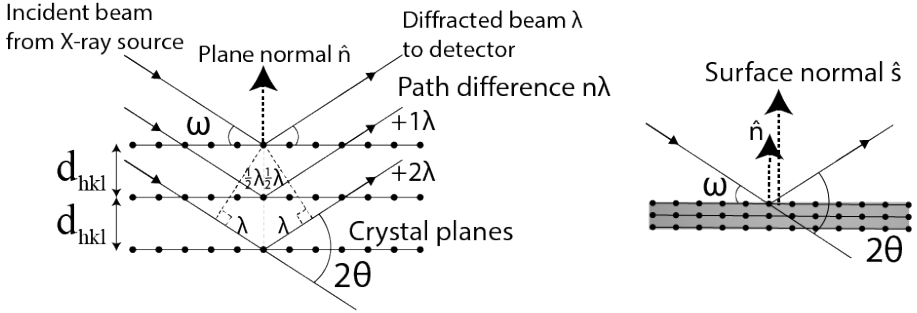
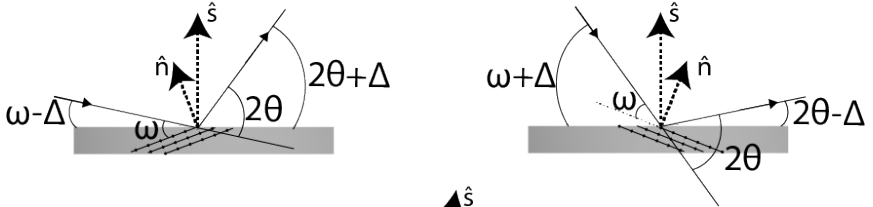
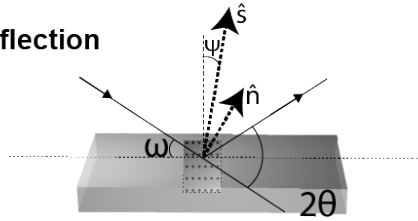
(a) Bragg's law, symmetric reflection**(b) Asymmetric reflections****(c) Skew symmetric reflection**

Figure 4.3: Bragg's law for symmetric (a), asymmetric (b) and skew symmetric (c) reflection geometries.

In hexagonal crystal structures with a pronounced mosaic component such as GaN and ZnO, the on-axis symmetric rocking curve yields the tilt that is related to threading dislocations that have a Burgers vector \mathbf{b} parallel to the $\langle 0001 \rangle$ direction which is the case for pure screw dislocations. The skew-geometry rocking curve gives the twist related to pure edge dislocations which are threading dislocations that have a \mathbf{b} parallel to $\langle 1000 \rangle$. Two scans are thus necessary to give a comprehensive assessment of the structural quality of a wurtzite material such as ZnO and GaN. Mixed screw-edge threading dislocations have components of both \mathbf{b} .

The crystal or structural quality is assessed by measuring the full-width-at-half-

4. CHARACTERIZATION TECHNIQUES

maximum (FWHM) of a diffraction peaks obtained from on- and off-axis scans where the off-axis scan is performed in the skew-geometry configuration. The FWHM of the on-axis scan is a measure of the tilt $\Delta\omega_s$ of the layer whereas the FWHM from the skew-geometry scan is a measure of the layer twist $\Delta\omega_e$. A narrow FWHM of the diffraction peak corresponds to a better crystalline quality.

It has been shown that it is possible [81–83] to obtain an estimate of the amount of screw and edge dislocations from the tilt and twist measurements through the relations

$$\rho_s = \frac{\Delta\omega_s^2}{2\pi \ln 2 |\mathbf{b}_s|^2} \quad (4.3)$$

$$\rho_e = \frac{\Delta\omega_e^2}{2\pi \ln 2 |\mathbf{b}_e|^2} \quad (4.4)$$

where ρ_s and ρ_e are the concentrations of screw and edge dislocations, respectively, \mathbf{b}_s and \mathbf{b}_e are the corresponding Burgers vectors and $\Delta\omega_s$ and $\Delta\omega_e$ is the tilt and twist in radians.

From a set of individual $\omega/2\theta$ scans which are performed with a crystal in front of the detector and for a set of ω values, it is possible to obtain a map of the Bragg reflection peak and the surrounding region in the reciprocal space. A reciprocal space map can be displayed in angular units ($\Delta\omega$, $\omega/2\theta$) or in reciprocal units (Q_x , Q_y) using the coordinate transformation

$$Q_x = R(\cos \omega - \cos(2\theta - \omega)) \quad (4.5)$$

$$Q_y = R(\sin \omega + \sin(2\theta - \omega)) \quad (4.6)$$

$$|Q| = \sqrt{Q_x^2 + Q_y^2} = 2R \sin \theta \quad (4.7)$$

where R is the radius of the Ewald sphere and $|Q|$ is the length of the diffraction vector [80, 84]. An $\omega/2\theta$ -scan converted to reciprocal units will be a radial line if extended to the origin in a (Q_x , Q_y) graph and is therefore also called a radial scan. In a reciprocal space map, the vertical position of a reflection is related to the out of plane lattice constant c and the horizontal position is related to the in-plane lattice constant a . A symmetric on-axis reflection for a relaxed ZnO/GaN layer will have the same Q_x -value since this measurement is insensitive to the in-plane lattice constant. On the other hand, an asymmetric reflection for the relaxed ZnO/GaN layer will exhibit different Q_x positions for the ZnO and GaN peaks since the in-plane lattice constants are different. For a fully strained ZnO/GaN-layer the Q_x -positions for the ZnO and GaN peaks coincide in an asymmetric geometry reflecting the identical in-plane lattice constants for ZnO and GaN.

In this work, a Philips X'Pert Materials Research Diffractometer (MRD) was used for the characterization of the grown ZnO and GaN layers (papers I – III) and ZnO/GaN DBRs (paper V). A symmetric configuration was used for the rocking curve

scans across the (0002) reflection. The rocking curve scans across the (10 $\bar{1}$ 5) reflection were obtained in a skew symmetric configuration. Reciprocal space maps were acquired with an asymmetric configuration (with a high angle of incidence) across the (10 $\bar{1}$ 5) reflection and in a symmetric configuration across the (0002) reflection.

4.4 Time of flight secondary ion mass spectroscopy

A unique capability of time of flight secondary ion mass spectroscopy (TOF-SIMS) is elemental mapping of a surface. The working principle of this instrument is based on a primary ion beam directed against the sample surface. The primary beam creates a sputtering effect which generate secondary ions that are then removed from the sample. The secondary ions are collected and detected by through a mass detector and are ultimately yielding a mass spectrum [85].

In this work an IONTOF V [86] was used for a qualitative characterization of grown ZnO layers on GaN(0001)/Al₂O₃ templates [Paper I]. The primary beam was either Bi or Cs. Two instrument modes can be used, the high-current bunch mode and the burst alignment mode. The high-current bunch mode is associated with a lower spatial resolution of 2–5 μm but with the highest mass resolution. The burst alignment mode, which was used in this work, is associated with a lower mass resolution and broader peaks but with a high lateral resolution (≈ 200 nm) [87]. Depth profiling of grown layers was also performed.

4.5 Transmission Electron Microscopy

With transmission electron microscopy (TEM) it is possible to display specimen images with an atomic resolution. The generation of electrons in a transmission electron microscope is similar to that in an SEM, but the electrons are accelerated with a much higher energy (80–300 kV). The electrons are directed against, and transmitted through a thin slice of the specimen material. The interaction volume is therefore small. A detector records the electrons from the sample. Both a direct image or a diffraction pattern from the specimen can be obtained [88]

In this work the morphology and crystal structure of ZnO/GaN DBRs were investigated with a Jeol 3000F TEM equipped with a field emission gun (FEG) and operating at 300 kV [paper V]. A FEI Nova NanoLab 600 DualBeam focused ion beam (FIB)/SEM system was used to prepare the cross-sectional TEM lamellae with a maximum thickness of 300 nm. This is the first time both specimen preparation and TEM-analysis have been made on ZnO/GaN DBRs.

4.6 Spectral Reflectance Measurements

In paper V the reflectance was measured for the ZnO/GaN DBRs. Figure 4.4 shows a schematic of the employed reflectance setup together with a photo of a cleaved 20-period ZnO(000 $\bar{1}$)/GaN DBR (sample S1-55) and the recorded reflectance. The

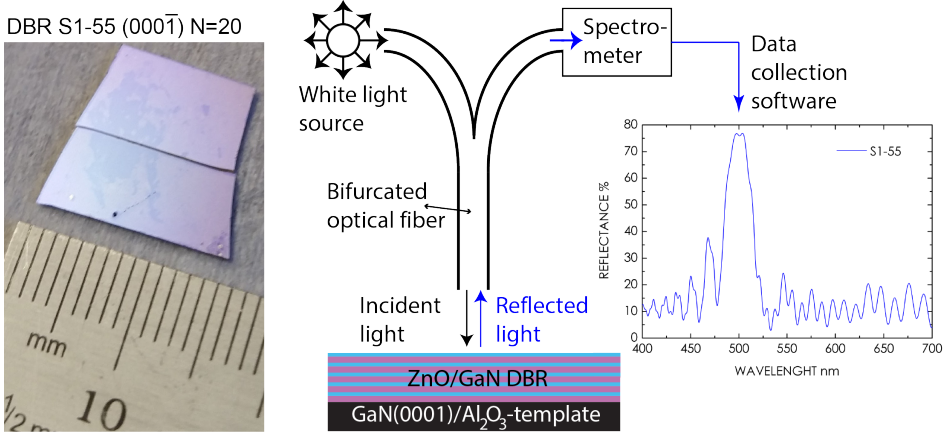


Figure 4.4: A cleaved 20-period ZnO(000 $\bar{1}$)/GaN DBR (left) with a schematic spectral reflectance setup (center) and with the recorded reflectance (right).

sample is illuminated at normal incidence with white light from a Xe-lamp (Thorlabs OSL1-EC) through a bifurcated reflection probe with one bundled illumination and one detection fiber. The detection fiber collects the reflected light from the sample and directs it into a Avantes AvaSpec 3648 spectrometer used for wavelengths λ in the 350–800 nm range. The diameter of the spot size on the sample was ≈ 2 mm. The spectrometer is connected with a USB-cable to a computer with a data collection software. Before each measurement the Xe-lamp was stabilized for 5 min. The dark intensity signal I_{dark} from the ambient was measured to assess signal noise floor. The measured intensity from a Si-wafer I_{ref} which has a known reflectivity R_{ref} , was recorded. The sample reflectivity R_{sample} is then given by:

$$R_{sample} = R_{ref} \frac{I_{sample} - I_{dark}}{I_{ref} - I_{dark}} \quad (4.8)$$

over the entire 350–800 nm wavelength range [89]. Based on the reflectance from the reference sample, the measurement error was estimated to be $\approx 5\%$ for $\lambda < 400$ nm and $< 1\%$ for $400 \text{ nm} < \lambda < 800$ nm. A comparison between the measured reflectivity from a GaN/Al₂O₃ template with and without In on the backside showed that the In film

did not affect the reflectivity. From this we concluded that it was possible to measure the reflectivity from each ZnO/GaN sample without removing the In on the backside.

4.7 Electrical characterization

The electrical properties of the grown samples were assessed with Hall-effect measurements using the van-der Pauw geometry [90] [91] shown in Fig. 4.5(a). Figure 4.5(b) illustrates the Hall-effect geometry. When a current I is driven through a sample with

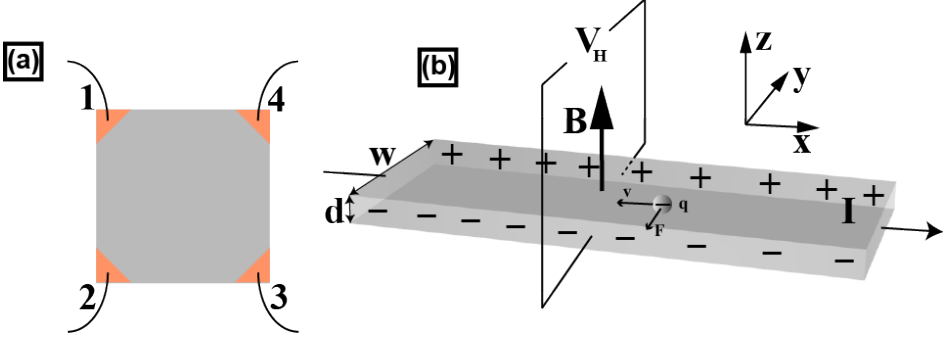


Figure 4.5: Van der Pauw geometry with contacts in the corners of a square sample (a). The Hall-effect geometry (b).

a carrier concentration n together with a magnetic field \mathbf{B} applied perpendicular to the current, charges accumulate on the opposite sides of the sample which create a transverse Hall voltage V_H that can be measured. The Hall voltage can be derived from the expression for the Lorentz force \mathbf{F} as given by $\mathbf{F} = q(\mathbf{E} + \mathbf{v} \times \mathbf{B})$ where q is the charge carrier with the drift velocity v . The carrier sheet density n_s is given by

$$n_s = \frac{IB}{q|V_H|}. \quad (4.9)$$

from which the carrier concentration can be calculated as $n = n_s/d$ for a known sample thickness d . The Hall-voltage V_H is negative for n-type carriers and positive for p-type carriers.

From the van-der Pauw configuration shown in Fig. 4.5(a), the Hall-voltage would be V_{24} for a current I_{13} . From the resistivity measurements $R_A = V_{43}/I_{12}$ and $R_B = V_{14}/I_{23}$ it is possible to determine the sheet resistivity R_s by solving the van der Pauw equation

$$e^{-\frac{nR_A}{R_s}} + e^{-\frac{nR_B}{R_s}} = 1 \quad (4.10)$$

which can be used to obtain the mobility μ with

$$\mu = \frac{|V_H|}{R_s I B}. \quad (4.11)$$

Usually the average is taken over a number of measurements with the magnetic field directed in both directions of the sample and with all combinations of voltage and current through the contacts 1–4.

In this work, a commercial HL5500 Hall-effect room temperature measurement setup was used with software from Nanometrics Inc. Cross-sectional SEM was used to determine the layer thickness d . The Hall samples were $5 \times 5 \text{ mm}^2$ and were cut out from the grown $13 \times 13 \text{ mm}^2$ sample in order to remove any inhomogeneous edge effects of the grown layer. The contacts consisting of Au(60 nm)/Ni(20 nm) were fabricated with e-beam evaporation and exhibited ohmic behavior on both ZnO and GaN layers. The measurements were performed under dark conditions and a sample current of 0.1 mA was employed. The background electron carrier concentration in the ZnO layers was $1 \times 10^{19} \text{ cm}^{-3}$ with $\mu = 51 \text{ cm}^2/\text{Vs}$ and R_s of $1123 \text{ }\Omega/\square$. The n-type carrier concentration for the GaN-layers was $1.8 \times 10^{18} \text{ cm}^{-3}$ with $\mu = 108 \text{ cm}^2/\text{Vs}$ and R_s of $1058 \text{ }\Omega/\square$.

4.8 Optical emission spectroscopy

The amount of active O in the O-plasma provided by the O-plasma source, was determined with optical emission spectroscopy [92, 93]. Figure 4.6(a–e) shows the optical emission spectroscopy setup used in this work [paper IV].

The interior of the O-plasma source consists of a quartz-bulb with a 254 holes facing the substrate heater [Fig. 4.6(b)]. The quartz bulb is surrounded with a coil to which an RF-power in the range 150–300 W is applied. The sample is exposed to the plasma by opening a shutter in front of the quartz aperture. Ultra pure 6N neutral O_2 was used as the source gas [Fig. 4.6(c)]. A plasma consisting of neutral, excited and charged elements of O and (O_2) was created inside the quartz bulb. Light is emitted from the plasma when the constituent elements decayed to the ground state. The emitted light was detected through the optical viewport located at the end of the plasma source [Fig. 4.6(d)]. The well-defined atomic transitions of the emitted light was used to identify the contents of the plasma. The total emitted spectral line intensity I is given by $I \sim AN$ where A is the atomic transition probability and N the number of excited atoms per unit volume [94]. A computer controlled fiber-coupled Avantes AvaSpec 3648 spectrometer with a 200–1100 nm wavelength range and with a resolution of 1.3 nm was used to record the emitted light from the plasma. Figure 4.6(f) shows an optical emission spectrum obtained from the O-plasma with the plasma operated at 150 W and with an O_2 flow-rate $\Phi_{\text{O}_2}=1.0 \text{ sccm}$. The highest peaks were intentionally saturated to make the weaker peaks more visible. The National Institute of Standards and Technology (NIST) Atomic Spectra Database for excited

neutral atomic O (OI) and excited and singly ionized atomic O (OII) was used for the spectral peak identification [95]. The peaks related to excited and singly ionized molecular O (O_2^+) were identified using the spectral data available in Ref. [96].

The insert in Figure 4.6(f) shows the total optical emission intensity as a function of a varying Φ_{O_2} where the intensity was integrated over the entire spectrometer wavelength range (200–1100 nm) for each Φ_{O_2} flow rate. An increase of intensity up to a maximum for $0.25 < \Phi_{O_2} < 2.0$ sccm was observed. This initial intensity increase was followed by an intensity reduction for higher Φ_{O_2} values.

Figure 4.6(g) shows an increased emission intensity for a selection of peak-lines with an RF-power between 150–300 and with $\Phi_{O_2} = 1.0$ sccm. These observations for the employed 254-hole quartz bulb are similar to previously reported observations using a 275-hole aperture with an RF power between 150–450 W with $\Phi_{O_2} = 1.5$ sccm [97]. Nevertheless, in Ref. [97] it was pointed out that a lower number of aperture holes will affect the response of the emission intensity.

4. CHARACTERIZATION TECHNIQUES

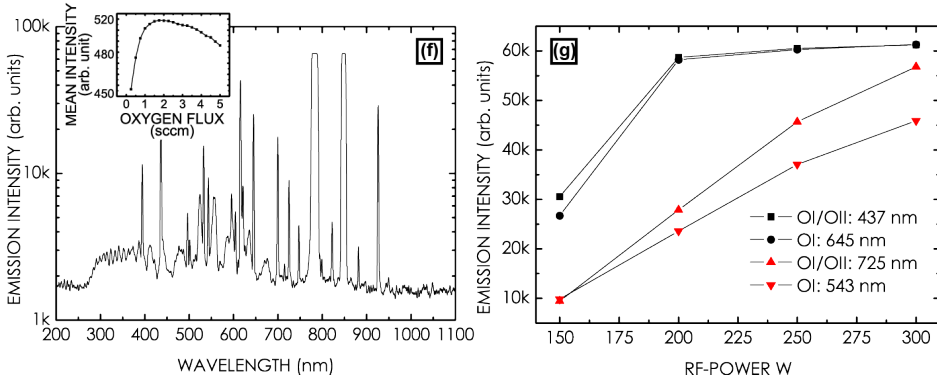
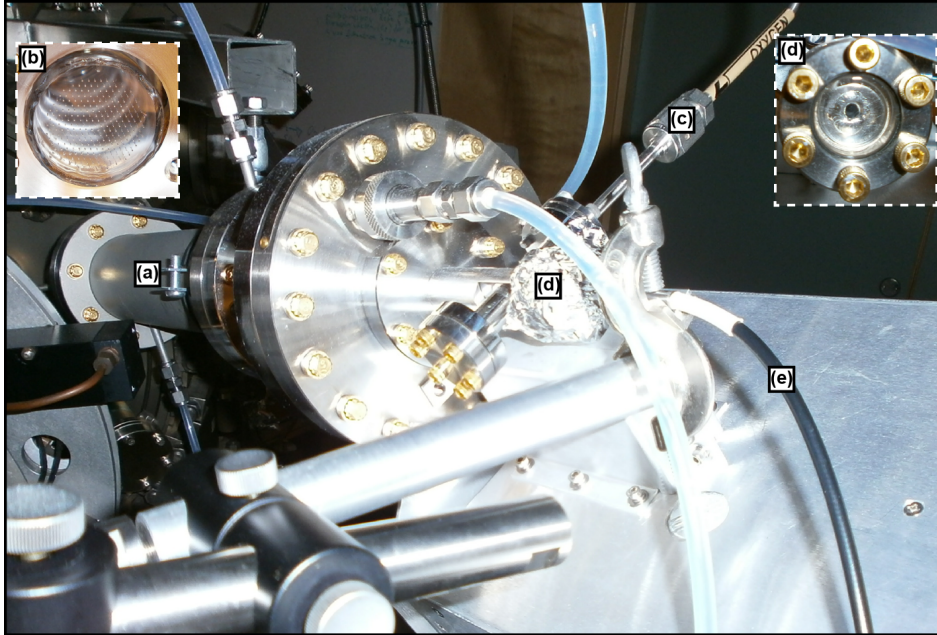


Figure 4.6: Optical emission spectroscopy setup. Oxygen plasma source (a) with a quartz bulb equipped with a 254-hole aperture (b) supplied with O_2 (c). Optical viewport (d) to which an optical fiber (e) is attached and connected to a spectrometer. The spectrometer is connected to a computer. Captured emission spectrum from the O-plasma (f) with the integrated average emission intensity for all wavelengths for O_2 flow rates $0.25 < \Phi_{O_2} < 5.0$ sccm (insert). Emission intensity of selected lines for RF-powers 150–300 W (g).

Chapter 5

Growth of ZnO and GaN

This chapter presents the growth and characterization of ZnO and GaN on 4H-SiC(0001) substrates and GaN(0001)/Al₂O₃-templates. A description of the substrate preparation is given and is followed by a section on how to grow GaN on 4H-SiC. Hereafter, a section on the nucleation is given related to paper 5.3. The nucleation section describes how to grow either ZnO(0001) or ZnO(000 $\bar{1}$) on GaN(0001).

The next section describe how to grow a smooth ZnO(0001)-layers on GaN/4H-SiC as reported in papers II-III. The described method has been employed also on GaN(0001)/Al₂O₃-templates for both ZnO(0001) and ZnO(000 $\bar{1}$). This section also include a description on how the growth rate of ZnO(0001) and ZnO(000 $\bar{1}$) on GaN(0001) depends on the active amount of O supplied by the O-plasma source (paper IV).

5.1 Substrates

In this work, two different types of substrates have been used, 3-inch 4H-SiC(0001) and 2-inch GaN(0001)/Al₂O₃-templates. The GaN(0001)/Al₂O₃-templates were acquired from SaintGobain Crystals [98]. Both standard non-intentionally doped and semi-insulating GaN(0001)/Al₂O₃-templates were employed. The thickness of the GaN template layer is 3.5–4.2 μ m on Al₂O₃. This GaN layer is completely relaxed on the Al₂O₃ substrate (lattice constants $a_{\text{Al}_2\text{O}_3} = 0.4765$ nm and $a_{\text{Al}_2\text{O}_3} = 1.2982$ nm) [99]. Figure 4.2 in chapter 4.2 shows an AFM micrograph of the surface of an as-received GaN template layer.

The 4H-SiC(0001)-substrates were acquired from Cree[50]. Polishing of the SiC substrates was performed by NovaSiC [100] and produced an atomically smooth surface exhibiting straight and wide terraces.

5.1.1 Substrate preparation

The substrates were cleaved into $(10-15) \times (10-15)$ mm² pieces and degreased using a standard organic cleaning procedure (acetone, isopropanol, de-ionized H₂O, sonication, N₂ blow-dry) before before they were In-mounted on the sample holder and introduced into the MBE system. All samples were outgassed at 500–600°C for 1–3 h in the growth chamber prior to the growth.

An in-situ Ga-polishing or Ga flash-off procedure was performed prior to the GaN growth to remove sub-oxides residing on the SiC substrate surface [101, 102]. This procedure also served as an independent temperature calibration of the specific substrate holder.

Table 5.1 summarizes the different substrate holder configurations, the substrate temperatures for the (3×1) reconstruction and typical GaN growth temperatures for the sample series presented in this work also given in papers I–V. All samples reported

Table 5.1: Summary of the different substrate holder configurations used in this work. Listed is the typical substrate temperature for the (3×1) reconstruction $T_S-(3 \times 1)$, the corresponding growth temperature for GaN, sample series with the corresponding references.

Sample holder	$T_S-(3 \times 1)$ (°C)	T_S -GaN (°C)	Samples (°C)	Paper
Mo-block	870–880	900	m1001-m1013	–
Si+2 μ m Ti	825–835	865	m1014-m1081	I
Si	650–670	650–700	m1082-m1264	II–V

in paper I were mounted on Si wafers coated with 2 μ m Ti on the back side. From sample m1082 and forward, all samples were mounted on Si-wafers without the Ti on the backside (papers II – V). The measured substrate temperature was $\approx 150 - 180^\circ\text{C}$ higher for a Si-wafer with a Ti-coated backside compared to a bare uncoated Si-wafer. Early experiments with solid Mo holders exhibited a $\approx 200^\circ\text{C}$ higher substrate temperature compared to an untreated Si-wafer. Knowledge of the type of substrate holder is therefore important for a reasonable comparison of growth results.

5.1.2 RHEED - ZnO on GaN

Figure 5.1 shows the temporal evolution of the RHEED-pattern from the $[11\bar{2}0]$ azimuth before, during, and after 20 min growth of ZnO on a GaN(0001)/Al₂O₃ template treated with N-plasma (exposure to N-plasma prior to the growth). A similar temporal evolution was observed for Zn- and Ga-treated GaN(0001)/Al₂O₃-templates [paper I].

Figure 5.1(a) shows bright small streaks and Kikuchi lines (the curved lines) as observed after (~ 1 h) thermal outgassing of the GaN(0001)/Al₂O₃ template. A brighter pattern is observed after the N-plasma surface treatment [Fig. 5.1(b)]. The longer streaks indicate an improved lattice ordering of the surface on the order of the electron coherence length which is ~ 100 nm corresponding to an acceleration voltage of 10 kV [73], [74].

Figure 5.1(c) shows a lower intensity of the RHEED pattern during the first minutes of ZnO growth with both Zn and O-shutters open. The reduced intensity is attributed to a larger disorder on the surface as compared with the N-plasma exposure case. For most samples, the RHEED patterns remained streaky for 3.5–4.5 minutes and hereafter larger and brighter spots were formed. During this period of time, a slow nucleation and island formation occurred as evidenced from AFM micrographs [paper I].

Large and bright RHEED spots are observed after 4 min, indicating coalescence of the islands which resulted in a rough surface morphology and which yielded transmission and diffraction of electrons through 3D features on the surface [Fig. 5.1(d)]. The RHEED pattern remained spotty or in some cases, weak streaks developed between the spots producing a modulated pattern. These weak streaks remained to the end of the growth [Figs. 5.1(f)-(g)]. An increased intensity was observed for the final modulated RHEED-pattern when the growth chamber was pumped down to base pressure [Fig. 5.1(h)].

The N-plasma treated sample exhibited an RMS roughness of 4 nm and PV distance of 35 nm as determined from AFM scans over $2 \times 2 \mu\text{m}^2$. In comparison, the Zn-treated sample exhibited a more streaky end-of-growth RHEED pattern with less pronounced modulated streaks indicating a smoother surface exhibiting an RMS roughness of 2 nm and a PV distance PV=22 nm. Without pre-treatment, the RHEED pattern changed from initial nucleation spots to diffuse streaks which was maintained for the rest of the growth indicating a comparably smooth layer. In this case, the AFM micrographs showed only nucleation islands without a subsequent layer growth [paper I].

5.2 GaN on 4H-SiC(0001)

The growth of GaN on the 4H-SiC and 6H-SiC polytypes with MBE has been described in refs [2, 61, 101–104] and adapted to the requirements of this work.

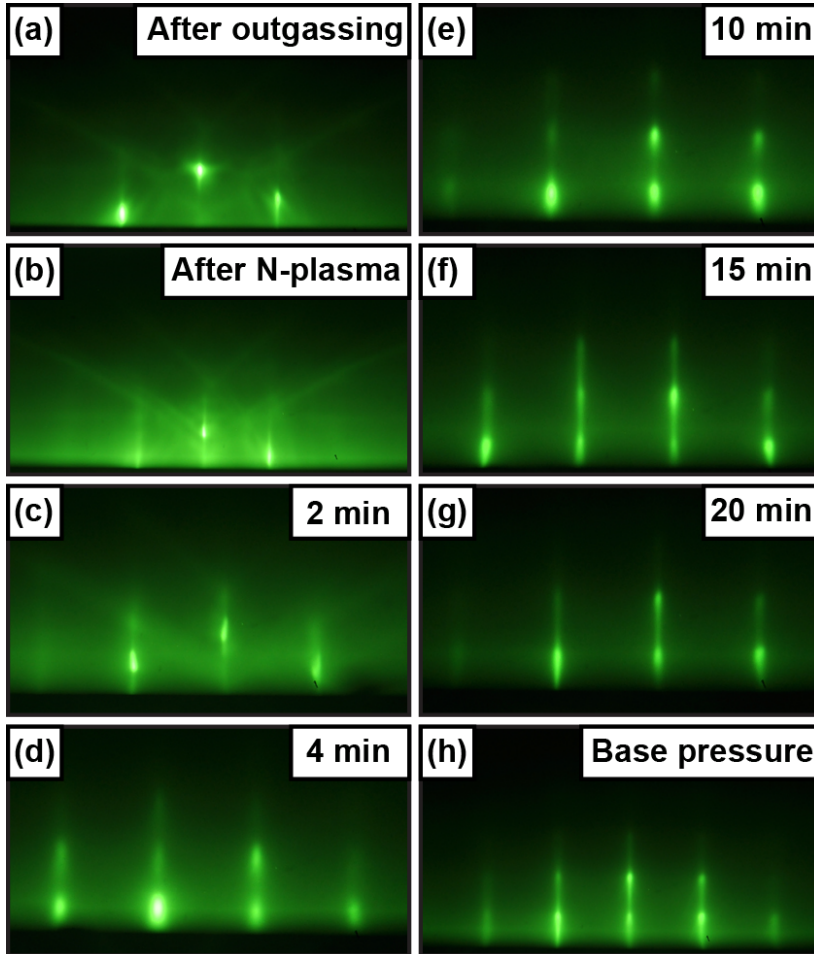


Figure 5.1: Temporal evolution of the RHEED-pattern from the $[11\bar{2}0]$ azimuth before, during and after ZnO growth on a GaN(0001)/Al₂O₃ template. After thermal outgassing (a). After N-plasma treatment (b). Growth after 2 min (c), 4 min (d), 10 min (e), 15 min (f) and 20 min (g). End of growth RHEED pattern with growth chamber pumped down to base pressure (h).

Figure 5.2(a) shows a common GaN MBE phase diagram that illustrates Ga-rich, Ga-stable and N-rich growth regimes. The corresponding RHEED-patterns and inten-

sities during growth are very dark streaks or no pattern at all for Ga-rich growth, bright and streaky for Ga-stable growth and very bright chevrons for the N-rich regime. The optical microscopy image insert in Fig. 5.2(a) shows 2–8 μm wide Ga-droplets on the surface of a GaN sample grown under Ga-rich conditions. It is possible to evaporate these Ga-droplets by increasing the growth temperature. Large droplets leave circular areas or footprints behind on the surface as revealed by optical microscopy.

A featureless GaN surface is observed in both dark field and bright field optical microscopy for GaN grown under Ga-stable conditions as shown in Fig. 5.2(b). For GaN grown under N-rich conditions, the bright field contrast image can be observed indicating plateau-valley morphology [Fig. 5.2(c)].

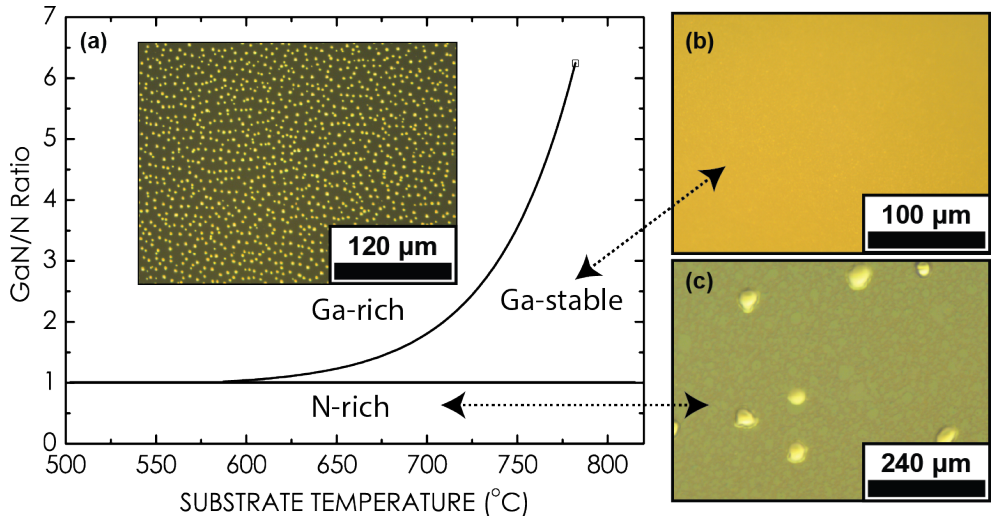


Figure 5.2: Phase diagram for MBE of GaN. Dark field optical microscopy image (insert) show Ga-droplets after Ga-rich growth (a). Optical microscopy image for GaN grown under Ga-stable (b) and N-rich conditions (c) which also shows a few Ga-droplets on the surface. These droplets resulted from a Ga-rich period during the growth.

Figure 5.3 shows structural and morphological data for a GaN-layers grown on 4H-SiC(0001) during Ga-stable conditions.

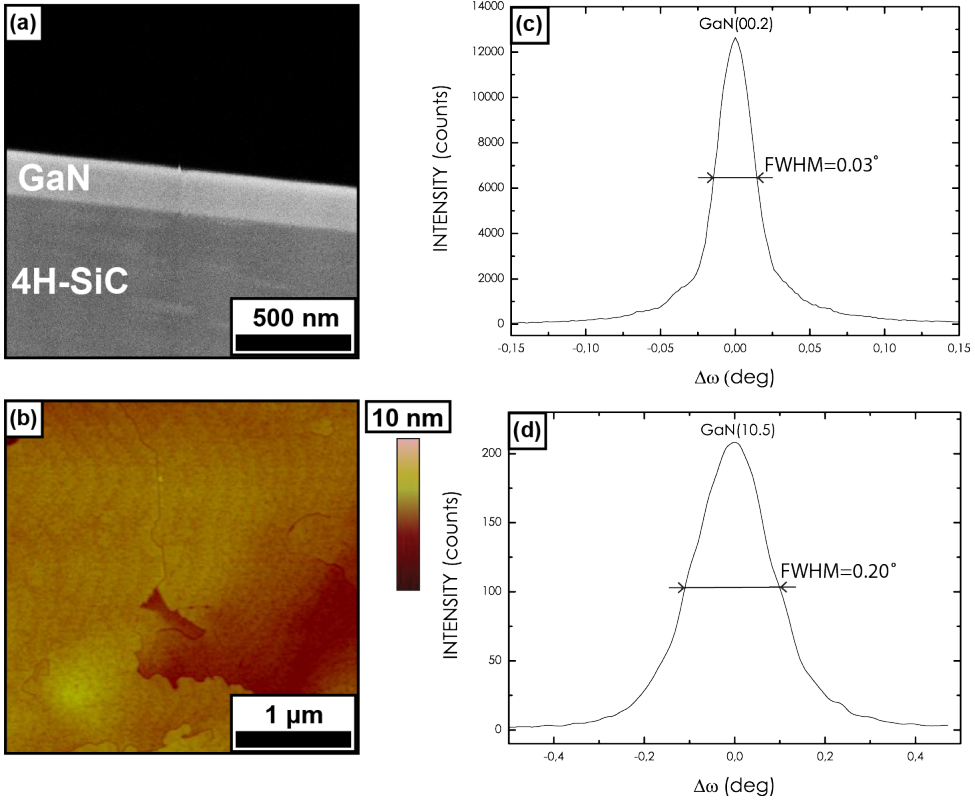


Figure 5.3: Morphological and structural data for a GaN(0001) layer grown on a 4H-SiC(0001) substrate. Cross-sectional SEM of a 190 nm thick layer (a). AFM micrographs of GaN surfaces (b). XRC across the GaN(0002) reflection (c). The XRC FWHM is 107 arcsec for this reflection. XRC across the GaN(10 $\bar{1}$ 5) reflection (d). The (10 $\bar{1}$ 5) XRC FWHM is 728 arcsec.

5.3 ZnO-nucleation and initial growth

This section describes ZnO nucleation on 4H-SiC, on GaN(0001)/Al₂O₃-templates and on in-situ grown GaN/4H-SiC buffer layers. In paper I we have reported on the difference in nucleation and subsequent growth on GaN(0001)/Al₂O₃ and on in-situ grown GaN/4H-SiC buffer layers.

5.3.1 ZnO nucleation on 4H-SiC(0001)

There are several experimental reports on the initial stages of the nucleation, the coalescence and the epitaxial growth of ZnO on 6H-SiC(0001), [105–109]. In these papers, the nucleation and coalescence is discussed. A more theoretical discussion involving the Zn-O bond process on the substrate surface, is provided by Fujiwara et al. [60]. A few papers have been published regarding the growth of ZnO on 4H-SiC(0001) with MBE [110, 111]. Smooth ZnO layers on 4H-SiC(0001) have been achieved using pairs of buffer layers grown at a low temperature followed by high-temperature annealing and subsequent growth. The reported AFM root mean square (RMS) was 0.75 nm for a scan over a $2 \times 2 \mu\text{m}^2$ area and the FWHM was 468 arcsec for an XRC across the ZnO(0002) reflection [111].

We tried direct deposition of ZnO on 4C-SiC(0001) and observed nucleation islands without layer formation. The ZnO growth parameters, including the Ga-polishing procedure prior to the growth, were similar to what is reported in paper I. The substrate temperature was 590 °C for a Si wafer carrier with a 2 μm Ti back side coating and the Zn beam equivalent pressure (BEP) was 1.0×10^{-5} Torr as measured before the growth. The O-plasma source was operated at 300 W with an O₂ flow rate Φ_{O_2} of 1.0 sccm.

Figure 5.4 shows small ZnO islands along the steps of the 4H-SiC(0001) substrate after 30 min of growth. It was not possible to map the surface with AFM without

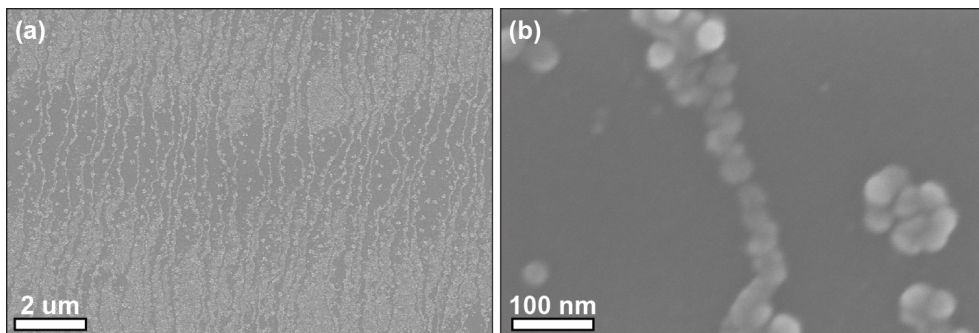


Figure 5.4: SEM micrograph of ZnO islands along 4H-SiC(0001) steps (sample m1060).

observing severe tip-imaging likely caused by the AFM tip picking up the islands from the substrate surface. A growth performed under identical conditions but with a growth time of 2 min, did not exhibit any surface features as revealed by AFM. The islands are arranged along the steps-edges or terraces of the 4H-SiC(0001) substrate (c.f. TSK-model in figure 3.2, chapter 3.1.3). The number of binding sites for a Zn and or an O atom at a step-edge are larger as compared with the number of binding

sites on a terrace. Due to energetic reasons, the atoms rather stick to edges than to flat surfaces with less available bonds. The XRC showed a weak broad ZnO signal to the left of the 4H-SiC(0001) substrate peak. The weak signal intensity and the broadening are attributed to the small size of the ZnO islands.

5.3.2 ZnO nucleation on GaN/Al₂O₃-templates

Nucleation of ZnO occurred on untreated GaN(0001)/Al₂O₃ but no layer formed. These results are very similar to what was observed for ZnO growth on Ga-treated 4H-SiC.

Figures 5.5(a) and (c) show the ZnO nucleation islands on an untreated GaN(0001)/Al₂O₃-template after 5 and 20 min of growth, respectively. After 20 min growth, the dispersed islands on the GaN-template were 15–30 nm wide and 0.5–0.7 nm high [Fig. 5.5(c)]. Here, the step-morphology of the GaN-template is still clearly visible on both samples and no coalescence of the islands into a layer had occurred. In contrast, for a Zn-, N-plasma or Ga- pre-treatment, the ZnO islands coalesced and formed a layer as reported in paper I.

Figures 5.5(b) and (d) show the ZnO nucleation islands on a Zn-treated GaN(0001)/Al₂O₃-template after 5 and 20 min of growth, respectively. After 5 min of growth, the surface of the GaN(0001)/Al₂O₃-template was still visible [Fig. 5.5(b)]. After 20 min of growth, the ZnO islands had coalesced into a columnar film on the Zn pre-exposed GaN surface and the GaN surface was not visible anymore. The columns were 100–200 nm wide and 3–15 nm high [Fig. 5.5(d)]. ZnO coalescence and film growth had clearly occurred after 20 min.

Elemental analysis of nucleation samples

In paper I, ZnO is identified with TOF-SIMS on nucleation layers that were grown for 2–20 min. Here, the elemental mapping of ZnO⁺ and Zn⁺ is shown for 10×10 μm² areas and for Zn- and Ga-treated GaN(0001)/Al₂O₃.

Figures 5.6(a)–(b) show detection of ZnO⁺ and Zn⁺ ions for a 20×20 μm area of a ZnO nucleation layer grown for 5 min on a Zn-treated GaN(0001)/Al₂O₃-template (sample m1064).

The scalebar represents the number of counts (cts) for each ion which in this case is a qualitative measurement. A quantitative assessment on the real number of ions requires a calibration sample. Nevertheless, the identification of each ion mass from the acquired mass spectra is unambiguous since isotopes or other elements could not be detected during the measurements.

Figure 5.6(c) shows sputter profiles of ZnO⁺ and Zn⁺ ions for a ZnO layer grown for 20 min on a Ga-treated GaN(0001)/Al₂O₃-template (sample m1059). Each curve is normalized to the corresponding maximum number of counts. The number of counts decreases with the sputter time which indicates that the ZnO is completely sputtered

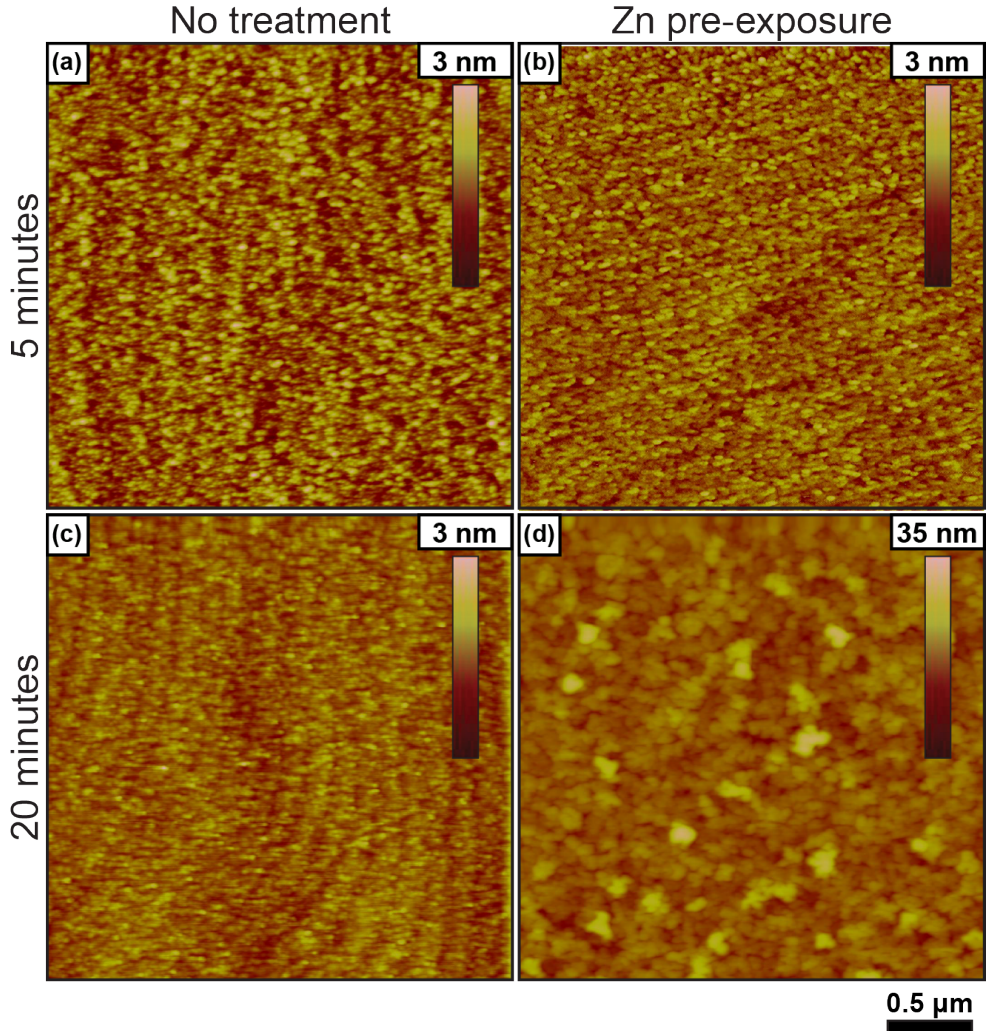


Figure 5.5: AFM micrographs of nucleation sample surfaces after 5 (a)–(b) and 20 min (c)–(d) of ZnO nucleation growth on untreated and on Zn pre-exposed GaN/Al₂O₃.

away. The increase of Ga⁺ is attributed to residual Ga droplets on the surface after the Ga polishing procedure or Ga from the GaN layer.

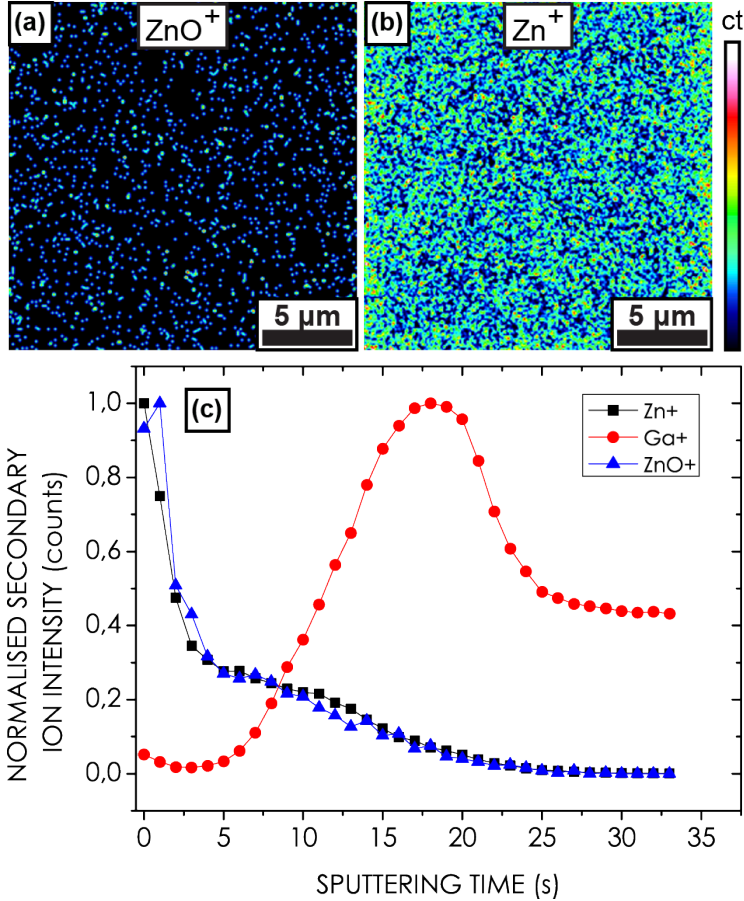


Figure 5.6: TOF-SIMS maps of ZnO^+ ions (a) and Zn^+ ions (b) for a ZnO layer grown for 5 min on a Zn-treated substrate (sample m1064). Normalized TOF-SIMS graphs for Zn^+ , ZnO^+ and Ga^+ ions plotted with respect to sputtering time for a ZnO-grown layer for 20 min on Ga-treated GaN(0001)/ Al_2O_3 (sample m1059) (c).

5.3.3 ZnO nucleation on GaN/4H-SiC

In paper I we reported on the need for Zn-, N-plasma or Ga-pre-treatment prior to the ZnO growth on GaN(0001)/ Al_2O_3 . It was concluded that it is crucial to use a procedure for removing the Ga_xO_y sub-oxides to achieve ZnO growth on GaN(0001)/ Al_2O_3 -templates. It was also reported that no such pre-treatment procedure is needed to

achieve ZnO growth on in-situ grown GaN since these GaN-layers were never exposed to ambient and thus never formed sub-oxides.

The same ZnO-growth conditions were used on in-situ grown GaN/4H-SiC buffer layers as for 4H-SiC(0001) and GaN(0001)/Al₂O₃-templates. Cross-sectional SEM micrographs revealed that a 115–175 nm thick columnar ZnO film had formed. The RMS roughness was 11 nm and PV distance 80 nm as determined from AFM scans over 2×2 μm². The XRC FWHM of the ZnO(0002) peak was 389 arcsec compared to the FWHM of the GaN(0002) peak which was 108 arcsec.

In summary, we observed nucleation islands on all substrates but a ZnO layer formation was only observed on pre-treated GaN(0001)/Al₂O₃-templates and on (untreated) in-situ grown GaN/4H-SiC-buffer layers. The ZnO layers exhibited a relatively rough morphology.

5.3.4 Zn(0001) and ZnO(000 $\bar{1}$) growth

The effect of pre-exposing GaN(0001)/Al₂O₃ layers to a Zn-flux or O-plasma before starting the ZnO growth has been investigated with respect to the resulting ZnO-polarity, the structural quality and the interface homogeneity by a number of research groups [16–21]. An important conclusion in these reports was that Zn pre-exposure always resulted in Zn(0001) and O-exposure always resulted ZnO(000 $\bar{1}$). It was also shown that no interface layer was formed between the ZnO(0001) layer and the GaN(0001)/Al₂O₃-template for the Zn pre-exposed samples. O-plasma exposure on the other hand, resulted in the formation of monoclinic Ga₂O₃ on the surface of the GaN(0001)/Al₂O₃-template. The ZnO(000 $\bar{1}$) grown on this surface exhibited a lower structural quality as compared to the ZnO(0001) layers that were grown on GaN(0001) that was pre-exposed to Zn. Polarity determination of the grown layer can be done with wet-etch experiments using hydrochloric acid (HCl) as described in Ref. [112].

In this work, both Zn(0001) and ZnO(000 $\bar{1}$) layers were grown on GaN(0001)/Al₂O₃-templates. The ZnO(0001) layer growth was initiated by a 3 s up to 3.5 min pre-deposition of Zn on the GaN/Al₂O₃(0001) before opening the shutter to the O-plasma source. The ZnO(000 $\bar{1}$) growth was initiated with a 5 min pre-exposure of the GaN/Al₂O₃-template to the O-plasma (RF-power at 300 W with an O₂ flow rate of 2.0 sccm) before opening the Zn-shutter (papers IV- V).

The ZnO was etched in 0.012 M HCl for 10 s and the surfaces were examined by SEM. Hexagonal etch pits [Fig. 5.7(a)] indicated Zn(0001) and rough hillocks [Fig. 5.7(b)] was an indication of ZnO(000 $\bar{1}$) [112].

5.4 Growth of smooth ZnO layers on GaN(0001)/4H-SiC

Since the roughness of the initial grown ZnO(0001) layers [paper I] was comparably high, a growth study of ZnO(0001) on in-situ grown GaN(0001)/4H-SiC was performed and is described in papers II–III.

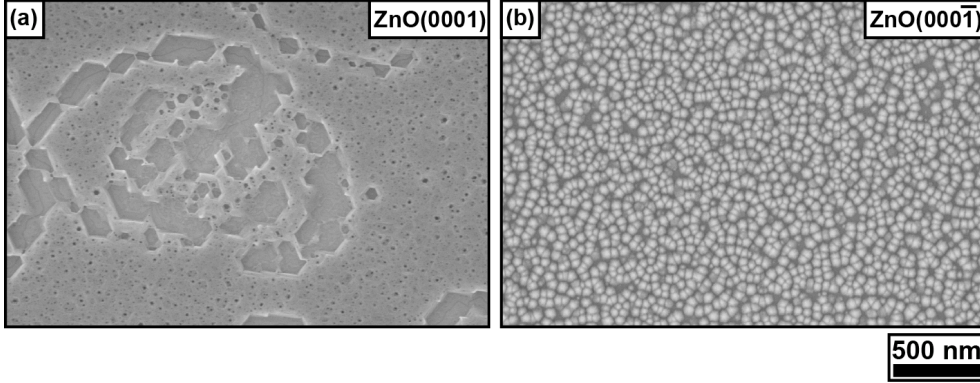


Figure 5.7: SEM micrographs of ZnO layers after a 10 s etch in a 0.012 M HCl solution. (a) ZnO(0001) and (b) ZnO(000 $\bar{1}$).

This section describes how to grow statistically smooth ZnO(0001) layers suitable for DBRs. These results are also applicable for the growth of both ZnO(0001) and ZnO(000 $\bar{1}$) on GaN(0001)/Al₂O₃ templates. In addition, a new growth rate dependence of ZnO on the O₂ flow rate Φ_{O_2} was observed and is described in detail in paper IV.

Early reports describe the influence of the Zn/O-ratio on the growth of ZnO on Al₂O₃ substrates with or without MgO or ZnO buffer layers [113–116]. Other reports treat ZnO growth on MOCVD-grown GaN(0001)/Al₂O₃ layers [16–21].

5.4.1 ZnO - growth temperature dependence

Figure 5.8 shows the growth rate of ZnO(0001) on GaN/4H-SiC layers for growth temperatures $290 < T_{\text{S}} < 500$ °C and for two different Zn-source temperatures, $T_{\text{Zn}} = 390$ °C and $T_{\text{Zn}} = 420$ °C (T_{Zn} is proportional to the Zn-flux). The O-plasma RF-power was 300 W and the O₂ flow rate was $\Phi_{\text{O}_2} = 2.0$ sccm.

The temporal evolution for RHEED pattern was recorded during all growths. A distinct spotty RHEED-pattern was observed for all samples and is a characteristic of a rough surface. The growth rate is decreasing with increasing growth temperature T_{S} . This is expected due to a higher desorption at a higher substrate temperature. Also, as expected for the employed O-rich growth conditions, the growth rate for the samples grown with the Zn-source at 420 °C is higher than the growth rate for samples grown with $T_{\text{Zn}} = 390$ °C. The SEM image inserts show the surface morphology of a sample that was grown at a low T_{S} and another sample grown at a high T_{S} . Both

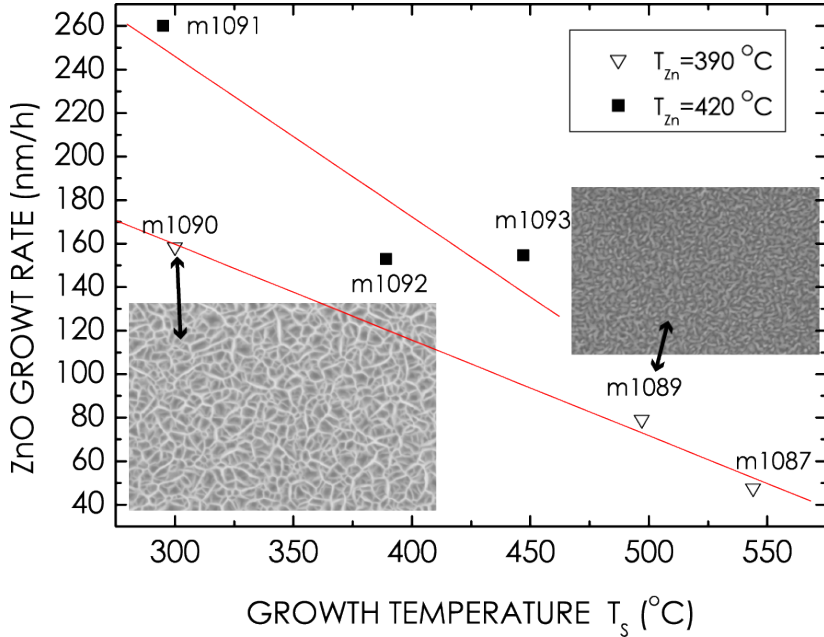


Figure 5.8: Growth rate of ZnO on GaN(0001)/4H-SiC buffer layers with respect to the growth temperature and at $T_{Zn} = 390^\circ\text{C}$ and $T_{Zn} = 420^\circ\text{C}$. The straight lines are guides to the eye. The inserts show SEM micrographs of the surfaces of two ZnO samples.

samples exhibit a network-like surface morphology and all other samples in the two sample series exhibited a similar rough morphology.

5.4.2 ZnO - Zn source temperature dependence

Figure 5.9 shows the growth rate of ZnO(0001) on GaN(0001)/4H-SiC for $340 < T_{Zn} < 420^\circ\text{C}$. The growth temperature varied inadvertently between $440\text{--}450^\circ\text{C}$ due to the limitations of the substrate heater control loop. The O-plasma RF-power was 300 W and the O_2 flow-rate $\Phi_{\text{O}_2} = 2.0$ sccm. A longer growth time was used to compensate for the lower growth rates resulting from using a lower T_{Zn} . A spotty RHEED pattern was observed for the sample grown (m1093) with the highest T_{Zn} . The SEM image inserts show a sparse network-like morphology which is indicative for columnar growth. The RHEED-pattern for the sample (m1093) grown with $T_{Zn} = 380^\circ\text{C}$ evolved slightly differently. Here, low-intensity lines started to form between the spots as well as

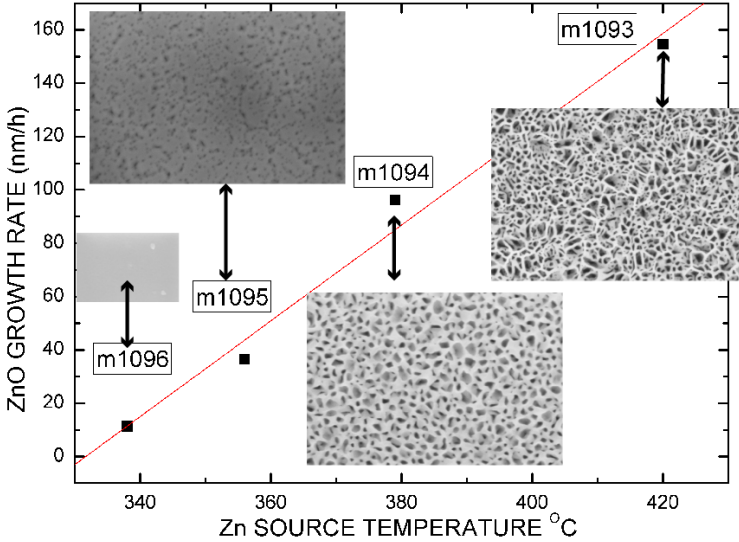


Figure 5.9: Growth rate of ZnO on GaN(0001)/4H-SiC for different Zn-source temperatures. The surface morphology is shown in the SEM image inserts. The O-plasma RF-power was 300 W and the O₂ flow-rate was 2.0 sccm. The line serves as a guide for the eye. The growth times were 1 h (m1093), 1.5 h (m1094), 2 h 10 min (m1095) and 3 h (m1096). The growth temperature was 440–450°C.

chevrons at each spot. Chevrons are the result of facets forming on the surface. The low-intensity lines between the spots are an indication of an improved lattice ordering within the coherence length of the electrons diffracted from the surface. The lateral coherence length is estimated to ≈ 150 nm for our 9.5 keV electron gun. The RHEED pattern for m1095 and m1096 grown with a low T_{Zn} evolved from streaky to spotty and then into modulated streaks. The modulated streaks were relatively bright and is yet an indication of a smooth surface. This is confirmed by the SEM images in Fig. 5.9 that show smooth surface morphologies.

5.4.3 ZnO - O₂ flow-rate dependence

Figure 5.10 shows the growth rate of ZnO(0001) on GaN(0001)/4H-SiC with respect to the O₂ flow-rate for three sample series G1–G3. Each sample group was grown at a different T_S

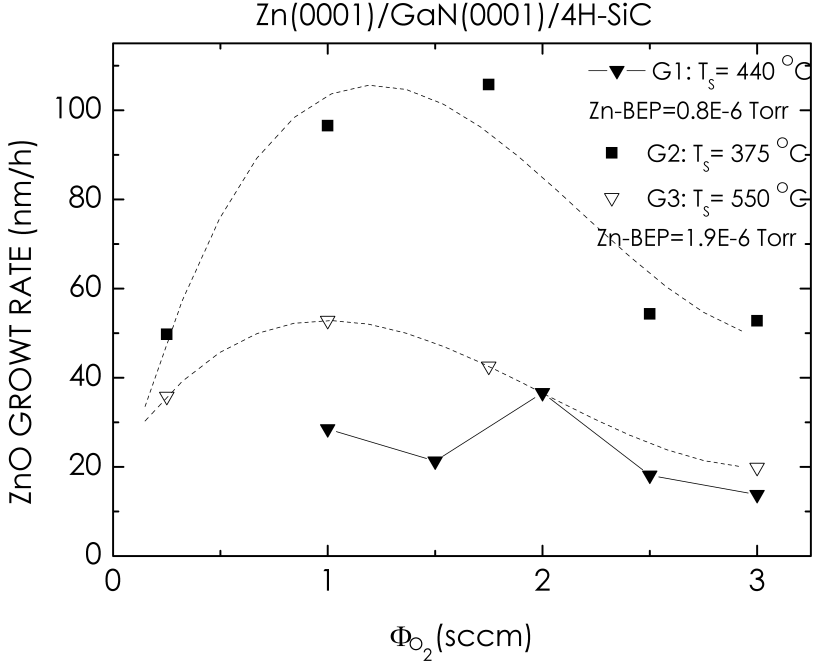


Figure 5.10: Growth rate of ZnO(0001) on GaN(0001)/4H-SiC for different O_2 flow-rates and for three series of samples grown at a different growth temperature.

For the G1-samples (\blacktriangledown), T_S was 440–445°C, $T_{Zn} = 350^\circ\text{C}$ corresponding to a Zn beam equivalent pressure (BEP) of 0.8×10^{-6} Torr and with $1.0 < \Phi_{O_2} < 3.0$ sccm. All BEP values are given with the BEP-controller range 200 μA for the filament current. The Zn-BEP of 0.36×10^{-6} Torr [paperIII] corresponds to the BEP controller range 2 mA-range and represent the same Zn-flux. The growth rate is relatively low and a decreasing trend can be observed for a higher Φ_{O_2} . The higher growth rate for the sample grown with $\Phi_{O_2} = 2.0$ sccm is probably caused by a higher Zn-flux during the growth than what was measured before the growth. All G1 samples exhibited a smooth and featureless surface morphology suitable for DBRs as observed with SEM. However, it was not expected to observe the decrease of the ZnO growth rate during O-rich conditions and this was therefore investigated further.

The G2 (\blacksquare) and G3 (∇) samples were grown with a higher Zn BEP of 1.9×10^{-6} Torr using $0.25 < \Phi_{O_2} < 3.0$ sccm and using $T_S = 375^\circ\text{C}$ for the G2 group and $T_S = 550^\circ\text{C}$ for the G3 samples. The higher growth rate for the G2- and G3- compared with the G1-samples is attributed to the higher Zn-flux. The higher growth rate for the G2-

5. GROWTH OF ZNO AND GAN

samples as compared to the G3-samples is attributed to the lower Zn desorption rate at lower substrate temperatures. The increase of the growth rate when Φ_{O_2} was increased above the flow rate of 0.25 sccm is expected since it is consistent with O-limited growth conditions. Both G1 and G2 series exhibit a maximum growth rate for $1.0 < \Phi_{\text{O}_2} < 2.0$ sccm. The growth rate was expected to be independent of Φ_{O_2} for O-rich conditions within a reasonable range of high Φ_{O_2} because the growth rate would be solely determined by the Zn-flux under these conditions corresponding to Zn-limited growth.

Figure 5.11 shows the growth rate of Zn(0001) and ZnO(000 $\bar{1}$) on GaN(0001)/Al₂O₃-templates at $T_s = 375^\circ\text{C}$ using $0.25 < \Phi_{\text{O}_2} < 4.5$ sccm with a Zn BEP of 1.7×10^{-6} Torr.

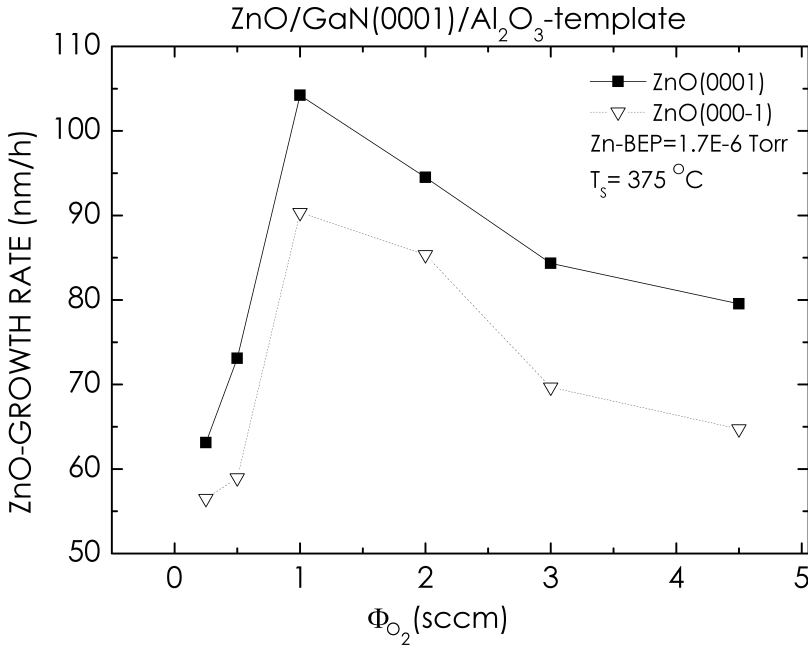


Figure 5.11: Growth rates of Zn(0001) and ZnO(000 $\bar{1}$) on GaN(0001)/Al₂O₃-templates for different O₂ flow-rates.

The growth rate for both Zn(0001) and ZnO(000 $\bar{1}$) exhibit the same unexpected growth rate dependence with respect to the O₂ flow rate as for the in-situ grown GaN(0001)/4H-SiC buffer layers. The growth rate of ZnO(0001) is higher than the ZnO(000 $\bar{1}$) growth rate and this is attributed to a higher number of back bonds (3) for a Zn-atom on an O-terminated ZnO(0001) surface compared to only (1) back bond for a Zn atom on an O-terminated ZnO(000 $\bar{1}$) surface. This difference in bond

configuration facilitates a higher incorporation rate of Zn-atoms in the ZnO(0001) direction [117, 118].

Earlier reports show how the Zn-flux during a constant O₂ flow-rate influences the ZnO growth rate [113–115, 117, 119, 120]. The growth rate initially increases due to Zn-limited (O-rich) conditions until it reaches a maximum. Hereafter, the growth rate remains constant due to Zn-rich (O-limited) conditions. The ZnO growth rate has been shown to increase during Zn-rich (O-limited) conditions when the O₂ flow rate was increased from $\Phi_{\text{O}_2} = 1.5$ sccm to $\Phi_{\text{O}_2} = 2.5$ sccm [119]. In this report, the same growth rate was observed during O-rich (Zn-limited) conditions for both $\Phi_{\text{O}_2} = 1.5$ sccm and 2.5 sccm. All reports show how the growth conditions change from O-rich (Zn/O-ratio < 1) through stoichiometric (Zn/O-ratio = 1) to Zn-rich (Zn/O-ratio > 1) where no further increase of the growth rate occurs. It was therefore unexpected to observe results that showed that the growth rate decreased when Φ_{O_2} was increased.

A very likely cause for this reduced ZnO growth rate for a higher Φ_{O_2} is a reduction of the O-plasma source efficiency due to a decrease of active O contributing to the ZnO growth. The optical emission from the O-plasma source was therefore investigated. The setup for the optical emission spectroscopy is described earlier in section 4.8.

Figure 5.12(a) shows the emission intensity for a selection of emission peak-lines using $0.25 < \Phi_{\text{O}_2} < 5.0$ sccm with an O-plasma source power of 300 W which was the same as for the ZnO growths.

The emission peak-line intensities for excited neutral atomic O (OI) and excited and singly ionized atomic O (OII) and unresolved combinations of OI and OII-lines show an increased intensity for an O₂ flow-rate that was increased up to 1–2 sccm. For $\Phi_{\text{O}_2} > 2.0$ sccm, the line intensity decreased.

In contrast, the emission line intensity for excited singly ionized molecular O (O₂⁺) showed an intensity decrease from a low $\Phi_{\text{O}_2} = 0.25$ to a high $\Phi_{\text{O}_2} = 5.0$ sccm [Fig. 5.12(b)].

The ZnO growth rate showed the same dependence on the O₂ flow-rate as the intensity for the emission spectra [Fig. 5.12(a)] and from this we concluded that the decrease of the growth rate was caused by a reduced amount of active OI and OII that could contribute to the ZnO growth. The singly ionized molecular O (O₂⁺) contribution to the ZnO growth was negligible.

In summary, the ZnO growth rate has been shown to depend on the amount of the active O (OI and OII) in contrast to earlier reports where it was related to the O₂ flow rate. These observations has been confirmed for ZnO(0001) on in-situ grown GaN(0001)/4H-SiC and for Zn(0001) and ZnO(0001) grown on GaN(0001)/Al₂O₃-templates and is reported in paper IV.

5.4.4 ZnO - smooth layers

The left column in Fig. 5.13 shows AFM micrographs over $2 \times 2 \mu\text{m}^2$ for samples grown with $1.0 < \Phi_{\text{O}_2} < 3.0$ sccm [G1-samples in Fig. 5.10]. Every height image is arranged

5. GROWTH OF ZNO AND GAN

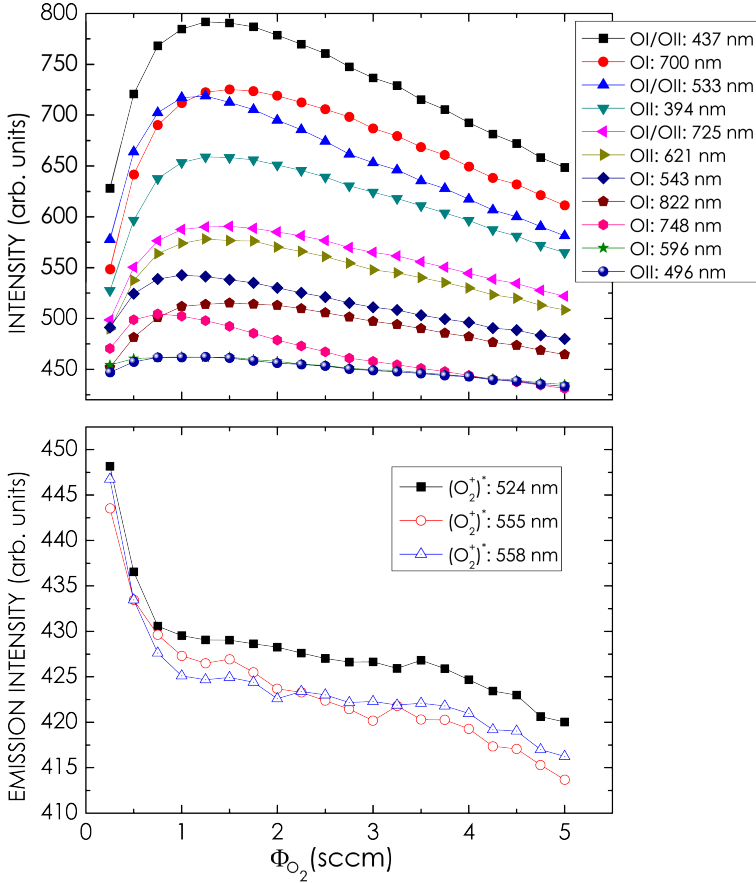


Figure 5.12: Emission line intensities for different O_2 flow rates. (a) Excited neutral atomic O (OI) or excited singly ionized atomic O (OII) and unresolved combinations of OI/OII-lines. (b) Excited singly ionized molecular O (O_2^+).

from the top row with $\Phi_{O_2} = 1.0$ sccm to the bottom row with $\Phi_{O_2} = 3.0$ sccm in steps of 0.5 sccm. The right column shows $1 \mu\text{m}$ long height-profile sections which are indicated with white lines in the the AFM micrographs. All samples exhibit the same type of morphology.

Figure 5.14 shows the evolution of the AFM RMS and peak to valley (PV) roughness for the ZnO samples grown with $1.0 < \Phi_{O_2} < 3.0$ sccm.

We see that a higher O_2 flow-rate leads to a lower RMS roughness and PV distance

thus indicating a smoother surface morphology. Sample m1099 has the smoothest surface morphology with an RMS-roughness of ≈ 0.5 nm which is comparable to the height of the ZnO unit cell. The surface exhibits nanoscale roughness as evidenced by the height cross-section profiles given in figure 5.13. The sample surface is statistically very smooth but does not exhibit ordering such as the step-flow morphology observed on MOCVD-grown GaN(0001) or a 4H-SiC substrate.

The RMS for the template was 0.06 nm and the PV was 0.9 nm over a $2 \times 2 \mu\text{m}^2$ scan area. An RMS surface roughness of 0.75 nm over a $2 \times 2 \mu\text{m}^2$ scan area from a ZnO layer grown with MBE on a low-temperature ZnO buffer layer deposited at a low temperature on a 4H-SiC(0001) substrate, has been reported in Ref. [111]. An RMS roughness of 1.6 nm has been reported for a MBE-grown ZnO layer on a MgO-buffer layer deposited on an Al_2O_3 substrate ($5 \times 5 \mu\text{m}^2$ scan area). This surface morphology was ordered since 80 nm wide terraces could be observed [113]. Therefore, our RMS-roughness compare well with corresponding values reported in the literature (c.f. Table-2 in paper III for more references).

5. GROWTH OF ZNO AND GAN

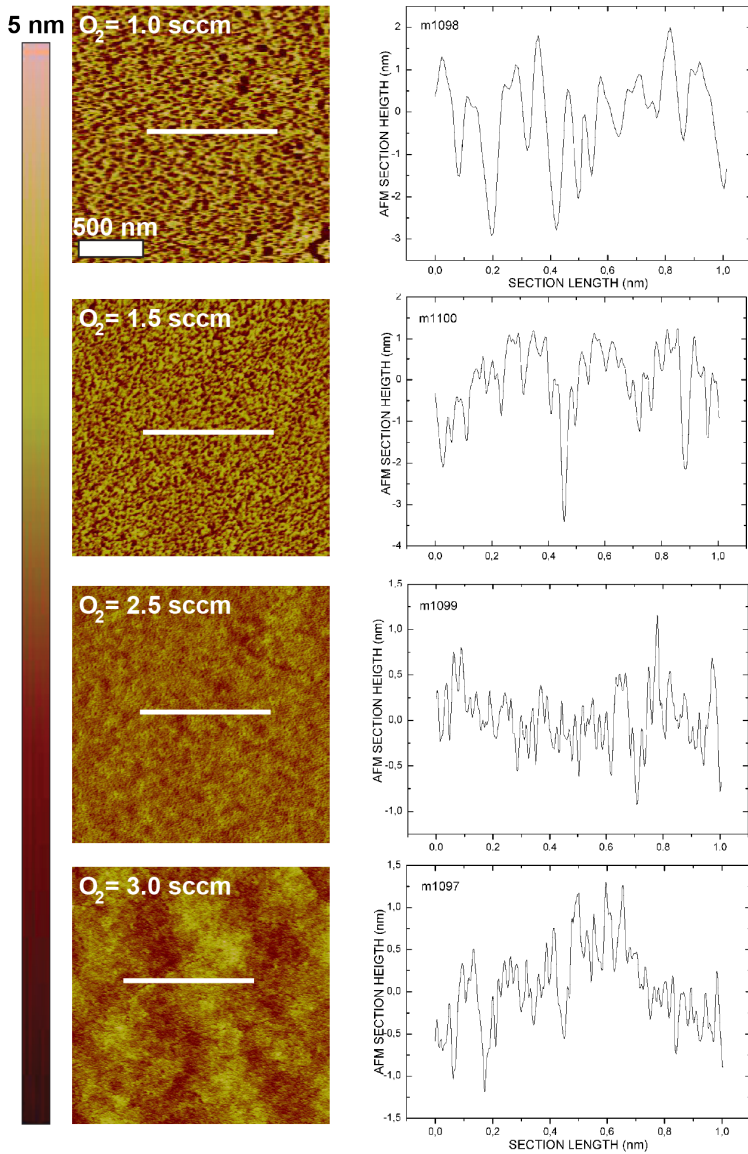


Figure 5.13: AFM micrographs of ZnO surfaces for an O_2 -flow rate of 1.0 sccm (m1098), 1.5 sccm (m1100), 2.5 sccm (m1099) and 3.0 sccm (m1097) (Left column). Height-profiles sections are indicated with white lines and are shown in the right column.

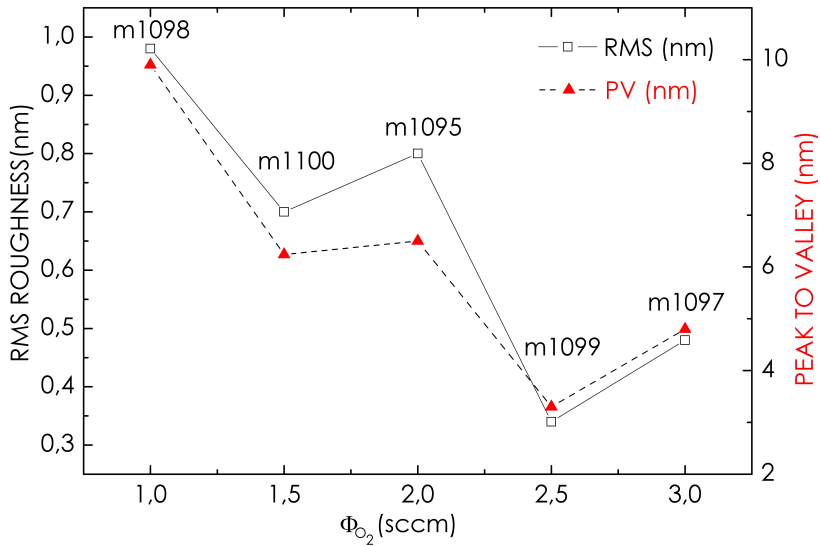


Figure 5.14: The evolution of the AFM RMS and PV values of ZnO samples grown on GaN(0001)/4H-SiC with respect to the O_2 flow rate. All measurements were taken over a $2 \times 2 \mu m^2$ area. The Zn-source temperature was $350^\circ C$. The substrate temperature was $440-445^\circ C$. The O -plasma power was 300 W. The growth times were 2 h 27 min (m1097), 2 h (m1098), 2 h 47 min (m1099) and 2 h (m1100).

Chapter 6

ZnO/GaN distributed Bragg reflectors

Previous sections described how to grow smooth GaN, ZnO(0001) and ZnO(000 $\bar{1}$) layers with optimized conditions [reported in papers I – IV]. This chapter describes the growth of ZnO/GaN DBRs along both ZnO(0001) and ZnO(000 $\bar{1}$) crystallographic directions which is reported in paper V.

6.1 Growth procedure - ZnO/GaN DBRs

Figure 6.1 shows a schematic corresponding to the first grown period for the ZnO/GaN DBR sample series S1 and S2.

The samples in S1 were grown along the ZnO(000 $\bar{1}$) direction [Figs 6.1(a) and (b)] while the S2 DBRs were grown along the opposite ZnO(0001) direction [Fig 6.1(c)]. The growth temperature T_S is indicated in Fig 6.1 for each layer. The respective number of periods grown for the S1 and S2 DBRs, were 2–20 and 1–5.5. All DBRs were initiated with the growth of a ZnO layer and ended with a GaN layer. The S1 DBRs started with a 5 min O-plasma pre-exposure using $\Phi_{O_2} = 2.0$ sccm on the GaN/Al₂O₃(0001) templates before opening the Zn-shutter which initiated the ZnO(000 $\bar{1}$) growth. The first type of S1 DBRs were grown at the same T_S for both the ZnO and the GaN layers [Figs 6.1(a)]. The second type of S1 DBRs were grown with a 3–9 nm thick low-temperature (LT) GaN buffer layer at $T_S = 350^\circ\text{C}$ followed by a high-temperature (HT) GaN layer grown at $T_S = 650^\circ\text{C}$ corresponding to one pair of ZnO/GaN [Figs 6.1(b)].

Figure 6.1(c) shows the growth procedure for the S2 DBR samples grown with a LT and a HT step for both the ZnO and the GaN layers. One ZnO/GaN period of the S2

6. ZNO/GAN DISTRIBUTED BRAGG REFLECTORS

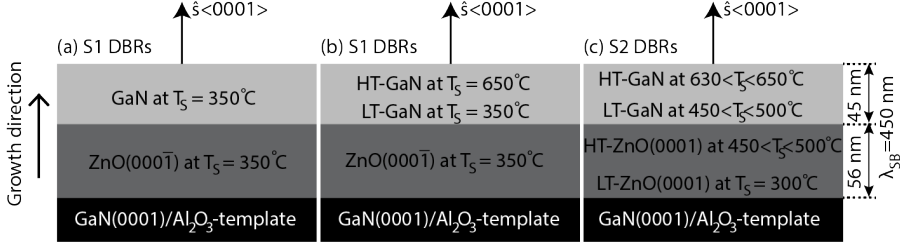


Figure 6.1: Schematic of the first period of the DBRs. (a) S1 DBRs grown along the ZnO(000 $\bar{1}$) direction using the same substrate temperature for both ZnO and GaN. (b) S1 DBRs grown along ZnO(000 $\bar{1}$) direction with a low- and high-temperature GaN layer. (c) S2 DBRs grown along the ZnO(0001) direction with a low- and high-temperature step for both ZnO and GaN. The growth direction which is parallel to surface normal \hat{s} , is indicated in the figure. Also indicated is the target center wavelength λ_{SB} for the stopband with corresponding $\lambda/4$ -layer thicknesses.

samples therefore corresponded to (LT-ZnO/HT-ZnO)/(LT-GaN/HT-GaN). The LT-ZnO(0001) growth was started with a 3 s pre-deposition of Zn on the GaN/Al₂O₃(0001) templates at $T_S = 300^\circ\text{C}$ before opening the shutter to the O-plasma which initiated the growth. After the completion of the LT-ZnO layer, the T_S was increased under O-plasma exposure of the sample to the growth temperature for HT-ZnO. A LT-GaN layers was initiated within 2–3 min after first switching off the O-plasma and then by simultaneously opening the shutters to the N-plasma source and the Ga-source. The LT-GaN layers were 3–9 nm thick and were exposed to the N-plasma source during the temperature ramp up to the HT-GaN growth temperature.

Studies on the growth of GaN on both ZnO(000 $\bar{1}$) and ZnO(0001) show that these GaN layers were (0001)-oriented (Ga-polar). Xia et al. reported in 2014 that MBE-growth of GaN on ZnO(000 $\bar{1}$) substrates at low growth temperatures $T_S < 550^\circ\text{C}$ using Ga-rich conditions, resulted in GaN(0001)-layers whereas N-rich conditions and $T_S > 600^\circ\text{C}$ yielded Ga(000 $\bar{1}$)-layers [121]. In 2004, Gu et al. used MBE to grow Ga(0001) on both ZnO(000 $\bar{1}$) and ZnO(0001) substrates using a LT-GaN buffer layer followed by HT-GaN growth and using Ga-rich conditions [122]. Kobayashi reported in 2006 on PLD deposition of GaN(0001) layers on ZnO(000 $\bar{1}$) substrates at room temperature or by using a LT-GaN layer grown at room temperature followed by a HT-GaN layer grown at $T_S = 700^\circ\text{C}$ [123]. Namkoong et al. reported in 2005 that single polarity Ga(0001) films were grown with MBE on ZnO(0001) substrates but that mixed polarity films with both GaN(0001) and GaN(000 $\bar{1}$) was the result on ZnO(000 $\bar{1}$) substrates. These mixed polarity layers were dominated by GaN(0001) [124].

Based on these studies, we concluded that the GaN layers grown using the S1

DBR growth scheme, most likely were Ga-polar [Fig 6.1(a) and b)] since a low growth temperature and Ga-stable conditions were used for the growth of these structures. However, it can not be excluded that these GaN layers had mixed GaN-polarity due to previous reports. Further, we concluded that the growth of GaN on the ZnO(0001) surface [Fig 6.1(c)] as in the case of the S2 DBRs, produced Ga-polar GaN layers.

6.2 List of selected sample properties - ZnO/GaN DBRs

Table 6.1 shows a selection of properties for the DBRs grown in this work. The S1 and S2 growth approach has been indicated in the sample name.

Table 6.1: Summary of selected properties for S1 and S2 ZnO/GaN DBRs. Listed is the number of periods N , the peak reflectance R , the stopband center wavelength λ_{SB} , the RMS roughness and the PV distance as determined from AFM scans over $2 \times 2 \mu\text{m}^2$. The type of surface morphology and the presence of Ga-droplets is also indicated.

Sample	N	R (%)	λ_{SB} (nm)	RMS (nm)	PV (nm)	Morphology	Ga- droplets
S1-43	2	47	443	6.5	43	rough	no Ga
S1-46	7	63	455	10.6	81.7	rough	no Ga
S1-55	20	77	501	12.5	104	rough	no Ga
S1-62	5	63	370	–	–	rough	no Ga
S1-64	5	63	427	15.3	110	rough	no Ga
S2-44	1	45-55	410	–	–	smooth	no Ga
S2-47	2	47/50	420/775	–	–	plateau valley	Ga
S2-51	1	52	396	1.7	16.3	plateau valley	no Ga
S2-60	1	48	385	–	–	smooth	no Ga
S2-45	2	60	382	–	–	plateau valley	no Ga
S2-63	1	39	440	–	–	smooth	Ga
S2-63	2	56-70	390	–	–	smooth	Ga
S2-07	5.5	23/40	449/564	2.1	20.6	smooth	Ga
S2-48	5	49/49	457/609	1.4	12.9	smooth	Ga

The number of periods N is listed together with the peak reflectance R , the stopband center wavelength λ_{SB} , the root-mean-square (RMS) roughness and the peak-to-valley (PV) distance as determined from AFM scans over $2 \times 2 \mu\text{m}^2$ and the type of surface morphology and the presence of Ga-droplets. Samples S1-43, S1-46 and S1-55

were grown with the same T_S whereas the samples S1-62 and S2-64 were grown with LT- and HT-GaN layers according to Fig. 6.1(a)-(b).

6.3 Properties of ZnO/GaN DBRs - Color

Figure 6.2(a) shows a photograph of a cleaved 20-period ZnO/GaN S1 DBR (sample S1-55). In Fig. 6.2(b) a 5.5-period ZnO/GaN S2 DBR where the top-layer is a LT-GaN-layer (sample S2-07), is shown. The cleavage edge c' - c'' and surface normal \hat{s} is indicated in the figure. To the naked eye, the 20-period ZnO/GaN DBR appeared blue across the entire sample area. The 5.5 ZnO/GaN DBR exhibited a green color. To exclude edge effects, the samples were cleaved close to their center area.

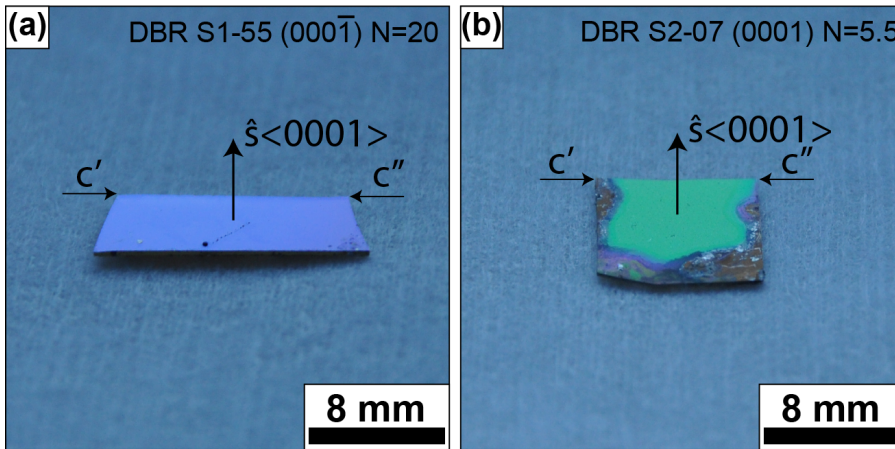


Figure 6.2: Photograph of an S1 (a) and an S2 (b) DBR after cleavage along the c' - c'' edge. The growth directions ZnO(000 $\bar{1}$) and ZnO(0001) and the number of periods (N) as well as the surface normals \hat{s} are indicated.

Figures 6.3(a)-(d) show the respective optical microscope image obtained from a 2-, 7-, 20- and 5-period S1 ZnO/GaN DBR [Table 6.1].

Each surface was free of cracks. The In on the back side of the sample originating from the sample mounting, is partially visible as white areas in Figs. 6.3(a)-(b). The small dark spots observed on the 5-period ZnO/GaN DBR (sample S1-62) are regions where the layers have delaminated from the substrate. This is attributed to a too thin LT-GaN layer that might not have been coalesced properly, a too fast temperature ramp that momentarily created large thermal stresses between the layers or a too high growth temperature for the HT-GaN causing decomposition of the layer.

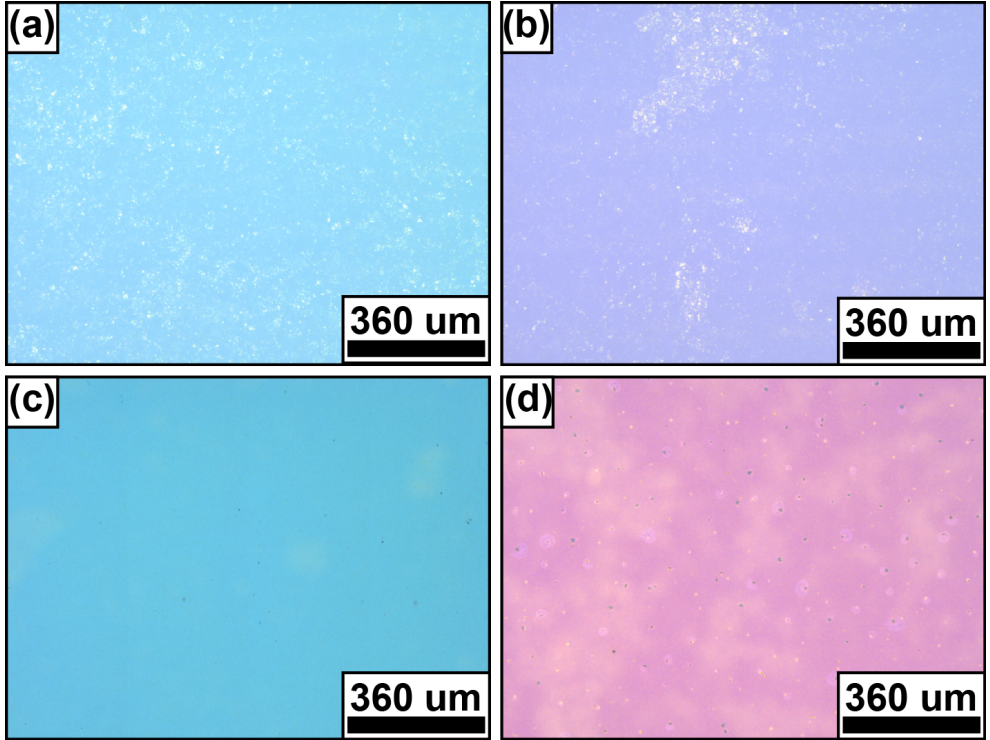


Figure 6.3: Optical microscopy images for S1 ZnO/GaN DBRs grown along the ZnO(000 $\bar{1}$)-direction for (a) 2 (sample S1-43), (b) 7 (sample S1-46), (c) 20 (sample S1-55) and (d) 5 periods (sample S1-62).

Figures 6.4(a–d) show optical microscopy images for a 1–2-period S2 ZnO/GaN DBRs listed in Table 6.1.

Figure 6.4(a) shows the optical microscope image of the surface of a 2-period ZnO/GaN S2 DBR (sample S2-45). This sample was grown under N-rich conditions which is known for creating the observed plateau-valley surface morphology. The insert shows that the sample is highly non-uniform also on a small scale.

Figure 6.4(b) shows a comparably more uniform sample (sample S2-51) which was grown with a higher amount of Ga but still under N-rich condition resulting in the observed plateau-valley surface morphology.

Figure 6.4(c) shows a single-pair uniform and smooth ZnO/GaN S2 DBR (sample S2-63N1) with a high density of Ga-droplets caused by Ga-rich growth conditions.

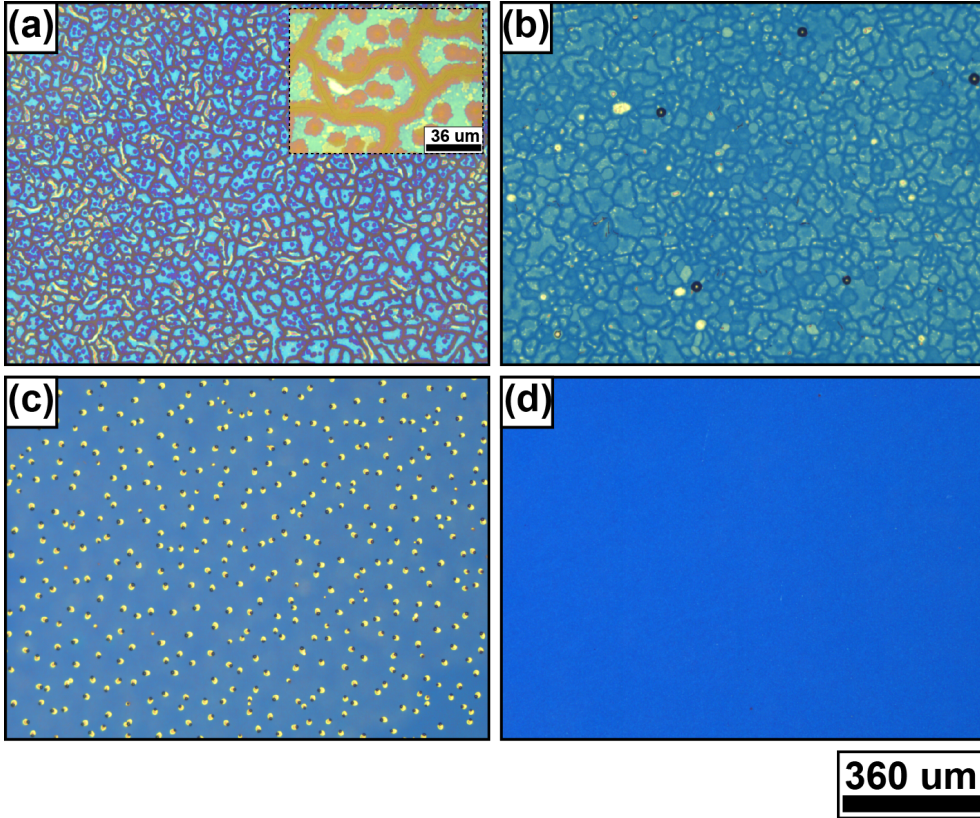


Figure 6.4: Optical microscopy images for S2 ZnO/GaN DBRs grown along the ZnO(0001)-direction. (a) Sample with plateau-valley morphology (sample S2-45). The insert shows foot-prints from droplets. (b) Sample with plateau-valley morphology and with Ga-droplets (sample S2-51). (c) Smooth sample with a high density of Ga-droplets (sample S2-63N1). (d) Featureless DBR sample with no Ga-droplets (sample S2-60).

A uniform and featureless sample (sample S2-60) free of Ga-droplets is shown in Fig. 6.4(d). This sample was grown under Ga-stable conditions where the amount of Ga on the growth front is balanced by the desorption and incorporation of Ga.

6.4 ZnO/GaN DBR surface morphology

Figures 6.5 show SEM micrographs for a 1-, 2- and 5-period ZnO/GaN S1 DBR [left column, (a)–(c)] and the corresponding S2 DBR [right column, (d)–(f)] for samples from Table 6.1.

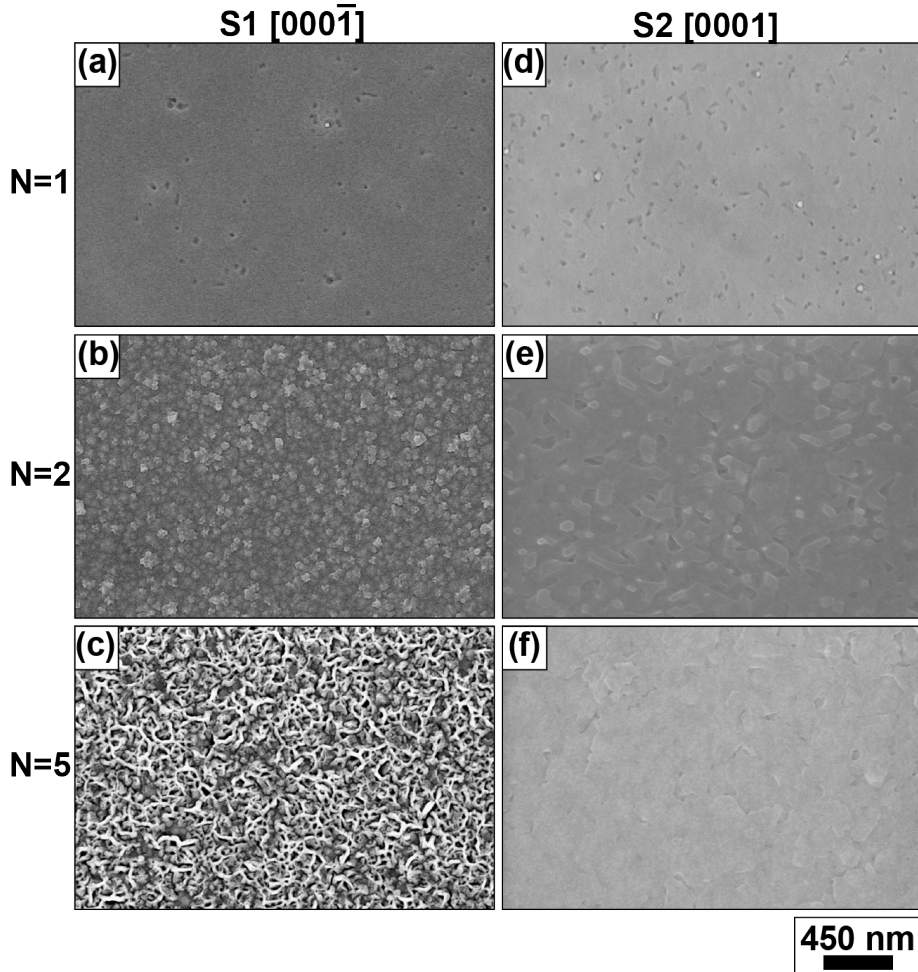


Figure 6.5: SEM micrograph of the surface of a 1-, 2- and 5-period ZnO/GaN S1 DBR sample [samples S1-57, S1-43 and S1-62] for (a)–(c)] and the surface of a 1-, 2- and 5-period S2 DBR [samples S2-44, S2-47 and S2-48] for (d)–(f)].

6. ZNO/GAN DISTRIBUTED BRAGG REFLECTORS

The surface morphology of the ZnO/GaN S1 DBRs top GaN-layer evolved from a smooth surface for a one-pair [Fig. 6.5(a)] DBR to a more rough morphology after two [Fig. 6.5(b)] and five periods [Fig. 6.5(c)]. The surface morphology improved for the first S1 DBR pair with a LT- and HT-GaN layer [Fig. 6.1(a) and (b)] but this improvement was not maintained after growing additional pairs. A rough surface morphology similar to the surface of the samples grown without LT/HT-GaN, was observed after 5–7 pairs.

The surface morphology of the ZnO/GaN S2 DBRs top GaN-layer is smooth after one pair [Fig. 6.5(d)] and remains essentially unchanged after the growth of two [Fig. 6.5(e)] and five pairs [Fig. 6.5(f)].

This shows that the surface morphology for the S1 DBRs becomes more rough after growing more pairs compared to the S2 DBRs where a smooth surface is maintained even after growing a large number of pairs. This was also confirmed by AFM which showed that the RMS roughness was 6–7 times larger for the S1 samples compared to the S2 DBR structures. The PV distance was ≈ 5 times larger (Table 6.1).

Figure 6.6(a) shows an AFM micrograph of a 20-period ZnO/GaN S1 DBR (sample S1-55). The surface exhibit a relatively high RMS roughness of 12.5 nm and a PV distance of 100 nm. Figure 6.6(b) shows the sample surface of a 5.5-pair ZnO/GaN S2 DBR (sample S2-07) with a comparably low RMS roughness of 2.1 nm and a PV distance of 20.6 nm.

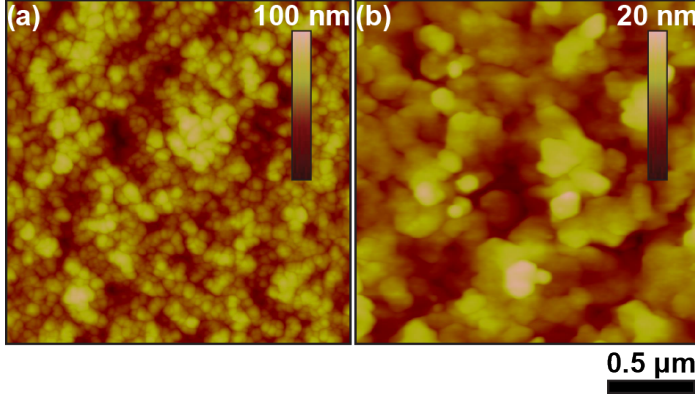


Figure 6.6: (AFM micrograph of the surface of a (a) 20-period ZnO/GaN S1 DBR (sample S1-55) and (b) a 5.5-period ZnO/GaN S2 DBR (sample S2-07).

The ZnO/GaN S1 DBRs were crack-free without Ga-droplets and the morphology evolved into a rough surface for a higher number of pairs. The ZnO/GaN S2 DBRs were crack-free with some samples having Ga-droplets on the surface due to inadequate

control of the Ga-flux caused by an inefficient source control circuit. Samples grown during Ga-rich conditions exhibited smooth surfaces with Ga-droplets such as samples S2-07 and S2-48. DBRs grown during N-rich conditions exhibited smooth layers with a pronounced plateau-valley morphology exemplified by samples S2-51 and S2-45.

6.5 ZnO/GaN DBR Reflectance

Figure 6.7(a) shows the measured reflectance for a 2-, 7- and 20-period S1 ZnO/GaN DBR from table 6.1 grown at the same T_S as shown in Fig.6.1(a).

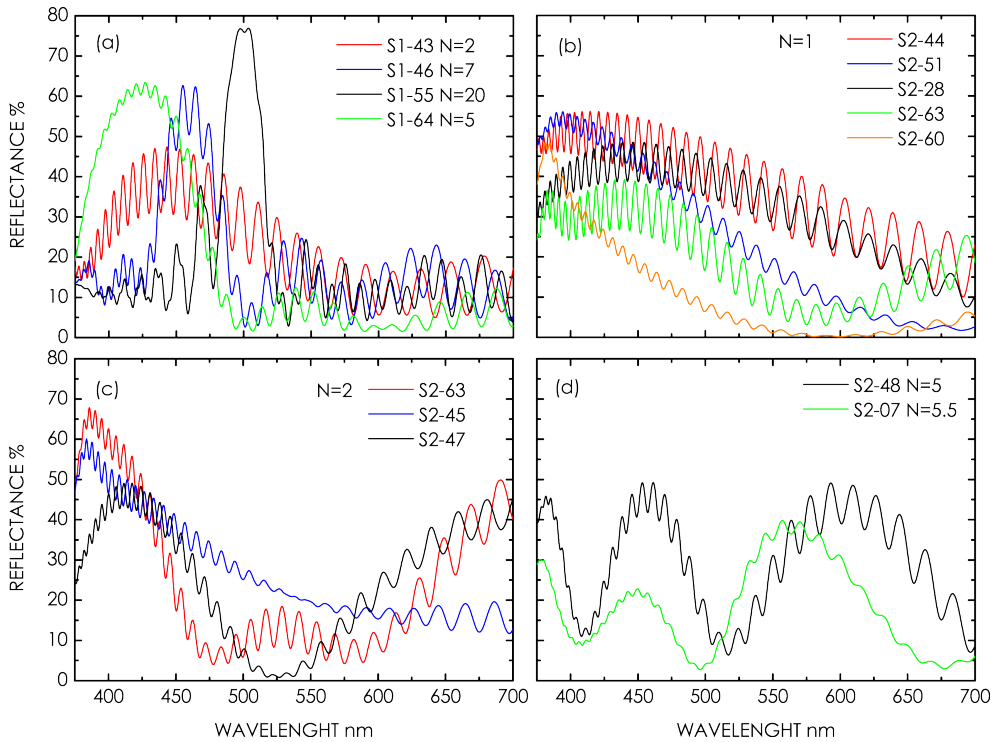


Figure 6.7: Reflectance spectra for ZnO/GaN S1 DBRs grown along the ZnO(000 $\bar{1}$) direction (a) and for ZnO/GaN S2 DBRs grown along the opposite ZnO(0001) direction, (b)–(c). The sample name and the number of periods N is indicated for each sample or graph.

The highest reflectivity of 77% was achieved for a 20-period ZnO/GaN S1 DBR (sample S1-55) with a stopband center wavelength λ_{SB} at 500 nm and with a stopband width of 32 nm. The thickness of the ZnO and the GaN layer is 60.9 nm and 51.0 nm, respectively according to the $\lambda/4$ criteria corresponding to this position for the stopband center wavelength λ_{SB} . Figure 6.7(a) also shows the measured reflectance for a 5-period ZnO/GaN S1 DBR (sample S1-64) grown with the LT/HT-GaN procedure [Fig.6.1(b)]. A similar reflectance was measured for sample S1-62 [Table 6.1] which was also grown with the LT/HT-GaN procedure. These samples exhibited the same the reflectivity as for a 7-period ZnO/GaN DBR grown at the same T_S (sample S1-46). From this we conclude that the improved reflectivity for a S1 DBR grown with the LT/HT-GaN procedure is due to an improved interface quality compared with the growth procedure where the same T_S is used for both ZnO and GaN. These conclusions are also supported from the observations of a more streaky RHEED pattern for the LT/HT-GaN samples compared with a spotty RHEED-pattern for samples grown at the same temperature.

The growth along the ZnO((0001) direction [growth procedure in Fig.6.1(c)] was investigated for fewer pairs in order to decrease the interface and surface roughness of the layers which in turn would improve the reflectance. Figure 6.7(b) shows the reflectivity for ZnO/GaN S2 DBRs grown with one period of (LT-ZnO/HT-ZnO)/(LT-GaN/HT-GaN) [samples in table 6.1]. A reflectance of 40–55% was achieved after one period and with $\lambda_{SB} = 400 - 500$ nm. The different positions of the peaks correspond to varying ZnO and GaN layer thicknesses of the different DBRs. For instance, a thinner layer moves the λ_{SB} position towards shorter wavelengths.

Figure 6.7(c) shows the reflectivity for ZnO/GaN S2 DBRs grown with two periods [samples in table 6.1]. The reflectance is 45–60% and a second stopband at a longer wavelength appeared for some samples such as S2-63 and S2-47. This is attributed to failing control circuitry of the Zn-source resulting in an uneven Zn-flux for a longer time period. This caused the ZnO layers to be thinner than expected. Also the Ga-source was failing and resulted in an erratic behavior with an intermittent stable/unstable Ga-flux causing either too much or too little Ga during the GaN growth. This explained why the GaN layers were not possible to grow Ga-stable for the prolonged periods required for the growth of the DBRs. It also explained why some samples exhibited both Ga-droplets and a plateau-valley morphology indicative of N-rich growth conditions. A Ga-rich growth condition resulted in a thicker than expected GaN layer due to the continuing growth during the temperature ramps when the N-plasma was on but the Ga-shutter closed. An N-rich growth condition resulted in thinner GaN-layers with a typical plateau-valley morphology. The drift between each S2 DBR-period made it virtually impossible to maintain a repeatable period thickness. This is shown by sample S2-63 where the $\lambda_{SB} = 440$ nm after the first grown period [Fig. 6.7(b)] and $\lambda_{SB} = 390$ nm after the second grown period even though the growth parameters were seemingly identical. This sample was removed from the MBE after the first period. The reflectivity was measured and the sample

was then reinserted into the MBE system for the overgrowth of the second pair.

The reflectance spectra for S2 DBRs grown with 5 and 5.5 periods also showed multiple reflectance peaks [Fig. 6.7(d)] due to the insufficient thickness control. Despite these thickness control problems, the S2 DBRs exhibited a significantly improved surface morphology compared with the ZnO/GaN S1 DBRs [SEM micrographs in Fig.6.5(c) and (f)]. The reflectance of the S2 DBRs were also comparably higher already after one period [Fig. 6.7(c)] which we relate to the lower surface roughness of the S2 DBRs.

6.6 Microanalysis of ZnO/GaN DBRs

Figure 6.8 shows a high-angle annular dark-field scanning transmission electron microscope (HAADF-STEM) micrograph for a 20-period ZnO/GaN S1 DBR (sample S1-55) [Fig. 6.8(a)] and for a 5-period ZnO/GaN S2 DBR (sample S2-48) [Fig. 6.8(b)].

The periodic ZnO/GaN structure can be observed clearly in Fig. 6.8(a) where each dark layer corresponds to ZnO and each bright layer corresponds to GaN. A low HAADF-STEM contrast between the ZnO and GaN layers is expected due to same atomic number for ZnO (30+8) as for GaN (7+31). Compared to sample S1-55, the ZnO are thinner and whereas the GaN layers in the S2 DBR [Fig. 6.8(b)]. This was also verified with cross-sectional SEM.

Figure 6.9(a)–(c) shows cross-sectional images of three ZnO/GaN S2 DBRs grown with 5 periods [Fig. 6.9(a)(sample S2-48) and (c) (sample S2-15)] and 5.5 periods [Fig. 6.9(b)(sample S2-07)].

The periodic structure of the ZnO/GaN DBRs is clearly visible. The first two periods of sample S2-48 [Fig. 6.9(a)] are 82 and 75 nm, respectively which is lower than than the target period of 101 nm [schematic in Fig.6.1]. For this sample it is estimated that the largest deviation of the total period thickness originates from the ZnO layer.

Sample S2-07 DBR exhibited ZnO layers with a thickness of 31–36 nm and GaN layers that were 80–116 nm thick [Fig. 6.9(a)]. These thickness variations are the reason for the multiple reflectance peaks or stopbands previously shown in Figure. 6.7(d).

The thickness measurement of each (ZnO/GaN)-pair of the S2-15 DBR [Fig. 6.9(b) (sample S2-15)] yielded (14/45), (12/38), (16/42), (14/38) and (12/45) nm which is close to the target layer thickness of 46 nm for GaN but far from the target ZnO thickness of 56 nm required for reaching the target $\lambda_{SB} = 450 \text{ nm}$. These samples exhibited Ga-droplets which reduced the reflectance through scattering if the incident light. This was very prominent for sample S2-15 which had a very high density of Ga-droplets and consequently barely no reflectance peak. However, the observed interfaces for the S2 DBRs were abrupt which is a necessity for an efficient DBR.

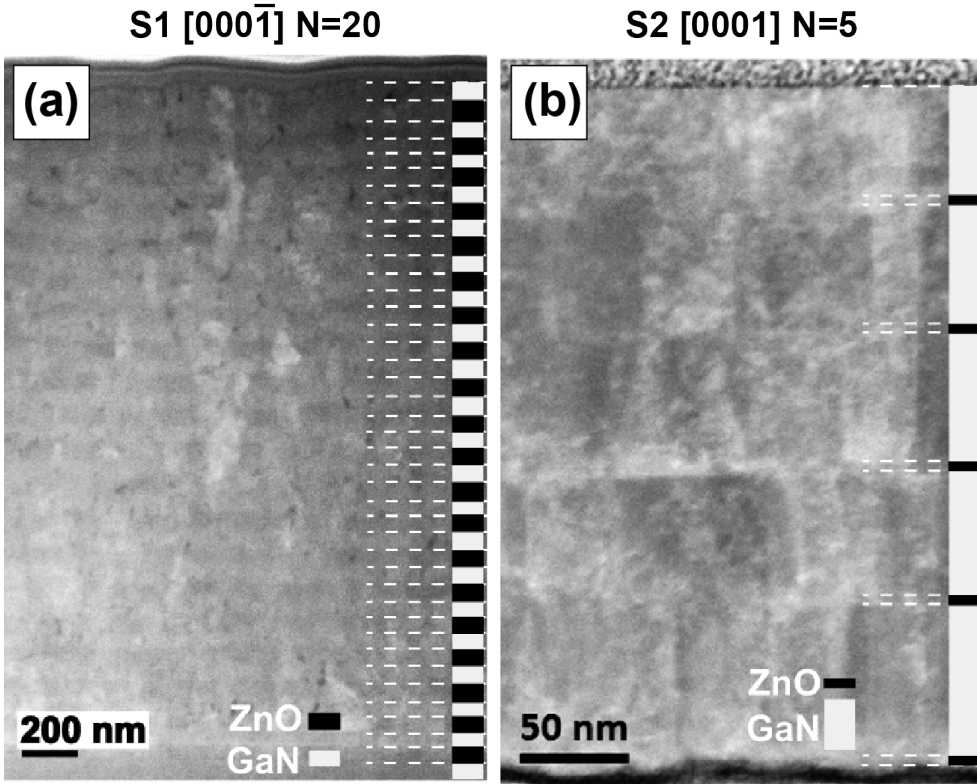


Figure 6.8: Cross-sectional HAADF-STEM phase contrast images of (a) a 20-period ZnO/GaN DBR grown along ZnO(000 $\bar{1}$) direction (sample S1-55) and (b) a 5-period ZnO/GaN DBR grown along the ZnO(0001) direction (sample S2-48). *Courtesy Dr. Reza R. Zamani at Solid State Physics and Nanometer Structure Consortium (nmC@LU), Lund University, Sweden.*

6.7 Structural analysis of ZnO/GaN DBRs

Figure 6.10 shows symmetric XRD $\omega/2\theta$ triple axis scans across the (0002) reflections for a 2- and a 20-period ZnO/GaN S1-DBR (samples S1-43 and S1-55) and the corresponding scan for a 5.5 period S2 DBR (sample S2-07).

Interference fringes are observed to the left of the ZnO(0002)-peak for the 2-period DBR (sample S1-43) which indicates a smooth interface morphology. The interfer-

ence fringes are reduced for the 20-period DBR (sample S1-55) which indicates an increased interface roughness. Both ZnO(0002) peaks are located to the left of the GaN(0002) peak indicating a relaxed or nearly relaxed structure. These observations are in agreement with the previously shown surface morphologies for 1–5 period DBRs [Fig. 6.5(a)-(c)] where the surface morphology became rougher with an increasing number of periods. The position of the ZnO(0002) peak for the 5.5 period DBR (sample S2-07) is located further to the left as compared to the (0002)-peaks related to the S1-DBRs. This shows that these ZnO layers are strained to the GaN-layers. The intensity of this ZnO(0002) reflection was also very weak due to the low thickness of the layer. The observations from the $\omega/2\Theta$ -scans are in agreement with reciprocal spacemaps captured across the asymmetric (10 $\bar{1}$ 5) reflection which showed a nearly relaxed ZnO peak for the 20-period S1-DBR (sample S1-55) and a low-intensity strained ZnO peak for the S2-DBR (sample S2-07) [paper V].

Preliminary data obtained from X-ray $2\Theta/\omega$ -scans with an open detector in the range $10 < 2\Theta < 80^\circ$ exhibit a difference between DBRs grown along the ZnO(000 $\bar{1}$) and the ZnO(0001)-directions. Additional weaker peaks in the spectrum are observed for the DBRs grown along the ZnO(000 $\bar{1}$) which is an indication of interface oxides. TEM investigations must be carried out for a correct identification of the phase of the interface oxides.

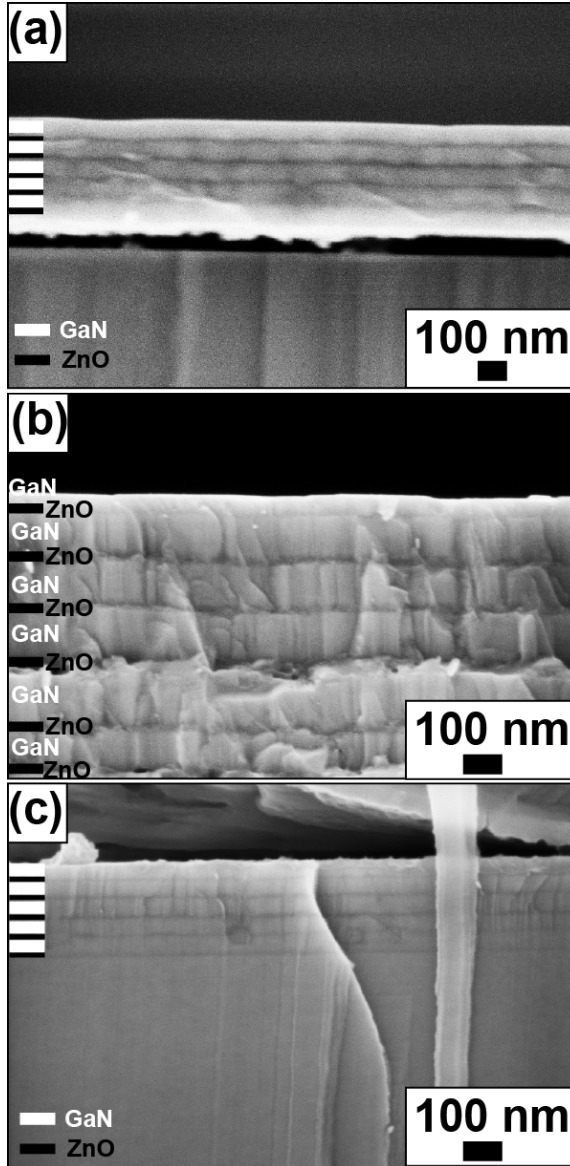


Figure 6.9: Cross-sectional SEM images of (a) a 5-period (sample S2-48), (b) a 5.5-period (sample S2-07) and (c) a 5-period (sample S2-15) ZnO/GaN DBR grown along the ZnO(0001) direction.

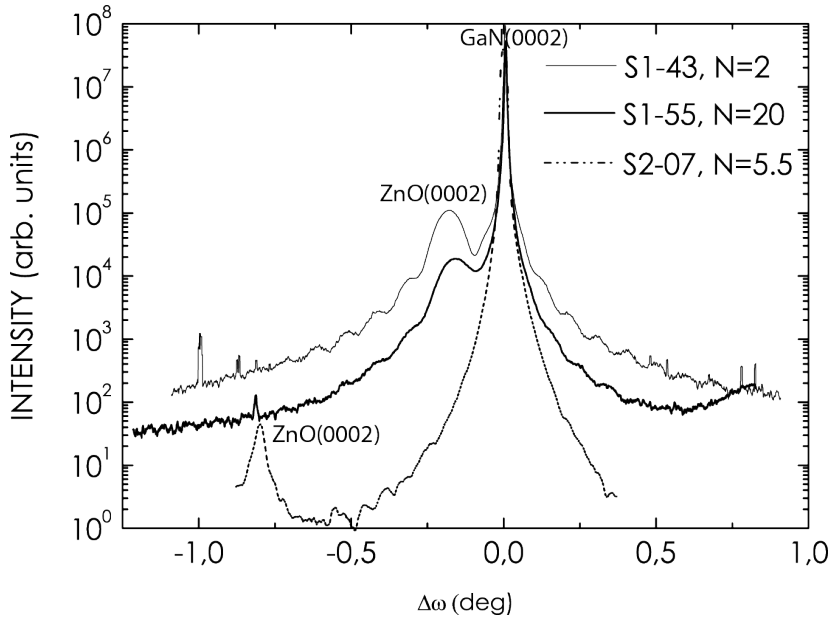


Figure 6.10: Symmetric XRD $\omega/2\theta$ triple axis scans across the (0002) reflections for a 2-period ZnO/GaN DBR grown along the ZnO(000 $\bar{1}$) direction (sample S1-43), a 20-period ZnO/GaN DBR grown along the ZnO(000 $\bar{1}$) direction (sample S1-55) and a 5.5-period ZnO/GaN DBR grown along the ZnO(0001) direction (sample S2-07).

Chapter 7

Summary and Outlook

This chapter presents an outlook for ZnO/GaN DBRs in the context of fabricating a blue-emitting VCSEL. A motivation for growing DBRs along (0001) as being the most promising way forward, is presented. The DBRs grown along (000 $\bar{1}$) may also be improved, which is also discussed.

7.1 Summary and discussion

The 20-period ZnO(000 $\bar{1}$)/GaN DBR presented in this work shows a reflectance of 77% which was the highest obtained reflectance value for all structures. This type of DBR also exhibited a surface roughness that increased after each grown period. The reason for this morphology degradation is presently unknown and warrants further studies.

A possible explanation is that a higher-than-expected Zn-flux was used inadvertently due to the failing Zn-source control circuitry. As has been shown previously, a high Zn-flux yields a rough ZnO surface. Nevertheless, the Zn- BEP was measured before each growth experiment and in some cases also before each grown period and these BEP measurements did not show any significant change of the Zn-BEP.

Another cause for the deteriorating surface morphology could be the low GaN growth temperature employed $T_S = 350^\circ\text{C}$. This low T_S is known to be a very challenging for obtaining high-quality GaN. The established GaN T_S is in the temperature region $720 < T_S < 800^\circ\text{C}$.

The ZnO(000 $\bar{1}$)-oriented DBRs that were fabricated with a LT/HT-GaN layers did initially show a streaky RHEED-pattern and consequently a smoother surface

morphology after the first period but after growing a number of periods, the surface still became rougher. These ZnO(000 $\bar{1}$)/(LT/HT-GaN) DBRs did not show a significant improvement in terms of surface roughness as compared to the DBRs grown at a constant T_S for both ZnO and GaN.

Yet another possible explanation is the effect of surface oxides formed on the GaN surface when the growth of the ZnO layers was initiated. Reports have described that O-plasma pre-exposure create monoclinic Ga₂O₃ on the GaN(0001)-surface. This surface oxide results in a lesser structural quality ZnO(000 $\bar{1}$). The length of the O-plasma exposure affects the thickness of the Ga₂O₃ surface oxide. A 5 min O-plasma pre-exposure was used for the growth of the O-polar DBRs. A reduced thickness of Ga₂O₃ may improve the structural quality of O-polar ZnO. The minimum O-plasma exposure time that still yields ZnO(000 $\bar{1}$), is yet unknown.

The growth of GaN on ZnO(000 $\bar{1}$) has also been reported to exhibit an interface oxide ZnGa₂O₄ which also might affect the structural quality of the layers. Diffraction patterns obtained from XRC scans with open detector in the range $10 < 2\Theta < 80^\circ$ show that there is a difference between DBRs with ZnO layers grown along the ZnO(000 $\bar{1}$) axis and the opposite ZnO(0001) direction. The ZnO(000 $\bar{1}$) scan shows diffraction peaks that are not observed for the (0001) grown DBRs. These additional peaks most likely are an indication of the presence of ZnGa₂O₄ or similar oxides but a TEM analysis must be carried out to unambiguously identify this interface oxide.

In contrast to the O-polar DBRs, the surface morphology of the DBRs grown along the ZnO(0001) direction showed a smoother surface morphology. These DBRs yielded a comparably high reflectance of 45–55% already after the growth of the first pair. The literature report on small or no interface oxides on the ZnO(0001)/GaN interface. Preliminary data from X-ray $2\Theta/\omega$ -scans in the range $10 < 2\Theta < 80^\circ$ did not exhibit any extra unknown peaks related to interface oxides. Studies found in the literature show that a higher crystal quality is achieved for ZnO(0001) compared to ZnO(000 $\bar{1}$).

As has been shown previously in this work, the maximum efficiency of the O-plasma source can be found with optical emission spectroscopy. Operating the O-plasma source at this point yields the maximum growth rate from which the smoothest surface can be found by optimizing the Zn-flux. Deviations of the O₂ flow-rate from this point will yield a lower growth rate. A higher O₂ flow-rate will affect the surface roughness only to a small degree.

It has also been shown that a precise control of the Zn- and Ga-flux is crucial for obtaining accurate DBR periods. The technical problems encountered for the ZnO(0001) DBRs concerning the instability of the Zn- and the Ga-source fluxes, caused a poor layer thickness accuracy when growing a large number of periods. Despite these equipment issues, the DBRs grown along the ZnO(0001) showed the smoothest surfaces and are therefore the most promising path toward high-reflectance ZnO/GaN DBRs.

7.2 Outlook

The grown ZnO and GaN layers have been confirmed to be n-type materials, as expected. The n-conductivity of both ZnO and GaN can be increased in a controlled fashion through n-doping which is a straightforward process for both materials. Common donors for n-doping of ZnO are Al, Ga and In whereas Si is the most commonly used donor for GaN. The ability to obtain high-reflectance ZnO(0001)/GaN DBRs that are also highly conductive electrically makes it very interesting to use these DBR structures to fabricate a blue VCSEL that is electrically injected through the DBR. Beside the electrically conductive DBR, a tentative blue VCSEL design would consist of a GaN cavity that includes InGaN/GaN QWs. A current aperture could be formed by etching or ion-bombarding the ZnO layers. An electrically conducting top p-type ZnO/GaN DBR is not yet possible due to the challenges associated with p-doping ZnO. Nevertheless, the top DBR could still consist of an in-situ grown ZnO-based DBR. ZnO is readily etched in common acids and forming a mesa is therefore straightforward. The whole VCSEL structure could therefore be grown in-situ thus minimizing the number of device processing steps.

A hybrid oxide/nitride MBE system would be necessary for this project. Based on the experience from working with this type of system, the entire MBE system must be resistant to O to avoid premature degradation of the components. Further, the system should be equipped with Ga, In and Zn sources that yield a very stable flux during growth. The doping sources include a dedicated group III-source such as an In-source for n-doping of ZnO and Si and Mg sources for n- and p-doping of GaN. It would also be desirable to enclose each plasma source in a small turbopumped vacuum chamber since this would allow to keep these sources on permanently throughout the growths.

Both GaN and ZnO are semiconductors with a large exciton binding energy. The exciton binding energy is 26 meV for GaN and 60 meV for ZnO meaning that the excitons are stable at room temperature. An exciting project including the hybrid MBE system is to grow cavity-polariton ZnO/GaN structures for the fundamental study of polaritons. Combining these two semiconductors might lead to new insights in polariton physics and also open the path to practical applications based on polaritons.

Chapter 8

Summary of Papers

Paper I

Nucleation and epitaxial growth of ZnO on GaN(0001) The growth of ZnO on GaN(0001)/Al₂O₃ templates was compared with the growth of ZnO on GaN(0001)/4H-SiC(0001)-buffer layers using the same growth chamber for both ZnO and GaN. The growth of ZnO and GaN using the same growth chamber is a very rare approach that has been previously investigated only once. A significant difference in terms of nucleation and growth between the substrates was observed. The GaN(0001)/Al₂O₃ templates was found to need a surface pre-treatment to allow the formation of a ZnO layer. Zn-, Ga- and N-plasma pre-treatments were investigated. The in-situ grown GaN/4H-SiC(0001) buffer layers did not need any surface treatment to enable the ZnO layer growth. The different nucleation and subsequent epitaxial growth is related to the existence of monoclinic Ga₂O₃ the GaN/Al₂O₃ templates surfaces. The growth of ZnO and GaN has so far been performed in two different growth chambers by other research groups. The transfer between the growth chambers in ambient, exposes the first grown GaN(0001)-layer to air. This procedure inevitably creates sub-oxides on the GaN(0001)-surface. By using the same growth chamber for GaN and ZnO it is therefore possible to avoid the formation of sub-oxides on the GaN(0001) surface.

My contribution: The growth experiments, RHEED analysis, AFM, XRD and SEM of all samples. Dr. Per Malmberg conducted the TOF-SIMS measurements at the National center for imaging mass spectrometry at Chalmers University of Technology in Gothenburg Sweden. I analyzed the SIMS-results. I wrote the paper.

Paper II

Plasma-assisted molecular beam epitaxy of ZnO on *in-situ* grown GaN/4H-SiC buffer layers A growth study was made of ZnO growth on in-situ deposited GaN/4H-SiC buffer layers. The growth was investigated with respect to the Zn-source temperature, the substrate temperature and the O₂ flow-rate. The full-width-at-half-maximum for x-ray rocking curves obtained across the ZnO(0002) and ZnO(10 $\bar{1}$ 5) reflections was 198 and 948 arcsec, respectively. From RSMs we concluded that the relaxation of our ZnO layers occurred early and abruptly in the course of the growth. The crystal quality was assessed with XRD and we found that crystal quality of ZnO and GaN grown in the same growth chamber, was comparable. Room-temperature Hall-measurements were performed on the ZnO layers. All films were inherently n-type. The background electron carrier concentration n was $1 \times 10^{19} \text{ cm}^{-3}$ with $\mu = 50 \text{ cm}^2/\text{Vs}$ and a sheet resistance R_s of $1.1 \text{ k}\Omega/\square$.

My contribution: The growth experiments and AFM, XRD, SEM of all samples. The Hall-effect measurements were made together with Tobias Tingberg. I wrote the paper.

Paper III

Growth of ZnO(0001) on GaN(0001)/4H-SiC buffer layers by plasma-assisted hybrid molecular beam epitaxy The growth of ZnO(0001) on GaN(0001)/4H-SiC was investigated. A more extensive systematic investigation was made of the ZnO growth. The Zn-flux was determined with a thickness calibration from the deposition of Zn and cross-sectional SEM. Smooth ZnO layers were obtained with a root-mean-square roughness of 0.3 nm. Electrical measurement were made on both ZnO and GaN layers. The polarity was determined with wet-etch experiments and SEM characterization of the surface morphology. Both columnar ZnO layers and compact and statistically smooth ZnO layers were achieved. The crystal quality was assessed for all grown layers with a thickness above 34 nm. The background electron carrier concentration n for the GaN-layers was $1.8 \times 10^{18} \text{ cm}^{-3}$ with $\mu = 108 \text{ cm}^2/\text{Vs}$ and a sheet resistance R_s of $1058 \Omega/\square$.

My contribution: The growth experiments and AFM, XRD, SEM of all samples. Polarity determination of the layers. The Hall-effect measurements were made together with Tobias Tingberg. I wrote the paper. I also gave an oral presentation of these results at the 18th European Molecular Beam Epitaxy Workshop in Canazei, Italy, March 15-18, 2015.

Paper IV

Impact of O₂ flow rate on the growth rate of ZnO(0001) and ZnO(000 $\bar{1}$) on GaN by plasma-assisted molecular beam epitaxy In this paper we report on a new growth-rate dependence for ZnO(0001) and ZnO(000 $\bar{1}$) growth on GaN(0001)/Al₂O₃ templates with respect to the O₂ flow rate. ZnO(0001) layers were also grown on in-situ grown GaN(0001)/4H-SiC(0001) buffer layers. An unexpected decrease of the ZnO growth-rate was observed for higher O₂ flow-rates. This is contrary to the behavior reported in the literature. Optical emission spectroscopy on the plasma source was employed to identify the contents of the plasma. The emission intensity from the plasma is an assessment of the amount of active O inside the plasma. Excited neutral atomic O (OI) and excited and singly ionized atomic O (OII) was identified. Excited and singly ionized molecular O (O₂⁺) was also identified. The spectral lines exhibited a maximum emission intensity for the OI, OII and unresolved OI/OII-lines for $1.0 < \Phi_{O_2} < 2.0$ sccm. This trend follows the evolution of the growth-rate in the Φ_{O_2} interval of 1.0–2.0 sccm for both ZnO(0001) and ZnO(000 $\bar{1}$). The evolution of the O₂⁺ line intensity as a function of Φ_{O_2} differed significantly and did not correlate with the ZnO-growth-rate. We therefore concluded that the O₂⁺ contribution to the ZnO growth is negligible. This showed that the active O species related to the OI, OII and unresolved OI/OII-lines significantly contributed to the ZnO growth. We have shown that it is not the direct amount of O₂ supplied to the O-plasma source that determine the growth rate but rather the amount of active O delivered from the O-plasma source.

My contribution: Growth of both ZnO(0001) and ZnO(000 $\bar{1}$) layers. Identification of the unexpected growth rate dependence on the O₂ flow-rate during early growth experiments. Setup of optical emission spectroscopy. Collection and analysis of optical emission spectra and peak identification. Polarity determination. SEM-characterization. I wrote the paper.

Paper V

Hybrid ZnO/GaN distributed Bragg reflectors grown by plasma-assisted molecular beam epitaxy, In this paper we report on the fabrication of two types of ZnO/GaN distributed Bragg reflectors with center wavelengths 400–500 nm and with up to 20 ZnO/GaN periods. Growth along both ZnO(0001) or ZnO(000 $\bar{1}$) direction was investigated. A maximum reflectivity of 77% at a center wavelength of 501 nm was achieved with a 20-pair ZnO(000 $\bar{1}$)/GaN reflector. The periodic structure of the DBRs is clearly shown in micrographs obtained by transmission electron microscopy. The DBRs were grown completely in-situ. ZnO(000 $\bar{1}$) reflectors were grown at the same substrate growth temperature for ZnO and GaN and also with a low-temperature/high-temperature-GaN-layer. An improved reflectivity was achieved

with the insertion of the LT/HT-GaN layer. The ZnO(0001)/GaN reflectors were fabricated with LT/HT-layers for both ZnO and GaN. One period therefore corresponded to (HT-ZnO/LT-ZnO)/(HT-GaN/LT-GaN). A smoother surface morphology was achieved for ZnO(0001)/GaN DBRs which improved the reflectivity for the first 1–2 grown pairs compared to the ZnO(000 $\bar{1}$)/GaN reflectors. Reciprocal space maps show that the ZnO(000 $\bar{1}$)/GaN reflectors are relaxed whereas the ZnO(0001)/GaN reflectors are strained. The ability to n-type dope the ZnO and GaN makes the ZnO(0001)/GaN reflectors interesting for bottom reflectors in blue vertical surface emitting lasers. This is the first time ZnO/GaN DBRs have been reported.

My contribution: Growth experiments. Reflectance measurements, SEM-, AFM- and XRD-characterization. The TEM-characterization was made by Dr. Reza R. Zamani in the group of Prof. Kimberly A. Dick Thelander (Solid State Physics and Nanometer Structure Consortium (nmC@LU), Lund University). I wrote the paper.

References

- [1] B. Monemar, "Fundamental energy gap of GaN from photoluminescence excitation spectra," *Phys. Rev. B*, 10:676–681, 1974.
- [2] T. Ive. *Growth and investigation of Al/GaN and (Al,In)N/GaN based Bragg reflectors*. PhD thesis, Paul-Drude-Institut Für Festkörperelektronik Berlin, 2005.
- [3] Blu-ray.com, "About: What is Blu-ray?," <http://www.blu-ray.com/info/>. Last checked: 2016-04-25.
- [4] A. Janotti and C. G. V. de Walle, "Fundamentals of zinc oxide as a semiconductor," *Rep. Prog. Phys.*, 72(12):126501, 2009.
- [5] U. Özgür, V. Avrutin, and H. Morkoç, "Chapter 16 - zinc oxide materials and devices grown by MBE," In M. Henini, editor, *Molecular Beam Epitaxy*, pages 369 – 416. Elsevier, Oxford, 2013.
- [6] A. Cho and J. Arthur, "Molecular beam epitaxy," *Progress in Solid State Chemistry*, 10, Part 3(0):157 – 191, 1975.
- [7] W. P. McCray, "MBE deserves a place in the history books," *Nat Nano*, 2(5):259–261, 2007.
- [8] R. D. Vispute, V. Talyansky, S. Choopun, R. P. Sharma, T. Venkatesan, M. He, X. Tang, J. B. Halpern, M. G. Spencer, Y. X. Li, L. G. Salamanca-Riba, A. A. Iliadis, and K. A. Jones, "Heteroepitaxy of ZnO on GaN and its implications for fabrication of hybrid optoelectronic devices," *Appl. Phys. Lett*, 73(3):348–350, 1998.
- [9] T. Ive, T. Ben-Yaacov, C. V. de Walle, U. Mishra, S. DenBaars, and J. Speck, "Step-flow growth of ZnO(0001) on GaN(0001) by metalorganic chemical vapor epitaxy," *J. Cryst. Growth*, 310(15):3407–3412, 2008.

REFERENCES

- [10] C. Bayram, F. H. Teherani, D. J. Rogers, and M. Razeghi, "A hybrid green light-emitting diode comprised of n-ZnO/(InGaN/GaN) multi-quantum-wells/p-GaN," *Appl. Phys. Lett*, 93(8):-, 2008.
- [11] J. Y. Lee, J. H. Lee, H. S. Kim, C.-H. Lee, H.-S. Ahn, H. K. Cho, Y. Y. Kim, B. H. Kong, and H. S. Lee, "A study on the origin of emission of the annealed n-ZnO/p-GaN heterostructure LED," *Thin Solid Films*, 517(17):5157 – 5160, 2009. 4th International Conference on Technological Advances of Thin Films and Surface Coatings.
- [12] Y. I. Alivov, J. E. Van Nostrand, D. C. Look, M. V. Chukichev, and B. M. Ataev, "Observation of 430 nm electroluminescence from ZnO/GaN heterojunction light-emitting diodes," *Appl. Phys. Lett*, 83(14):2943–2945, 2003.
- [13] D. J. Rogers, F. Hosseini Teherani, A. Yasan, K. Minder, P. Kung, and M. Razeghi, "Electroluminescence at 375 nm from a ZnO/GaN:Mg c-Al₂O₃ heterojunction light emitting diode," *Appl. Phys. Lett*, 88(14):141918, 2006.
- [14] T. Ive, T. Ben-Yaacov, A. Murai, H. Asamizu, C. G. Van de Walle, U. Mishra, S. P. DenBaars, and J. S. Speck, "Metalorganic chemical vapor deposition of ZnO(0001) thin films on GaN(0001) templates and ZnO(0001) substrates," *Phys. Status Solidi C*, 5(9):3091–3094, 2008.
- [15] F. Schuster, B. Laumer, R. R. Zamani, C. Magén, J. R. Morante, J. Arbiol, and M. Stutzmann, "p-GaN/n-ZnO Heterojunction Nanowires: Optoelectronic Properties and the Role of Interface Polarity," *ACS Nano*, 8(5):4376–4384, 2014. PMID: 24720603.
- [16] H.-J. Ko, S.-K. Hong, Y. Chen, and T. Yao, "A challenge in molecular beam epitaxy of ZnO: control of material properties by interface engineering," *Thin Solid Films*, 409(1):153 – 160, 2002. Proceedings of the 2nd Asian Conference on Chemical Vapour Deposition.
- [17] H. J. Ko, Y. Chen, S. K. Hong, and T. Yao, "MBE growth of high-quality ZnO films on epi-GaN," *J. Cryst. Growth*, 209(4):816 – 821, 2000.
- [18] S.-K. Hong, T. Hanada, H.-J. Ko, Y. Chen, T. Yao, D. Imai, K. Araki, and M. Shinohara, "Control of polarity of ZnO films grown by plasma-assisted molecular-beam epitaxy: Zn- and O-polar ZnO films on Ga-polar GaN templates," *Appl. Phys. Lett*, 77(22):3571–3573, 2000.
- [19] S.-K. Hong, T. Hanada, H.-J. Ko, Y. Chen, T. Yao, D. Imai, K. Araki, M. Shinohara, K. Saitoh, and M. Terauchi, "Control of crystal polarity in a wurtzite crystal: ZnO films grown by plasma-assisted molecular-beam epitaxy on GaN," *Phys. Rev. B*, 65:115331, 2002.

-
- [20] S.-K. Hong, H.-J. Ko, Y. Chen, T. Hanada, and T. Yao, "Control and characterization of ZnO/GaN heterointerfaces in plasma-assisted MBE-grown ZnO films on GaN/Al₂O₃," *Appl. Surf. Sci.*, 159-160(0):441 – 448, 2000.
- [21] S.-K. Hong, H.-J. Ko, Y. Chen, T. Hanada, and T. Yao, "Evolution of initial layers of plasma-assisted MBE grown ZnO on (0001)GaN/sapphire," *J. Cryst. Growth*, 214-215(0):81 – 86, 2000.
- [22] M. Johnson, S. Fujita, W. Rowland, W. Hughes, J. Cook, and J. Schetzina, "MBE growth and properties of ZnO on sapphire and SiC substrates," *J. Electron. Mat.*, 25(5):855–862, 1996.
- [23] Y. Higuchi, K. Omae, H. Matsumura, and T. Mukai, "Room-Temperature CW Lasing of a GaN-Based Vertical-Cavity Surface-Emitting Laser by Current Injection," *Appl. Phys. Express*, 1(12):121102, 2008.
- [24] T.-C. Lu, C.-C. Kao, H.-C. Kuo, G.-S. Huang, and S.-C. Wang, "CW lasing of current injection blue GaN-based vertical cavity surface emitting laser," *Appl. Phys. Lett.*, 92(14), 2008.
- [25] G. Cosendey, A. Castiglia, G. Rossbach, J.-F. Carlin, and N. Grandjean, "Blue monolithic AlInN-based vertical cavity surface emitting laser diode on free-standing GaN substrate," *Appl. Phys. Lett.*, 101(15), 2012.
- [26] W.-J. Liu, X.-L. Hu, L. Y. Ying, J.-Y. Zhang, and B.-P. Zhang, "Room temperature continuous wave lasing of electrically injected GaN-based vertical cavity surface emitting lasers," *Appl. Phys. Lett.*, 104(25), 2014.
- [27] C. Holder, J. S. Speck, S. P. DenBaars, S. Nakamura, and D. Feezell, "Demonstration of Nonpolar GaN-Based Vertical-Cavity Surface-Emitting Lasers," *Appl. Phys. Express*, 5(9):092104, 2012.
- [28] T. Onishi, O. Imafuji, K. Nagamatsu, M. Kawaguchi, K. Yamanaka, and S. Takigawa, "Continuous Wave Operation of GaN Vertical Cavity Surface Emitting Lasers at Room Temperature," *IEEE J. Quantum Electron.*, 48(9):1107–1112, 2012. doi:10.1109/JQE.2012.2203586.
- [29] T. C. Lu, J. R. Chen, S. W. Chen, H. C. Kuo, C. C. Kuo, C. C. Lee, and S. C. Wang, "Development of gan-based vertical-cavity surface-emitting lasers," *IEEE J. Sel. Top. Quantum Electron.*, 15(3):850–860, 2009. doi:10.1109/JSTQE.2009.2013181.
- [30] T. C. Lu, T. T. Wu, S. W. Chen, P. M. Tu, Z. Y. Li, C. K. Chen, C. H. Chen, H. C. Kuo, S. C. Wang, H. W. Zan, and C. Y. Chang, "Characteristics of Current-Injected GaN-Based Vertical-Cavity Surface-Emitting Lasers," *IEEE J. Sel. Top. Quantum Electron.*, 17(6):1594–1602, 2011. doi:10.1109/JSTQE.2011.2116771.

REFERENCES

- [31] T.-C. Lu, S.-W. Chen, T.-T. Wu, P.-M. Tu, C.-K. Chen, C.-H. Chen, Z.-Y. Li, H.-C. Kuo, and S.-C. Wang, "Continuous wave operation of current injected GaN vertical cavity surface emitting lasers at room temperature," *Appl. Phys. Lett.*, 97(7), 2010.
- [32] K. Omae, Y. Higuchi, K. Nakagawa, H. Matsumura, and T. Mukai, "Improvement in Lasing Characteristics of GaN-based Vertical-Cavity Surface-Emitting Lasers Fabricated Using a GaN Substrate," *Appl. Phys. Express*, 2(5):052101, 2009.
- [33] D. Kasahara, D. Morita, T. Kosugi, K. Nakagawa, J. Kawamata, Y. Higuchi, H. Matsumura, and T. Mukai, "Demonstration of Blue and Green GaN-Based Vertical-Cavity Surface-Emitting Lasers by Current Injection at Room Temperature," *Appl. Phys. Express*, 4(7):072103, 2011.
- [34] C. O. Holder, J. T. Leonard, R. M. Farrell, D. A. Cohen, B. Yonkee, J. S. Speck, S. P. DenBaars, S. Nakamura, and D. F. Feezell, "Nonpolar III-nitride vertical-cavity surface emitting lasers with a polarization ratio of 100% fabricated using photoelectrochemical etching," *Appl. Phys. Lett.*, 105(3), 2014.
- [35] J. T. Leonard, D. A. Cohen, B. P. Yonkee, R. M. Farrell, T. Margalith, S. Lee, S. P. DenBaars, J. S. Speck, and S. Nakamura, "Nonpolar III-nitride vertical-cavity surface-emitting lasers incorporating an ion implanted aperture," *Appl. Phys. Lett.*, 107(1), 2015.
- [36] T. Ben-Yaacov, T. Ive, C. G. Walle, U. K. Mishra, J. S. Speck, and S. P. Denbaars, "Properties of In-Doped ZnO Films Grown by Metalorganic Chemical Vapor Deposition on GaN(0001) Templates," *J. Electron. Mat.*, 39(5):608–611, 2009.
- [37] I. Vurgaftman and J. R. Meyer, "Band parameters for nitrogen-containing semiconductors," *J. Appl. Phys.*, 94(6):3675–3696, 2003.
- [38] Q. Yan, P. Rinke, M. Winkelkemper, A. Qteish, D. Bimberg, M. Scheffler, and C. G. V. de Walle, "Band parameters and strain effects in ZnO and group-III nitrides," *Semi. Sci. Tech.*, 26(1):014037, 2011.
- [39] D. Brunner, H. Angerer, E. Bustarret, F. Freudenberg, R. Höppler, R. Dimitrov, O. Ambacher, and M. Stutzmann, "Optical constants of epitaxial AlGaIn films and their temperature dependence," *J. Appl. Phys.*, 82(10):5090–5096, 1997.
- [40] P. Yeh. *Optical waves in layered media*. Wiley Interscience, John Wiley & Sons, Inc., 1988.
- [41] O. Ambacher, "Growth and applications of group III-nitrides," *J. Phys. D: Appl Phys.*, 31(20):2653, 1998.

-
- [42] D. I. Florescu, V. M. Asnin, F. H. Pollak, A. M. Jones, J. C. Ramer, M. J. Schurman, and I. Ferguson, "Thermal conductivity of fully and partially coalesced lateral epitaxial overgrown GaN/sapphire (0001) by scanning thermal microscopy," *Appl. Phys. Lett.*, 77(10):1464–1466, 2000.
- [43] D. I. Florescu, L. G. Mourokh, F. H. Pollak, D. C. Look, G. Cantwell, and X. Li, "High spatial resolution thermal conductivity of bulk ZnO (0001)," *J. Appl. Phys.*, 91(2):890–892, 2002.
- [44] O. Ambacher, M. S. Brandt, R. Dimitrov, T. Metzger, M. Stutzmann, R. A. Fischer, A. Miehler, A. Bergmaier, and G. Dollinger, "Thermal stability and desorption of group III nitrides prepared by metal organic chemical vapor deposition," *J. Vac. Sci. Tech. B*, 14(6):3532–3542, 1996.
- [45] F. Bernardini, V. Fiorentini, and D. Vanderbilt, "Spontaneous polarization and piezoelectric constants of III-V nitrides," *Phys. Rev. B*, 56:R10024–R10027, 1997.
- [46] Y. F. Li, B. Yao, Y. M. Lu, Y. Q. Gai, C. X. Cong, Z. Z. Zhang, D. X. Zhao, J. Y. Zhang, B. H. Li, D. Z. Shen, X. W. Fan, and Z. K. Tang, "Biaxial stress-dependent optical band gap, crystalline, and electronic structure in wurtzite ZnO: Experimental and ab initio study," *J. Appl. Phys.*, 104(8), 2008.
- [47] T. Yao and S.-K. Hong, editors. *Oxide and Nitride Semiconductors*. Springer, 2008.
- [48] C. Stampfl and C. G. Van de Walle, "Density-functional calculations for III-V nitrides using the local-density approximation and the generalized gradient approximation," *Phys. Rev. B*, 59:5521–5535, 1999.
- [49] F. Bechstedt, P. Käckell, A. Zywietz, K. Karch, B. Adolph, K. Tenelsen, and J. Furthmüller, "Polytypism and Properties of Silicon Carbide," *Phys. Status Solidi B*, 202(1):35–62, 1997.
- [50] Cree-LED Chips & Materials, "Document library," <http://www.cree.com/LED-Chips-and-Materials/Document-Library>. Last checked: 2014-01-12.
- [51] H. Morkoç, S. Strite, G. B. Gao, M. E. Lin, B. Sverdlov, and M. Burns, "Large-band-gap SiC, III-V nitride, and II-VI ZnSe-based semiconductor device technologies," *J. Appl. Phys.*, 76(3):1363–1398, 1994.
- [52] A. Ashrafi and C. Jagadish, "Review of zincblende ZnO: Stability of metastable ZnO phases," *J. Appl. Phys.*, 102(7):–, 2007.
- [53] H. Morkoç and U. Özgür. *Zinc Oxide*. Wiley-VCH Verlag GmbH & Co. KGaA, 2008.

REFERENCES

- [54] Refractive index of GaN-Sellmeier equation first order, "Refractive index database," <http://refractiveindex.info/?shelf=main&book=GaN&page=Barker-o>. Last checked: 2016-04-27.
- [55] N. A. Sanford, L. H. Robins, A. V. Davydov, A. Shapiro, D. V. Tsvetkov, A. V. Dmitriev, S. Keller, U. K. Mishra, and S. P. DenBaars, "Refractive index study of $\text{Al}_x\text{Ga}_{1-x}\text{N}$ films grown on sapphire substrates," *J. Appl. Phys.*, 94(5):2980–2991, 2003.
- [56] U. Özgür, Y. I. Alivov, C. Liu, A. Teke, M. A. Reshchikov, S. Doğan, V. Avrutin, S.-J. Cho, and H. Morkoç, "A comprehensive review of ZnO materials and devices," *J. Appl. Phys.*, 98(4):–, 2005.
- [57] H. Yoshikawa and S. Adachi, "Optical Constants of ZnO," *Jpn. J. Appl. Phys.*, 36(Part 1, No. 10):6237–6243, 1997.
- [58] Y. S. Park and J. R. Schneider, "Index of Refraction of ZnO," *J. Appl. Phys.*, 39(7):3049–3052, 1968.
- [59] M. Herman, W. Richter, and H. Sitter. *Epitaxy-Physical Principles and Technical Implementation*. Springer, 2003.
- [60] K. Fujiwara, A. Ishii, T. Abe, and K. Ando, "Epitaxial growth of ZnO crystal on the Si-terminated 6H-SiC(0001) surface using the first-principles calculation," *e-J Surf. Sci. Nanotech.*, 4:254–257, 2006.
- [61] T. Ive, O. Brandt, H. Kostial, T. Hesjedal, M. Ramsteiner, and K. H. Ploog, "Crack-free and conductive Si-doped AlN/GaN distributed bragg reflectors grown on 6H-SiC(0001)," *Appl. Phys. Lett*, 85(11):1970–1972, 2004.
- [62] J.-F. Carlin, C. Zellweger, J. Dorsaz, S. Nicolay, G. Christmann, E. Feltn, R. Butt, and N. Grandjean, "Progresses in III-nitride distributed bragg reflectors and microcavities using AlInN/GaN materials," *Phys. Status Solidi B*, 242(11):2326–2344, 2005.
- [63] S. C. Jain, M. Willander, J. Narayan, and R. V. Overstraeten, "III-nitrides: Growth, characterization, and properties," *J. Appl. Phys.*, 87(3):965–1006, 2000.
- [64] M. Herman, W. Richter, and H. Sitter. *Epitaxy-Physical Principles and Technical Implementation*, chapter 7, page 139. Springer, 2003.
- [65] K. Oura, V. Lifshits, A. Saranin, A. Zotov, and M. Katayama. *Surface Science - An introduction*, chapter 12, page 295. Springer-Verlag Berlin Heidelberg, 2003.
- [66] B. A. Wacaser. *Nanoscale Crystal Growth-The importance of interfaces and Phase Boundaries*. PhD thesis, Division of Solid State Physics, Lund University, 2007.

-
- [67] A. Persson. *Epitaxial growth of semiconductor nanowires*. PhD thesis, Division of Solid State Physics, Faculty of Engineering, Lund University, 2005.
- [68] K. Oura, V. Lifshits, A. Saranin, A. Zotov, and M. Katayama. *Surface Science - An introduction*, chapter 10, pages 229–236. Springer-Verlag Berlin Heidelberg, 2003.
- [69] K. Oura, V. Lifshits, A. Saranin, A. Zotov, and M. Katayama. *Surface Science - An introduction*, chapter 13, pages 325–356. Springer-Verlag Berlin Heidelberg, 2003.
- [70] K. Oura, V. Lifshits, A. Saranin, A. Zotov, and M. Katayama. *Surface Science - An introduction*, chapter 14, pages 355–387. Springer-Verlag Berlin Heidelberg, 2003.
- [71] O. Zsebök. *Molecular Beam Epitaxy and Characterisation of GaN-compounds on GaAs(001) and Sapphire(0001)*. PhD thesis, Department of Microelectronics and Nanoscience, Chalmers University of Technology, 2000.
- [72] Y.-S. Kim, N. Bansal, and S. Oh, “Crucible aperture: An effective way to reduce source oxidation in oxide molecular beam epitaxy process,” *J. Vac. Sci. Tech. A*, 28(4):600–602, 2010.
- [73] S. Hasegawa. *Reflection High-Energy Electron Diffraction*. John Wiley & Sons, Inc., 2002.
- [74] S. A. Chambers, “Epitaxial growth and properties of thin film oxides,” *Surface Science Reports*, 39(5-6):105 – 180, 2000.
- [75] H. Nordén and A. Thölen. *Electron Microscopy and Microanalysis*. Fysiska Institutionen, Chalmers Tekniska Högskola, 1984.
- [76] R. Howland and L. Benatar. *A practical guide to Scanning probe microscopy*. Park Scientific Instruments, 1993-1997.
- [77] V.L.Mironov. *Fundamentals of Scanning Probe Microscopy*. The Russian Academi of Sciences, NT-MDT, 2004.
- [78] Homepage of μ masch, “Probes,” <http://www.spmtips.com/afm-tip-hq-nsc15-al-bs>. Last checked: 2014-01-09.
- [79] P. West and N. Starostina. *A guide to AFM image Artifacts*. Pacific Nanotechnology, Inc. Santa Clara CA, USA.
- [80] P. Kidd. *XRD of gallium nitride and related compounds: strain, composition and layer thickness*. PANalytical, 2009.

REFERENCES

- [81] V. M. Kaganer, O. Brandt, A. Trampert, and K. H. Ploog, "X-ray diffraction peak profiles from threading dislocations in GaN epitaxial films," *Phys. Rev. B*, 72:045423, 2005.
- [82] R. Chierchia, T. Böttcher, H. Heinke, S. Einfeldt, S. Figge, and D. Hommel, "Microstructure of heteroepitaxial GaN revealed by X-ray diffraction," *J. Appl. Phys.*, 93(11):8918–8925, 2003.
- [83] T. Metzger, R. Höpler, E. Born, O. Ambacher, M. Stutzmann, R. Stömmer, M. Schuster, H. Göbel, S. Christiansen, M. Albrecht, and H. P. Strunk, "Defect structure of epitaxial GaN films determined by transmission electron microscopy and triple-axis X-ray diffractometry," *Philosophical Magazine A*, 77(4):1013–1025, 1998.
- [84] *X'Pert PRO MRD Epitaxy manual*. PANalytical, 2014.
- [85] D. Baer and S. Thevuthasan. *Characterization of Thin Films and Coatings*, chapter 16, pages 802–804. Elsevier, 2010.
- [86] IONTOF Products TOF-SIMS⁵, "The iontof5," <http://www.iontof.com/products-tofsims5-IONTOF-TOF-SIMS-TIME-OF-FLIGHT-SURFACE-ANALYSIS.htm>.
- [87] R. N. S. Sodhi, "Time-of-flight secondary ion mass spectrometry (TOF-SIMS):- versatility in chemical and imaging surface analysis," *Analyst*, 129:483–487, 2004.
- [88] D. B. Williams and C. B. Carter. *Transmission Electron Microscope*. Springer, second edition, 2009.
- [89] *Avantes Avaspec system manual*. Avantes, 2013.
- [90] Engineering Physics Division. NIST Physical Measurement Laboratory, "Hall-effect," <http://www.nist.gov/>.
- [91] P. Y. Yu and M. Cardona. *Fundamentals of Semiconductors-Physics and Material Properties*. Springer, first edition, 1996.
- [92] S. Svanberg. *Atomic and Molecular Spectroscopy - Basic Aspects and Practical Applications*. Springer, second edition, 1997.
- [93] R. C. Boutwell, M., M. Baudalet, and W. V. Schoenfeld, "Investigation and impact of oxygen plasma compositions on cubic znmgo grown by molecular beam epitaxy," *J. Alloy. Comp.*, 584:327 – 330, 2014.
- [94] W. C. Martin and W. L. Wiese, "Atomic spectroscopy," 1999. National Institute of Standards and Technology, Gaithersburg, MD.

-
- [95] Ralchenko Yu. Reader J. Kramida, A. and NIST ASD Team, "NIST Atomic Spectra Database (version 5.1)," 2013. <http://physics.nist.gov/asd>. National Institute of Standards and Technology, Gaithersburg, MD.
- [96] P. H. Krupenie, "The spectrum of molecular oxygen," *J. Phys. Chem. Ref. Data*, 1(2):423–534, 1972.
- [97] W. C. T. Lee, P. Miller, R. J. Reeves, and S. M. Durbin, "Effects of plasma conditions on properties of ZnO films grown by plasma-assisted molecular beam epitaxy," *J. Vac.Sci.Tech. B*, 24(3):1514–1518, 2006.
- [98] Saint-Gobain Crystals, "LED-substrates, GaN standard templates on sapphire substrates," http://www.crystals.saint-gobain.com/High_Performance_Substrates.aspx. Last checked: 2014-01-12.
- [99] L. Liu and J. Edgar, "Substrates for gallium nitride epitaxy," *Materials Science and Engineering: R: Reports*, 37(3):61 – 127, 2002.
- [100] NOVASiC-Silicon carbide and related materials, "Polishing," <http://www.novasic.com/services/polishing/polishing.php>. Last checked: 2014-01-12.
- [101] R. Kaplan, "Surface structure and composition of β - and 6H-SiC," *Surface Science*, 215(1-2):111 – 134, 1989.
- [102] O. Brandt, R. Muralidharan, P. Waltereit, A. Thamm, A. Trampert, H. von Kiedrowski, and K. H. Ploog, "Critical issues for the growth of high-quality (Al,Ga)N/GaN and GaN/(In,Ga)N heterostructures on SiC(0001) by molecular-beam epitaxy," *Appl. Phys. Lett*, 75(25):4019–4021, 1999.
- [103] P. Waltereit, C. Poblentz, S. Rajan, F. Wu, U. K. Mishra, and J. S. Speck, "Structural properties of GaN buffer layers on 4H-SiC(0001) grown by plasma-assisted molecular beam epitaxy for high electron mobility transistors," *Jpn. J. Appl. Phys.*, 43(12A):L1520–L1523, 2004.
- [104] P. Waltereit. *(Al,Ga,In)N heterostructures grown along polar and non-polar directions by plasma-assisted molecular beam epitaxy*. PhD thesis, Paul-Drude-Institut Für Festkörperelektronik Berlin, 2001.
- [105] A. B. M. A. Ashrafi, Y. Segawa, K. Shin, and T. Yao, "Nucleation and interface chemistry of ZnO deposited on 6H-SiC," *Phys. Rev. B*, 72:155302, 2005.
- [106] A. Ashrafi, Y. Segawa, K. Shin, J. Yoo, and T. Yao, "Nucleation and growth modes of ZnO deposited on 6H-SiC substrates," *Appl. Surf. Sci.*, 249:139 – 144, 2005.

REFERENCES

- [107] A. B. M. A. Ashrafi, Y. Segawa, K. Shin, and T. Yao, "Strain effects in ZnO layers deposited on 6H-SiC," *J. Appl. Phys.*, 100(6):-, 2006.
- [108] A. Ashrafi and Y. Segawa, "Anomalous lattice relaxation mechanics in ZnO/SiC heterostructure," *J. Appl. Phys.*, 103(9):-, 2008.
- [109] A. Ashrafi and M. Aminuzzaman, "ZnO epitaxy on SiC(0001) substrate: Comparison with ZnO/SiC(0001) heterostructure," *Appl. Surf. Sci.*, 257(14):6191 – 6196, 2011.
- [110] J.-H. Kim, D.-H. Cho, W. Lee, B.-M. Moon, W. Bahng, S.-C. Kim, N.-K. Kim, and S.-M. Koo, "Structural and optical properties of epitaxial ZnO thin films on 4H-SiC(0001) substrates prepared by pulsed laser deposition," *J. Alloy. Comp.*, 489(1):179 – 182, 2010.
- [111] A. El-Shaer, A. Bakin, E. Schlenker, A. Mofor, G. Wagner, S. Reshanov, and A. Waag, "Fabrication and characterization of n-ZnO on p-SiC heterojunction diodes on 4H-SiC substrates," *Superlattices and Microstructures*, 42:387 – 391, 2007. E-MRS 2006 Symposium K: ZnO and Related Materials 2006 Spring Meeting of the European Materials Research Society.
- [112] H. Tampo, P. Fons, A. Yamada, K.-K. Kim, H. Shibata, K. Matsubara, S. Niki, H. Yoshikawa, and H. Kanie, "Determination of crystallographic polarity of zno layers," *Appl. Phys. Lett.*, 87(14):141904, 2005.
- [113] H.-J. Ko, T. Yao, Y. Chen, and S.-K. Hong, "Investigation of ZnO epilayers grown under various Zn/O ratios by plasma-assisted molecular-beam epitaxy," *J. Appl. Phys.*, 92(8):4354–4360, 2002.
- [114] A. Setiawan, Z. Vashaei, M. W. Cho, T. Yao, H. Kato, M. Sano, K. Miyamoto, I. Yonenaga, and H. J. Ko, "Characteristics of dislocations in ZnO layers grown by plasma-assisted molecular beam epitaxy under different Zn/O flux ratios," *J. Appl. Phys.*, 96(7):3763–3768, 2004.
- [115] J. Wang, C. Yang, M. Liou, C. Wu, K. Chiu, and W. Chou, "Influence of Zn/O flux ratio and Mn-doped ZnO buffer on the plasma-assisted molecular beam epitaxy of ZnO on c-plane sapphire," *J. Cryst. Growth*, 310(21):4503 – 4506, 2008.
- [116] B. Zhang, B. Yao, S. Wang, Y. Li, C. Shan, J. Zhang, B. Li, Z. Zhang, and D. Shen, "Influence of Zn/O ratio on structural, electrical and optical properties of ZnO thin films fabricated by plasma-assisted molecular beam epitaxy," *J. Alloy. Comp.*, 503(1):155 – 158, 2010.

-
- [117] H. Kato, M. Sano, K. Miyamoto, and T. Yao, "High-quality ZnO epilayers grown on Zn-face ZnO substrates by plasma-assisted molecular beam epitaxy," *J. Cryst. Growth*, 265(3-4):375 – 381, 2004.
- [118] H. Xu, K. Ohtani, M. Yamao, and H. Ohno, "Surface morphologies of homoepitaxial ZnO on Zn- and O-polar substrates by plasma assisted molecular beam epitaxy," *Appl. Phys. Lett.*, 89(7):071918, 2006.
- [119] Y. Chen, H.-J. Ko, S.-K. Hong, T. Yao, and Y. Segawa, "Morphology evolution of ZnO(000-1) surface during plasma-assisted molecular-beam epitaxy," *Appl. Phys. Lett.*, 80(8):1358–1360, 2002.
- [120] H. Kato, M. Sano, K. Miyamoto, and T. Yao, "Effect of O/Zn Flux Ratio on Crystalline Quality of ZnO Films Grown by Plasma-Assisted Molecular Beam Epitaxy," *Jpn. J. Appl. Phys.*, 42(4B):2241–2244, 2003.
- [121] Y. Xia, J. Brault, P. V. és, M. Nemoz, M. Teisseire, M. Leroux, and J.-M. Chauveau, "Growth of Ga- and N-polar GaN layers on O face ZnO substrates by molecular beam epitaxy," *J. Cryst. Growth*, 388(0):35 – 41, 2014.
- [122] X. Gu, M. A. Reshchikov, A. Teke, D. Johnstone, H. Morkoç, B. Nemeth, and J. Nause, "GaN epitaxy on thermally treated c-plane bulk ZnO substrates with O and Zn faces," *Appl. Phys. Lett.*, 84(13):2268–2270, 2004.
- [123] A. Kobayashi, Y. Kawaguchi, J. Ohta, H. Fujioka, K. Fujiwara, and A. Ishii, "Polarity control of GaN grown on ZnO (000-1) surfaces," *Appl. Phys. Lett.*, 88(18), 2006.
- [124] G. Namkoong, S. Burnham, K.-K. Lee, E. Trybus, W. A. Doolittle, M. Losurdo, P. Capezzuto, G. Bruno, B. Nemeth, and J. Nause, "III-nitrides on oxygen- and zinc-face ZnO substrates," *Appl. Phys. Lett.*, 87(18), 2005.

